

UNIVERSITY OF CAMBRIDGE

Spin-mixing and transport through superconducting interlayers in ferromagnetic Josephson junctions

James Michael Devine-Stoneman

St John's College

This thesis is submitted for the degree of Doctor of Philosophy

September 2020

Declaration

This thesis is the result of my own work and includes nothing which is the outcome of work done in collaboration except as specified in the text. It is not substantially the same as any that I have submitted, or, is being concurrently submitted for a degree or diploma or other qualification at the University of Cambridge or any other University or similar institution. I further state that no substantial part of my thesis has already been submitted, or, is being concurrently submitted for any such degree, diploma or other qualification at the University of Cambridge or any other University or similar institution. It does not exceed the prescribed word limit for the Physics and Chemistry Degree Committee.

James Michael Devine-Stoneman

September 2020

Spin-mixing and transport through superconducting interlayers in ferromagnetic Josephson junctions

James Michael Devine-Stoneman

Abstract

The creation of spin-polarization in the superconducting state raises possibilities for low-energy logic and memory elements. Supercurrents of spin-aligned triplet Cooper pairs (or 'triplet pairs') can be generated at magnetically inhomogeneous superconductor/ferromagnet interfaces, and have a longer decay envelope in a ferromagnet than singlet Cooper pairs (or 'singlet pairs'). In this thesis I investigate ferromagnetic nanopillar Josephson devices with different types of ferromagnetic barriers, incorporating spin-mixer interfaces and Rashba spin-orbit coupling. The research focuses on equilibrium spin-transport through intermediary superconducting regions for which experimental and theoretical studies are limited. The behaviour of singlet and triplet pair components in Nb/Cr/Fe/Nb/Fe/Cr/Nb Josephson devices demonstrates that spin-aligned triplet pairs decay more rapidly than singlet pairs in the normal state of the central Nb layer. In the superconducting state of the central Nb layer, the results suggest that at least one of the singlet or spin-aligned triplet components must be non-zero throughout the barrier region in order to carry a Josephson supercurrent. Recent theoretical work predicts that spin-aligned triplets can also arise in the presence of both a ferromagnetic exchange field and a Rashba spin-orbit field. The thesis investigates this hypothesis using Nb/Pt/Co/Pt/Nb Josephson devices, but triplet supercurrents due to the presence of a spin-orbit field from Pt are undetected at zero voltage (equilibrium). These results indicate that out-of-equilibrium transport might be required to generate triplet supercurrents due to spin-orbit fields and/or a different device geometry (e.g. a planar geometry with current components parallel to the superconductor/ferromagnet interface). A recent ferromagnetic resonance experiment showed an enhancement of dynamic spin transport from a ferromagnet through an intermediary superconducting layer when a material with high spin-orbit coupling was present at a distance of around a coherence length from the ferromagnet. This was attributed to triplet pairing opening a triplet channel in the superconductor. Analogous equilibrium Josephson junction experiments presented here did not give rise to a spin-aligned triplet, indicating that the origin of enhanced spin-transport is dependent on non-equilibrium effects.

Acknowledgements

I first met my supervisor Jason Robinson while deciding which first year undergraduate courses to take. Other than deciding to take materials science, the other outcome was a chat about his research, which seemed to lie in exactly the area of science that most provoked my interest. The result was starting a PhD in his group four years later. While a change may be as good as a rest, I felt sure that I wouldn't find a supervisor I work so well with elsewhere, and one who always makes time to give guidance despite his frenetic schedule. I am glad to say that nothing changed in this regard over the last four years, and I want to thank him for his creativity and optimism.

I would like to thank Sachio, with whom I collaborated on work found in two of the chapters of this thesis. Sachio's patience and support through countless hours together in the lab made so much of this work possible.

For training and help in the lab, I also thank group members past and present Carly, Yi, Mario, Kohei, Guang, Angelo and Greg. A special thanks goes to Nadia for her comprehensive expertise in all laboratory matters, and for running a tight ship. I like to think I fare comparatively well in her proverbial annals for never having broken anything too egregiously.

I am grateful for interesting discussions on theoretical aspects I have had with Xavier and Sacha.

I would also like to acknowledge my fellow PhD students in the group, for their support both direct and indirect and for many good times, which regrettably have included karaoke on more than one occasion. In no particular order of singing ability, they are Juliet, Lauren, Carla, Ben, Graham, Harry and Anand (Bence and Linde having escaped such occasions).

I would also like to thank Thomas, who mentored me as a summer student in the group while I was an undergraduate. In a sign of things to follow for the years ahead, Thomas would take me along to the pub quiz at the Alma on Thursday nights. Other regulars in those days included Ravi and Lana, who were great fun in addition to indulging my unhealthy obsession with quizzing. After Thomas left, I became the main instigator of the pub quiz nights, joined by many of the aforementioned names as well as John, Guillaume, Rob, Adam, Matt, Mohsen and Tom. This was such a fixture that I have amassed years of scoring statistics from it, which would be an appendix of the thesis were it not for my better judgement.

As Thomas had mentored me, I later enjoyed mentoring Brook. I then worked with visiting PhD student Ekta, resulting in some interesting experiments and a publication.

I was fortunate to be able to attend numerous workshops, meetings and conferences with the wider superconducting spintronics community. Among these were a workshop at the Spin Phenomena Interdisciplinary Centre in Mainz, a workshop in Amalfi and an international school in Sapporo (both under the Oxide SuperSpin international network), the Applied Superconductivity Conference in Seattle and a Royal

Society meeting in Chicheley Hall. I am grateful to the organizers and for the funding which enabled me to attend these fantastic events.

I would like to offer thanks to the wider Device Materials Group who make it an excellent place to do research.

St John's College was my home for almost eight years, and I would like to acknowledge all the fellows, staff, students and benefactors that did so much for me over that period.

I would like to thank the EPSRC and St John's College for funding this work.

Following my viva I thank Prof. Gavin Burnell and Prof. Manish Chhowalla for thorough discussions on the data analysis and interpretation, in addition to suggestions which have made this thesis more useful to you, hypothetical future reader.

Finally, I thank my family for their support. My parents might still not know what superconducting spintronics is, but they allowed me to take the path I wanted as they always have.

"And you," I said with childish impertinence, "never commit errors?"

"Often," he answered. "But instead of conceiving only one, I imagine many, so I become the slave of none."

The Name of the Rose - Umberto Eco

Contents

Introduction **1**

1 Magnetism **3**
1.1 Ferromagnetism . . . 3
1.1.1 The Weiss molecular field . . . 3
1.1.2 The exchange interaction . . . 4
1.1.3 Influence of band structure . . . 6
1.1.4 Proximity-induced magnetism . . . 7
1.1.5 Landau theory . . . 8
1.1.6 Magnetic anisotropy and hysteresis . . . 8
1.2 Antiferromagnetism . . . 11
1.2.1 Magnetism of Cr . . . 12
1.2.2 Frustration at Cr/Fe interfaces and spin glass formation . . . 13
1.3 Spin-orbit coupling . . . 14
1.4 Perpendicular magnetic anisotropy . . . 16

2 Superconductivity **17**
2.1 Fundamentals . . . 17
2.1.1 The two-fluid model and London theory . . . 17
2.1.2 BCS theory . . . 18
2.1.3 The proximity effect and Andreev reflection . . . 20
2.2 Josephson junctions . . . 22
2.2.1 The Josephson effect . . . 22
2.2.2 The RCSJ model . . . 22
2.2.3 Josephson junctions in a magnetic field . . . 23
2.2.4 Effect of size and current distribution . . . 25
2.2.5 S/N/S junctions . . . 26
2.2.6 S/N/S/N/S junctions . . . 27
2.3 Superconductor/ferromagnet interfaces . . . 28
2.3.1 The S/F proximity effect . . . 28
2.3.2 S/F/S Josephson junctions . . . 30
2.3.3 Pair-conversion at S/F interfaces . . . 30
2.3.4 Magnetically inhomogeneous interfaces . . . 31
2.3.5 Spin-orbit coupling . . . 32
2.3.6 Enhanced spin pumping with high spin-orbit coupling . . . 33

3 Methods **35**
3.1 Thin-film growth . . . 35
3.1.1 Substrate preparation . . . 35
3.1.2 Sputter deposition . . . 36
3.1.3 Thickness calibration . . . 38
3.2 Device fabrication . . . 39
3.3 Film microstructure and interface roughness . . . 43
3.4 Low-temperature transport measurements . . . 44
3.5 Magnetic characterization . . . 49
3.5.1 Vibrating sample magnetometry . . . 49

4 Effect of area and aspect ratio on ferromagnetic nanopillar Josephson junctions **51**
4.1 Nb/Py/Nb junctions . . . 51
4.2 Conclusions . . . 57

5 Josephson junctions with spin glass interfaces **59**
5.1 Nb/Cr/Fe/Cr/Nb junctions . . . 59
5.2 Conclusions . . . 64

6 Josephson junctions with spin glass interfaces and a superconducting interlayer **67**
6.1 Nb/Cr/Fe/Nb/Fe/Cr/Nb junctions . . . 67
6.1.1 Singlet-dominated interlayer junctions . . . 68
6.1.2 Triplet-dominated interlayer junctions . . . 74
6.2 Conclusions . . . 77

7 Josephson junctions with strong spin-orbit coupling **79**
7.1 Nb/Pt/Nb junctions . . . 79
7.2 Nb/Pt/Nb/Pt/Nb junctions . . . 83
7.3 Nb/Pt/Co/Pt/Nb junctions . . . 87
7.3.1 Magnetic characterisation . . . 87
7.3.2 Transport measurements . . . 92
7.4 Conclusions . . . 99

8 Josephson junctions with strong spin-orbit coupling and superconducting interlayers **101**
8.1 Nb/Cr/Fe/Nb/Pt/Nb junctions . . . 102
8.2 Nb/Pt/Nb/Py/Nb/Pt/Nb junctions . . . 107
8.3 Conclusions . . . 112

9 Summary and future works **113**
9.1 Overview . . . 113
9.2 Summary of experimental chapters . . . 114

A Josephson junctions with a ferromagnetic exchange-spring **117**
A.1 Nb/Py/Co/Py/Nb junctions 117
A.2 Conclusions 122

Bibliography **123**

List of figures

1.1 Splitting of the energy of spin-up and spin-down electrons in Fe 7
1.2 An illustration of a ferromagnetic hysteresis loop 10
1.3 Cartoon of spin frustration at an atomic step in a Cr/Fe interface 14
1.4 Magnetic phase diagram for CrFe alloys 15
1.5 Cartoon of spin glass formation due to interdiffusion and roughness at a Cr/Fe interface 15

2.1 Variation of the order parameter at an S/N interface 21
2.2 Scattering processes for quasiparticles at a N/S interface 21
2.3 Josephson junctions with the application of an in-plane magnetic field . 24
2.4 Idealized variation of critical current with magnetic flux in a rectangular Josephson junction 24
2.5 Andreev bound states in an S/N/S junction 27
2.6 Features of the behaviour of S/N/S/N/S Josephson junctions 28
2.7 Illustration of the exchange splitting of bands 29
2.8 Pair amplitudes at an S/F interface 29
2.9 Pair amplitudes at an S/F′/F interface 31

3.1 Illustration of the sputter deposition system 37
3.2 Schematic of the photolithography and FIB fabrication route 40
3.3 Illustration of the geometry during FIB nanofabrication 41
3.4 Schematic 3D model and SEM image of a fabricated nanopillar device . 43
3.5 Low-temperature transport measurement system 45
3.6 Differential resistance and $V(I)$ measurements of a nanopillar device . . 47
3.7 Definition of coordinates and dimensions for nanopillar measurements . 48
3.8 $I_c(H)$ dependence of a ferromagnetic nanopillar device 48
3.9 Schematic diagram of the VSM system used 49

4.1 Definition of measurement coordinates and dimensions of the nanopillar 52
4.2 I_cR_N and J_c variation with device area 53
4.3 I_cR_N and J_c variation with device aspect ratio 53
4.4 AR_N variation with device area and aspect ratio 53
4.5 I_c variation with device area and perimeter 54
4.6 Fraunhofer patterns for Nb/Py(3.4)/Nb devices 55
4.7 Nb/Py(5.3)/Nb devices of varying aspect ratio 56
4.8 I_cR_N against aspect ratio at different angles to the applied field 57

4.9 ΔH variation with aspect ratio 58

5.1 $V(I)$ characteristics for Nb/Fe(6)/Nb and Nb/Cr(1)/Fe(9)/Cr(1)/Nb . . 60
5.2 Decay of I_cR_N with thickness of ferromagnet d_{Fe} at 4.2 K 61
5.3 Decay of I_cR_N with thickness of ferromagnet d_{Fe} at 1.7 K 63
5.4 $I_c(H)$ dependence of the devices 65
5.5 Saturation magnetization and ΔH as a function of Fe thickness 66

6.1 I_cR_N dependence on the Nb interlayer thickness for Nb/Cr(1)/Fe(2)/ Nb'($d_{Nb'}$)/Fe(2)/Cr(1)/Nb devices 69
6.2 Area-resistance product against thickness of the Nb interlayer 69
6.3 $R(T)$ curves for a representative device at each Nb interlayer thickness . 70
6.4 Illustrations showing the supposed singlet pair amplitude 70
6.5 $I_c(H)$ dependence at each interlayer thickness 72
6.6 Decay of I_cR_N with thickness of the Nb interlayer 75
6.7 $I_c(H)$ dependence of the Nb/Cr(1)/Fe/Nb'/Fe/Cr(1)/Nb devices . . . 76
6.8 Illustrations of singlet and triplet pair amplitudes and $R(T)$ curves . . . 77

7.1 Decay of J_c with Pt thickness in Pt S/N/S junctions 81
7.2 Decay of I_cR_N with Pt thickness in Pt S/N/S junctions 81
7.3 AR_N variation in Pt S/N/S junctions 82
7.4 $I_c(H)$ for a Nb/Pt(34)/Nb junction 82
7.5 Comparison of junction length L from Fraunhofer fitting and SEM measurement 83
7.6 Variation of J_c, I_cR_N and AR_N with $d_{Nb'}$ in Nb/Pt/Nb/Pt/Nb junctions 85
7.7 $I_c(T)$ for patterned Nb/Pt/Nb/Pt/Nb devices 86
7.8 $R(T)$ curves for patterned Nb/Pt/Nb/Pt/Nb devices 86
7.9 $M(H)$ loops for unpatterned Nb/Pt/Co/Pt/Nb films 88
7.10 SQUID magnetometry of Nb/Pt/Co/Pt/Nb films 90
7.11 Remanent magnetization of unpatterned Nb/Pt/Co/Pt/Nb films 90
7.12 $M(H)$ loops for unpatterned Nb/Pt/Co/Pt/Nb films 91
7.13 Saturation moment per unit area plotted against Co thickness 91
7.14 I_cR_N, J_c and AR_N measured for varying d_{Pt} in Nb/Pt/Co/Pt/Nb devices 93
7.15 I_cR_N measured for a series of Nb/Pt/Co/Pt/Nb devices 94
7.16 $I_c(H)$ dependence of Nb/Pt/Co/Pt/Nb devices with d_{Pt} varying 95
7.17 $I_c(H)$ dependence of Nb/Pt/Co/Pt/Nb devices with d_{Co} varying 97
7.18 ΔH against d_{Co} and d_{Pt} in Nb/Pt/Co/Pt/Nb devices 98

8.1 I_cR_N, J_c and AR_N for Nb/Cr/Fe/Nb/Pt devices 104
8.2 I_cR_N measured for varying Fe thickness in Nb/Cr/Fe/Nb/Pt devices . 105
8.3 $I_c(H)$ dependence of Nb/Cr/Fe/Nb/Pt devices 105
8.4 $I_c(T)$ for Nb/Cr/Fe/Nb/Pt devices 106
8.5 Area dependence of I_cR_N for Nb/Pt/Nb/Py/Nb/Pt/Nb devices 107
8.6 I_cR_N, J_c and AR_N for Nb/Pt/Nb/Py/Nb/Pt/Nb devices 108

8.7 $I_c(T)$ and $R(T)$ for Nb/Pt/Nb/Py/Nb/Pt/Nb devices 110
8.8 $I_c(H)$ at $\phi = 0°$ and $\phi = 90°$ for a Nb/Pt/Nb/Py/Nb/Pt/Nb device . . 111
8.9 ΔH variation with aspect ratio 111

A.1 Saturation magnetization against d_{Py} for unpatterned Nb/Py/Co/Py/Nb films 118
A.2 I_cR_N, J_c and AR_N measured for varying d_{Py} in Nb/Py/Co/Py/Nb devices 119
A.3 $I_c(H)$ for Nb/Py/Co/Py/Nb devices 120
A.4 ΔH against d_{Py} for Nb/Py/Co/Py/Nb devices 120
A.5 $M(H)$ loops for unpatterned Nb/Py/Co/Py/Nb films 121

List of tables

3.1 Sputtering conditions used for the targets in this thesis 38

4.1 Hysteresis shift ΔH measured along perpendicular axes 57

5.1 Summary of fitting to decay data to estimate the decay length of triplets in Fe 63

7.1 Estimation of the normal state coherence length of Pt 80

8.1 Hysteresis shift ΔH in Fraunhofer patterns for Nb/Pt/Nb/Py/Nb/Pt/Nb devices 111

Symbols and abbreviations

Bold symbols indicate vector quantities; the same symbol in regular typeface may be used to mean the magnitude of the vector. Where the same symbol can take more than one meaning, the intended meaning should be clear from the context.

Roman symbols

a	inter-atomic distance
a, b	Landau parameters
A	device area
$\boldsymbol{B}$	magnetic flux density
C	capacitance
d	film thickness
d'	effective penetration thickness
$D(E)$	electronic density of states
$\boldsymbol{E}$	electric field
E_{ex}	exchange energy
E_{F}	Fermi energy
$\mathcal{F}$	free energy
g	dimensionless magnetic moment
g	S/N/S/N/S barrier strength
h	Planck's constant
$\hbar$	reduced Planck's constant
$\boldsymbol{H}$	magnetic field
$\boldsymbol{H}_{\mathrm{c}}$	coercive field
$\boldsymbol{H}_{\mathrm{ex}}$	exchange field
$\boldsymbol{H}_{\mathrm{mf}}$	Weiss molecular field
$\boldsymbol{H}_{\mathrm{R}}$	Rashba field
$\mathcal{H}$	Hamiltonian
I	current
I_{c}	critical current
J	exchange integral
J	current density
J_{c}	critical current density
$\boldsymbol{k}$	wavevector
k_{B}	Boltzmann's constant
$\boldsymbol{k}_{\mathrm{F}}$	Fermi wavevector
K	magnetic anisotropy constant
l	mean free path
L	device length
m	electron rest mass
m	magnetic moment
m_{s}	saturation moment
$\boldsymbol{M}$	volume magnetization
M_{r}	remanent magnetization
M_{s}	saturation magnetization
M_{s}	spin eigenvalues
n	number per unit volume
n_{s}	number of superconducting carriers per unit volum
q	generalized quantum coordinate
$\boldsymbol{Q}$	nesting wavevector
$\boldsymbol{r}$	position vector
R	resistance

R_N	normal-state resistance
$\boldsymbol{s}$	spin of an electron
$\boldsymbol{S}$	total spin of an electron pair
$\boldsymbol{S}_z$	spin projection on the z axis
t	time
T	absolute temperature
T_c	critical temperature
T_{Curie}	Curie temperature
T_G	Spin glass temperature
T_N	Néel temperature
v_F	Fermi velocity
V	voltage
W	device width
z	coordination number

Greek symbols

α_R	Rashba parameter
Δ	superconducting energy gap
$\Delta(H)$	hysteresis shift of $I_c(H)$
ϵ_0	permittivity of free space
θ	magnetization angle
θ	superconducting phase
λ	Weiss parameter
λ	London penetration depth
λ_J	Josephson penetration depth
μ_B	Bohr magneton
μ_0	permeability of free space
ξ	superconducting coherence length
ξ^0	clean limit coherence length
ξ_F	coherence length in ferromagnet
ξ_N	coherence length in normal metal
ρ	resistivity
ρ_s	number of Cooper pairs per unit volume
ϕ	spatial part of wavefunction
ϕ	measurement angle
Φ	applied flux
Φ_0	flux quantum
χ	spin part of wavefunction
ψ	wavefunction

Abbreviations

BCS	Bardeen-Cooper-Schrieffer
CPP	current-perpendicular-to-plane
F	ferromagnet
FIB	focused ion beam
IP	in-plane
LRT	long-ranged triplet
N	normal-state metal
OOP	out-of-plane
PMA	perpendicular magnetic anisotropy
R(C)SJ	resistively (and capacitively) shunted junction
S	superconductor
SDW	spin density wave
SEM	scanning electron microscope
SOC	spin-orbit coupling
SQUID	superconducting quantum interference device

Introduction

Rolf Landauer posited in 1961 that irreversible computational processes are necessarily accompanied by an increase in entropy. Known as Landauer's principle, this sets the lower bound on the energy efficiency of irreversible computation. However, the CMOS (complementary metal-oxide-semiconductor) technology of today expends around 1,000 times more energy per computation [1]. In addition, the drive to scale down logic elements in the current CMOS-based paradigm is reaching physical limits. The resulting desire to search for fundamentally different means of information processing has lead to multiple schemes grouped under the heading 'beyond CMOS'. One of these is spintronics; the utilisation of the spin degree of freedom of electrical currents, over and above simply manipulating charge flow.

The most widely used method to create spin-polarization for device applications is the injection of a current through a ferromagnet. Through this technique, Johnson and Silsbee first demonstrated a non-equilibrium magnetization in a paramagnetic metal, i.e. a spin accumulation [2]. Following soon after was the discovery of giant magnetoresistance (GMR), a large change in resistance dependent upon the relative magnetizations of magnetic layers separated by non-magnetic layers [3][4]. This is until now perhaps the most notable output of the field of spintronics; with Fert and Grünberg sharing the 2007 Nobel Prize in Physics and establishing a sensor technology which found widespread adoption in hard drive read heads.

Superconductivity would at first sight appear irrelevant to the field of spintronics. Consisting of Cooper pairs of opposite spin, it is not obvious how spin-polarization could be generated in the superconducting state. It is therefore perhaps surprising that prior to the work of Johnson and Silsbee, in the early 1970s, Tedrow and Meservey used ferromagnet/insulator/superconductor tunnel junctions to demonstrate that a spin-polarized current can be extracted from a ferromagnet, appearing as an asymmetry in the superconducting density of states [5]. As conventional spintronics became plagued by the need to generate very high current densities to produce technologically applicable effects, the superconducting state became attractive for its dissipationless nature. Superconductivity can greatly enhance phenomena from conventional spintronics; giant magnetoresistance becomes infinite magnetoresistance if the resistance can be switched off altogether through the magnetic configuration. Furthermore, the phase coherence of superconductivity offers entirely new ways of manipulating information compared with conventional spintronics. Superconducting spintronics has seen greatly increased research activity over the last decade, as multiple experiments demonstrated spin-polarized supercurrents, composed of triplet Cooper pairs [6].

In this thesis, I present the fabrication and measurement of nanopillar Josephson junctions incorporating spin-mixers and intermediary superconducting layers.

Chapter 1 reviews ferromagnetism, antiferromagnetism and spin-frustration at interfaces. Chapter 2 reviews superconductivity, Josephson junctions and superconductor/ferromagnet interfaces. The fabrication of nanopillar devices and the measurement techniques employed are discussed in Chapter 3.

The experimental results chapters commence with Chapter 5, describing the generation of long-ranged triplet (LRT) supercurrents with Cr/Fe spin glass interfaces. In Chapter 6, a superconducting interlayer is introduced to probe the propagation of the triplet supercurrent in a singlet superconductor. In Chapter 7, I attempt to observe the theoretically-predicted generation of the LRT via the combination of an exchange field and Rashba spin-orbit coupling with Pt/Co interfaces. Finally, I incorporate Cr/Fe interfaces and Rashba spin-orbit coupling from Pt in Chapter 8, in device structures where the aim is to 'open' a triplet channel through an intermediary superconductor, in an equilibrium analogue of the recent experiments of Jeon et al. [7].

Chapter 1

Magnetism

Magnetism in a condensed matter system is deeply intertwined with the spin angular momentum of the electrons. Ferromagnets will polarize charge currents while spin currents may exert torque on magnetic moments; effects utilized in spintronics.

Most generally, magnetism describes the response of a material to a magnetic field. Depending on the spin of electrons in the material, it may develop an opposing or co-directional induced field, termed diamagnetism and paramagnetism respectively. Some materials retain ordered magnetic states in the absence of an applied field, behaviours including ferromagnetism and antiferromagnetism. Some materials host a disordered, frustrated magnetic state known as a spin glass. To explain the wide range of magnetic phenomena observed in solid state systems, one must consider the occupation of electrons in atomic orbitals, the hybridization of these orbitals and formation of energy bands in a crystal.

The experimental work of this thesis is underpinned by the use of ferromagnetic and antiferromagnetic materials, and their competing interactions in the formation of spin glasses.

1.1 Ferromagnetism

Ferromagnetism is characterized by a material exhibiting a spontaneous magnetization in the absence of an applied magnetic field. The ferromagnets of interest in this work are the transition metals Fe and Co, and the alloy permalloy (Py), Ni-20wt%Fe; the origins of their magnetic behaviour will be developed in this section.

1.1.1 The Weiss molecular field

Models for ferromagnetism must include a mechanism which favours parallel alignment of electron spins. To this end, the Weiss model introduces effective molecular field $\boldsymbol{H}_{\mathrm{mf}}$, such that

$$\boldsymbol{H}_{\mathrm{mf}} = \lambda \boldsymbol{M} \tag{1.1}$$

where M is the magnetic moment per unit volume or the magnetization. Then, when we consider a ferromagnet containing many magnetic moments $\boldsymbol{S}$ in an applied field

$\boldsymbol{H}$ the Hamiltonian is

$$\mathcal{H} = g\mu_{\mathrm{B}} \sum_i \boldsymbol{S}_i \cdot (\boldsymbol{H} + \boldsymbol{H}_{\mathrm{mf}}), \tag{1.2}$$

where g is the dimensionless g-factor and μ_{B} is the Bohr magneton; the fundamental unit of magnetic moment. This is similar to the Hamiltonian for a paramagnet, except for the addition of the molecular field, which enables a spontaneous magnetization M in zero field.

A crucial postulate of the Weiss model is that there exists a molecular field, but it was not until the development of quantum mechanics that its origin could be explained. Hund's rules determine the ground state of a multi-electron atom. Hund's first rule states that for a given electron configuration, the lowest energy state is the one which maximizes the spin multiplicity. The highest occupied orbitals in Fe are the five degenerate 3d orbitals, among which six electrons must be distributed. The implication of Hund's rule is that the electrons will fill the 3d orbitals singly until all are occupied. This results in four unpaired electrons of the same spin and a net magnetic moment for the Fe atom.

The reason for this maximization of the spin multiplicity is given by a combination of Pauli's exclusion principle and electrostatic Coulomb repulsion. Initially, we will ignore the crystal structure and simply consider the pairing of two electrons. The wavefunction of two electrons can be considered as the product of a spatial component and a spin component. One and only one of these components must be antisymmetric with respect to particle exchange, since the overall wavefunction must be antisymmetric to obey the Pauli exclusion principle. Hence the spin state of the electrons determines their spatial state, and the spatial state with a larger separation of the electrons will be energetically favoured due to the Coulomb repulsion. This is the antisymmetric spatial component, which necessitates the symmetric (spin-aligned) spin state. Discovered independently by Heisenberg and Dirac, this effect is termed the exchange interaction, and provides the underlying reason for the favouring of parallel electron spins in ferromagnets.

1.1.2 The exchange interaction

The Heisenberg model of the exchange interaction is now presented more formally. The two-particle wavefunction can be written as

$$\psi(q_1, q_2) = \phi(\boldsymbol{r}_1, \boldsymbol{r}_2)\chi(\boldsymbol{s}_1, \boldsymbol{s}_2), \tag{1.3}$$

where q_1 and q_2 are the general coordinates of electrons 1 and 2 (the set of quantum numbers nlm). r_1 and r_2 are their spatial positions and σ_1 and σ_2 are their spin coordinates. Since the two electrons are identical fermions, the Pauli exclusion principle must be satisfied such that

$$\psi(q_1, q_2) = -\psi(q_2, q_1). \tag{1.4}$$

To satisfy this condition, we must choose one part of the wavefunction (spatial or spin) to be antisymmetric, and the other symmetric. Hence we have:

$$\psi(q_1, q_2) = \phi_{\mathrm{s}}(\boldsymbol{r}_1, \boldsymbol{r}_2)\chi_{\mathrm{a}}(\boldsymbol{s}_1, \boldsymbol{s}_2), \tag{1.5}$$

or

$$\psi(q_1, q_2) = \phi_{\mathrm{a}}(\boldsymbol{r}_1, \boldsymbol{r}_2)\chi_{\mathrm{s}}(\boldsymbol{s}_1, \boldsymbol{s}_2), \tag{1.6}$$

where

$$\phi_{\mathrm{s}}(\boldsymbol{r}_1, \boldsymbol{r}_2) = \frac{1}{\sqrt{2}}[\phi_1(\boldsymbol{r}_1)\phi_2(\boldsymbol{r}_2) + \phi_2(\boldsymbol{r}_1)\phi_1(\boldsymbol{r}_2)], \tag{1.7}$$

$$\phi_{\mathrm{a}}(\boldsymbol{r}_1, \boldsymbol{r}_2) = \frac{1}{\sqrt{2}}[\phi_1(\boldsymbol{r}_1)\phi_2(\boldsymbol{r}_2) - \phi_2(\boldsymbol{r}_1)\phi_1(\boldsymbol{r}_2)], \tag{1.8}$$

and

$$\chi_{\mathrm{a}}(\boldsymbol{s}_1, \boldsymbol{s}_2) = \frac{1}{\sqrt{2}}(\uparrow\downarrow - \downarrow\uparrow), \tag{1.9}$$

$$\chi_{\mathrm{s}}(\boldsymbol{s}_1, \boldsymbol{s}_2) = \begin{cases} \uparrow\uparrow & M_{\mathrm{s}} = 1 \\ \frac{1}{\sqrt{2}}(\uparrow\downarrow + \downarrow\uparrow) & M_{\mathrm{s}} = 0 \\ \downarrow\downarrow & M_{\mathrm{s}} = -1. \end{cases} \tag{1.10}$$

The possible spin states arise from the rules for the addition of angular momentum. Symbols $\uparrow$ and $\downarrow$ represent the two spin eigenstates for the individual electron spins. The four functions listed are linear combinations of product functions of the individual eigenstates, and are eigenstates of $\boldsymbol{S}^2$ (total spin) and $\boldsymbol{S}_z$ (spin projection on the quantization axis). The wavefunction χ_{a} has a total spin $\boldsymbol{S}^2 = 0$ and is called the singlet state, whereas the three functions χ_{s} have total spin $\boldsymbol{S}^2 = 1$ and are called the triplet states, with three possible projections on the quantization axis given by eigenvalues M_{s}. Loosely speaking, the singlet state corresponds to the two individual spins being oppositely directed, while the triplet states indicate spins pointing in the same direction. Note that although the triplet states always have $\boldsymbol{S}^2 = 1$, the projection on the quantization axis $\boldsymbol{S}_z$ may be zero. This distinction will be important when discussing superconducting triplet states, as a non-zero projection on the quantization axis is necessary to carry spin information in an experimental device.

Comparing the energy of wavefunctions 1.5 and 1.6, we find a difference in energy arising from the electron-electron interaction, termed the exchange energy $E_{\mathrm{ex}} = -2J$, where

$$J = \int\int \phi_1^*(\boldsymbol{r}_1)\phi_2^*(\boldsymbol{r}_2)\frac{e^2}{4\pi\epsilon_0 r_{12}}\phi_2(\boldsymbol{r}_1)\phi_1(\boldsymbol{r}_2)\mathrm{d}\boldsymbol{r}_1\mathrm{d}\boldsymbol{r}_2 \tag{1.11}$$

is the exchange integral.

For a many-electron system such as a metal, with atomic spins $\boldsymbol{S}_i$ on a lattice, the effective Hamiltonian is

$$\mathcal{H} = -2\sum_{i<j}^{N} J_{ij}\boldsymbol{S}_i \cdot \boldsymbol{S}_j \tag{1.12}$$

which incorporates the possibility for multiple exchange constants J_{ij} for higher order nearest-neighbour interactions. If only nearest-neighbour interactions are considered, then the sum over the constants J_{ij} simplifies to zJ, where z is the number of nearest neighbours or coordination number.

The exchange field H_{ex} is the effective field arising from the exchange interaction, analogous to the Weiss molecular field. It is given by

$$\boldsymbol{H}_{\text{ex}}(\boldsymbol{r}) = -\frac{1}{\mu_0}\frac{\delta E_{\text{ex}}}{\delta \boldsymbol{M}}, \tag{1.13}$$

and further we may link the Weiss parameter λ with the exchange integral J through the relationship

$$\lambda = \frac{2zJ}{ng^2\mu_{\text{B}}^2}, \tag{1.14}$$

where n is the number of spins per unit volume.

1.1.3 Influence of band structure

We must still account for two observations. Firstly, determination of the magnetic moment per atom for common metallic ferromagnets such as Fe results in non-integer multiples of the Bohr magneton. Secondly, we would predict all metals with unpaired electrons to show ferromagnetism. Both of these may be explained in terms of the effect of band structure, rather than dealing with isolated atomic magnetic moments.

In a crystal, the orbitals form bands, resulting in the loss of spherical symmetry. The orbital angular momentum no longer contributes significantly to the magnetic moment, which is borne mostly by the spin angular momentum. Furthermore, the band structure tends to favour spin neutrality. Consider a metal with an equal occupation of the spin-up and spin-down bands. Then, moving electrons from the spin-down band to the spin-up band would result in a net energy increase. However, upon introducing a molecular field as in the Weiss model, there is also an energy reduction to consider, which may outweigh the increase from the transfer between spin bands. Whether the overall energy change is favourable depends on the density of states at the Fermi energy $D(E_{\text{F}})$ and the strength of the molecular field λ (analogous to the exchange field), and is captured by the Stoner criterion, which states that

$$\mu_0\mu_{\text{B}}^2\lambda D(E_{\text{F}}) \geq 1 \tag{1.15}$$

must be satisfied for spontaneous magnetization to be favourable. The spontaneous energy splitting of the spin bands of Fe is illustrated in Fig. 1.1; for ferromagnetic materials, there is often a large peak in $D(E)$ around E_{F}. The transfer of electrons between spin bands to minimize the total energy will generally involve a non-integer number of spins per atom, explaining why we observe saturation magnetizations corresponding to non-integer multiples of the Bohr magneton per atom.

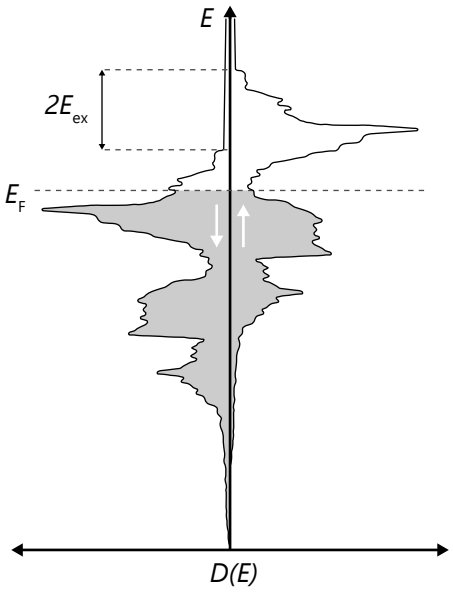


FIGURE 1.1: Splitting of the energy of spin-up and spin-down electrons in Fe. The transfer of electrons between spin bands is favourable for high exchange splitting E_{ex} and a high density of states around the Fermi energy E_F. Adapted from Cornwell et al. [8].

The Stoner criterion provides some justification for why ferromagnetism is relatively rare in the periodic table. Fe, Co and Ni have unpaired 3d electrons (and satisfy Stoner's criterion) and are ferromagnetic. Ru, Rh and Pd have unpaired 4d electrons, however the larger, more diffuse 4d orbitals result in wider bands which lead to a failure to satisfy Stoner's criterion.

It should be noted that no unified theory exists to explain ferromagnetism in the 3d transition metals. Some aspects of their behaviour are best treated with itinerant models, where electrons minimize their kinetic energy within the band structure (as in the Stoner model), and others are suited to localized models, where electrons minimize Coulomb repulsion through correlated motion (as in Heisenberg's direct exchange interaction). Hubbard attempted to reconcile these two approaches with a Hamiltonian including terms for both, which reproduces localized and itinerant behaviours in the two limits [9]. When dealing with large condensed matter systems such as metals, the itinerant approach is more applicable; however as we have seen, the localized models can provide straightforward insights which aid in understanding larger systems, so we will continue to refer to both as necessary.

1.1.4 Proximity-induced magnetism

Although none of the elements in the 4d and 5d blocks fulfil the Stoner criterion, some of them come close [10], which can lead to proximity-induced magnetism (PIM) [11][12]. Near an interface with a ferromagnetic material, Pt may develop a significant magnetic moment. Rowan-Robinson et al. [12] performed X-ray resonant magnetic reflectivity measurements on Pt/Co interfaces and interfaces split by a spacer layer

Pt/Au/Co. They found that the PIM decays rapidly and monotonically, vanishing around a spacer layer thickness of 1 nm.

1.1.5 Landau theory

The appearance of a spontaneous magnetization is a symmetry-breaking phase transition. The magnetization falls continuously to zero as T increases to the critical temperature T_{Curie}. As with the superconducting transition (to be discussed in Chapter 2), this is a second order phase transition. Landau developed a phenomenological theory for such phase transitions, requiring only an order parameter for the system and appropriate assumptions about the form of the free energy. In the case of ferromagnetism, the order parameter is the magnetization M, as it is the quantity which vanishes above the transition temperature. A suitable form for the free energy is

$$\mathcal{F} = \mathcal{F}_0 + a(T)M^2 + bM^4 \,. \tag{1.16}$$

Odd powers of M must have zero coefficients, since the energy should be the same regardless of the direction of the magnetization. The coefficient b must be positive, otherwise the free energy would be minimized for infinite M. Then we set $a(T) = a_0(T - T_{\text{Curie}})$ with a_0 positive so that the free energy is minimized at $M = 0$ for $T > T_{\text{Curie}}$. For $T < T_{\text{Curie}}$, two minima in the free energy arise for

$$M = \pm\sqrt{\frac{-a_0(T - T_{\text{Curie}})}{2b}} \,, \tag{1.17}$$

i.e. a finite magnetization which increases with decreasing temperature.

1.1.6 Magnetic anisotropy and hysteresis

Crystallographic symmetry plays an important role in ferromagnetism. The field required to align all the magnetic moments in a ferromagnetic material parallel depends on the direction chosen; the material is easier to magnetize along certain crystallographic directions (easy axes) and harder along others (hard axes). When an applied field is removed, the magnetization of a single crystal will revert to the closest easy axis. This is magnetocrystalline anisotropy. A simple case is that of uniaxial anisotropy, which has one easy axis, with the energy varying with magnetization angle θ as

$$E = K_1 \sin^2\theta + K_2 \sin^4\theta \,, \tag{1.18}$$

where K_1 and K_2 are anisotropy constants. This can be used to describe the hexagonal crystal system. If $K_1 > 0$ and $K_2 > -K_1$, the easy axis is the crystallographic c axis. This is the case for Co. If $K_1 > 0$ and $K_2 < -K_1$, the basal plane is an easy plane; i.e. we have infinitely many identical easy axes, lying in a plane. If $K_1 > 0$, $K_2 < 0$ and $0.5 < -K_2/K_1 < 1$, there is an easy cone. Each crystal system requires a separate equation. In Fe, with a cubic crystal structure, the easy directions are the $\langle 100 \rangle$ directions.

In addition to magnetocrystalline anisotropy, shape anisotropy is another contributor to the magnetic anisotropy of a sample. There is an energy cost associated with the magnetic field arising due to the magnetization of the material. This field is known as the stray field (since it pervades beyond the sample) or the demagnetizing field (since as with a bar magnet, the field generated will point from the N to S pole, against the magnetization of the material). The energy cost of the demagnetizing field will in general differ depending upon the direction of magnetization; it is less energetically costly to magnetize a rod along its length than across its width. For thin films, the shape anisotropy energy is

$$\frac{1}{2}\mu_0 M^2 \cos^2\theta\,, \tag{1.19}$$

where θ is the angle between the magnetization and the normal to the film. This shows that the energy can be minimized when the magnetization lies in the plane of the film.

A consequence of magnetic anisotropy is that there is in general an energy barrier to changing the magnetization of a ferromagnetic sample. Consider an idealized single magnetic domain in a field, magnetized along an arbitrary direction, with all magnetic moments parallel. On removing the field, the sample magnetization will rotate to the nearest easy axis to minimize its energy. If we then apply a magnetic field in the opposite direction, at low fields the magnetization will not change, and only will when the field is large enough to overcome the anisotropy energy.

Real ferromagnetic samples are often multi-domain, where each domain has its own magnetization shared by all the moments within it. The formation of a multi-domain structure lowers the energy of the demagnetizing field and so is typically favoured for samples larger than a few tens or hundreds of nanometres, depending on the material. Domains are separated by domain walls, which accommodate the change in magnetization by an in-plane rotation of the magnetization (Bloch domain walls) or an out-of-plane rotation of the magnetization (Néel domain walls). The domain wall thickness is determined by the change in magnetization which can be accommodated between each plane of magnetic moments. The exchange energy favours adjacent moments parallel, and in the absence of another energy term would unwind the domain wall. However, the magnetocrystalline anisotropy favours narrow domain walls, to minimize the energy cost of moments misaligned with the easy axis.

Consider the application of a magnetic field to a multi-domain ferromagnetic sample, with initial magnetization zero (the virgin state). Due to the random orientation of domains, some will already have a magnetization in a favourable orientation, i.e. a large component parallel to the applied field. The favourably oriented domains will grow by motion of the domain walls, sweeping over less favourably oriented domains. This process is much less energetically costly than the rotation of all the magnetic domains. The resulting structure will be dominated by a few large domains with magnetizations nearly aligned with the applied field. Complete alignment with the applied field requires domain rotation, where the magnetocrystalline anisotropy energy is overcome and the magnetization can rotate away from the easy axis to align

with the applied field. The result is a monodomain with all magnetic moments along the direction of the applied field. The sample is at saturation and its magnetization is M_s. If we then reduce the applied field to zero, multi-domain structure will be recovered with magnetizations along their nearest easy axes. This leads to a degree of preservation of the previously favoured directionality, and so the magnetization has not returned to zero, but rather to M_r, the remanent magnetization. Therefore, to return to zero magnetization, a field must be applied in the opposite direction. The field required to do so is called the coercive field H_c. Hence for a ferromagnetic material, the magnetization is not a single-valued function of the applied field, since it also depends on the magnitude and direction of fields applied previously. This behaviour is known as hysteresis. A plot of $M(H)$ exhibits a hysteresis loop, illustrated in Fig. 1.2 with the key parameters indicated.

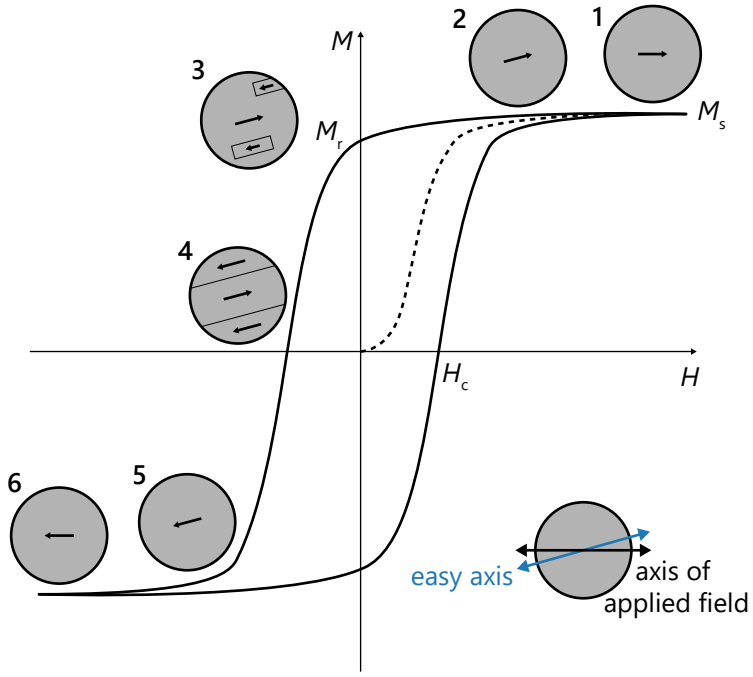


FIGURE 1.2: A schematic illustration of a ferromagnetic hysteresis loop $M(H)$. The dashed line indicates the virgin curve; the path followed for an initially demagnetized sample. Consider starting at (1) with a large applied field to the right. All the moments in the material (indicated by the small black arrow) are aligned to the field, hence we have a single domain and the magnetization is maximal at the saturation magnetization M_s. As the field is lowered, the magnetization returns to the easy axis (2). When the applied field is returned to zero, a multi-domain state (3) is obtained due to the nucleation of domains favourably oriented with respect to the applied field. The magnetization is now the remanent magnetization M_r. Applying a negative field will cause the growth of favourably oriented domains via domain wall motion. A negative field of $-H_c$ (the coercive field) must be applied to return the magnetization to zero (4). Increasing the field in the negative direction results in further growth of domains oriented in this direction, eventually resulting in a monodomain (5) whose magnetization is then pulled away from the easy axis to lie parallel to the applied field (6).

There are some important considerations specific to the nanopillar devices in this work, which will be discussed in the text as necessary:

- nanopillars have a size of a few hundreds of nanometres, and therefore are expected to be monodomain or close to monodomain;
- edge effects may cause a deviation from a perfect monodomain, e.g. curling or canting at the nanopillar walls;
- where there is more than one ferromagnetic layer in the pillar, the effect of stray fields on one layer from the other layers must be considered;
- Pt/Co bilayers and multilayers promote an out-of-plane easy axis.

1.2 Antiferromagnetism

The previous section presented the explanation that electrons lower their Coulomb repulsion by adopting a parallel spin state, through the exchange interaction, but this ignored the existence of atomic nuclei or a lattice. Heisenberg considered a direct exchange effect between two hydrogen atoms. He postulated that the sign of direct exchange (the J integral) can change with internuclear distance - if this distance is small enough, the electrons can lower their energy with respect to the electron-proton Coulomb attraction by adopting the singlet state, thereby reducing their average distance from the nuclei. If the nuclei are further apart, the electron-electron interaction becomes more important and so the triplet state is adopted as previously argued.

The consequence of a negative exchange integral J between two magnetic moments is that they will tend to align antiparallel to each other. This is the case in materials such as MnF_2 and Cr_2O_3, which may be described as two interpenetrating sublattices of equal and opposite magnetizations $\boldsymbol{M}_+$ and $\boldsymbol{M}_-$. Therefore, the net magnetization of such a material is zero in the absence of an applied field. This behaviour is termed antiferromagnetism.

Extending Heisenberg's direct exchange picture to the transition metals, the Bethe-Slater curve provides a framework in terms of the ratio of the inter-atomic distance to the radius of the 3d electron shell (a/r). This correctly predicts that Cr and Mn will have a negative exchange integral and hence be antiferromagnetic.

Reframing this in terms of the itinerant model, antiferromagnetism is mediated by the conduction electrons. A model for the mediation of the localized spins by the conduction electrons is called the RKKY interaction, after Ruderman, Kittel, Kasuya and Yosida who proposed it. They proposed an exchange interaction given by

$$J_{\mathrm{RKKY}}(r) \propto \frac{\cos(2k_{\mathrm{F}}r)}{r^3}\,, \tag{1.20}$$

where k_{F} is the magnitude of the Fermi wavevector and r is the separation of the two magnetic moments considered. Note that the sign of the exchange integral oscillates

with separation. Depending on the relation between the lattice and the period, this may give rise to aligned moments or alternately antiparallel moments, and so the model encompasses both ferromagnetism and antiferromagnetism.

The order parameter of an antiferromagnet may be defined as the difference in magnetization between the two sublattices $M_+ - M_-$, which is then non-zero below a temperature T_N, the Néel temperature.

If a magnetic field is applied to an antiferromagnet below T_N, the resulting behaviour is highly dependent upon the direction of the field relative to the sublattice magnetizations. If a field is applied perpendicular to $\boldsymbol{M}_+$ and $\boldsymbol{M}_-$, the magnetizations of both sublattices will rotate towards the direction of the field. This means there is a non-zero susceptibility, even at absolute zero. If a field is applied parallel to either $\boldsymbol{M}_+$ or $\boldsymbol{M}_-$, the local field experienced by one of these is increased and that for the other is reduced. For small fields, the lowest energy configuration is still with $\boldsymbol{M}_+$ and $\boldsymbol{M}_-$ antiparallel. However, at a sufficiently high field, the lowest energy configuration is a spin-flop phase. This is characterized by both $\boldsymbol{M}_+$ and $\boldsymbol{M}_-$ having a significant component in the direction of the applied field. At even higher fields, saturation will be reached with both $\boldsymbol{M}_+$ and $\boldsymbol{M}_-$ parallel to the applied field.

1.2.1 Magnetism of Cr

The magnetic behaviour of Cr is rich, and extensive reviews have been written on bulk Cr [13] and on Cr thin films and interfaces [14]. Here, we will briefly mention the general features but focus on the behaviour of Cr in thin films and at low temperatures, conditions relevant to this thesis.

While the Bethe-Slater curve from the localized theory correctly predicts Cr to be antiferromagnetic, the most important feature underlying the behaviour of Cr is found in the itinerant model and the Fermi surface. Large populations of electrons and holes at the Fermi energy have the same group velocity, and are separated in momentum space by a fixed wavevector $\boldsymbol{Q}$. This is known as Fermi surface nesting, and leads to a large magnetic susceptibility. At a critical temperature (the Néel temperature T_N), the antiferromagnetic transition breaks the translational symmetry given by the nesting vector $\boldsymbol{Q}$ and a gap opens at the Fermi level, accompanied by a fall in the density of states at this energy. The result is that the formerly conducting electrons and holes form bound states. The spin density then varies in an oscillatory fashion with wavevector $\boldsymbol{Q}$. This is known as a spin-density wave (SDW). Since $T_N = 311$ K [14] for Cr, this ordering is seen at room temperature.

We can compare the periodicity of this oscillation with that of the lattice by considering the magnitude of the SDW ordering wavevector $\boldsymbol{Q}$. $\boldsymbol{Q} = 0$ would imply no oscillation, corresponding to ferromagnetism, while $\boldsymbol{Q} = n\pi/a$ (with n an integer and a being the atomic spacing) results in antiferromagnetic ordering. In bulk Cr, $\boldsymbol{Q} \approx 0.96(2\pi/a)$ [15], so while the spin-density wave is not perfectly commensurate

with the lattice, the resulting ordering is essentially antiferromagnetic (with the additional complication that the magnitude of the magnetic moments varies spatially in an oscillatory fashion in addition to the antiparallel ordering).

However, in thin films, commensurate ordering can be seen. In this case, the corner atoms of the unit cell have an opposite spin to that in the body centre, hence the structure is simply alternating planes of opposite magnetization. In films with a thickness less than 4 nm (as in this thesis), commensurate ordering is favoured [14][16]. The commensurate phase has a higher T_N of 475 K [14] than the bulk incommensurate phase previously discussed. It should however be noted that the Cr films in this thesis are usually less than 1 nm thick, and therefore the SDW picture begins to lose physical meaning. The ordering will be further complicated by the roughness and interdiffusion present at sputtered interfaces.

1.2.2 Frustration at Cr/Fe interfaces and spin glass formation

We now move on to a consideration of Cr/Fe interfaces, which underpin much of the experimental work of this thesis. At such an interface, three types of exchange interaction are important: Cr-Cr, Fe-Cr, and Fe-Fe. Cr-Cr and Fe-Cr are both antiferromagnetic in nature, while Fe-Fe is ferromagnetic. For an idealized interface, these interactions are trivial to accommodate (Fig. 1.3 (a)), but roughness and interdiffusion will complicate this. These effects lead to a situation where not all the local exchange interactions can reach their energy minima; this is termed frustration.

As a model example, first consider an atomic step at a Cr/Fe interface. Fig. 1.3 (b) shows the frustrated state, and Figs. 1.3 (c-e) show possible ways that this frustration may be partially relieved. A domain wall might form in Fe (c) or in Cr (d) at the location of the step. Perhaps less intuitively, the SDW of Cr might reorient such that the individual layer magnetizations are now perpendicular to the interface (e), but if the spacing between atomic steps is small compared with the thickness of the Cr, this can be the favoured state [14]. The sputtered thin films of this work are relatively rough, but the Cr layers are generally very thin (only a few atomic layers), so it is not clear which of these configurations would be favoured.

In a real sputtered Fe-Cr interface, there is also likely to be a degree of interdiffusion and alloying. This gives rise to a complicated set of Cr-Cr, Fe-Cr, and Fe-Fe interactions with no trivial ground state configuration. Such a state is known as a spin glass, where two or more competing interaction mechanisms between magnetic moments preclude a global ground state being attained. Such a system has a number of metastable states for the spin configuration, with a range of small energy barriers between them, which may be accessed through the application of a magnetic field [17].

A spin glass phase is known to exist in the Fe-Cr system at temperatures below 50 K and with a molar fraction of Fe of around 0.2 [18]. In another study of a Cr-14%Fe alloy, a SDW state and a spin glass state were found to coexist, with $T_N = 65$ K and the spin glass existing below $T_G = 9$ K [19]. Burke et al. then explored the composition in detail to elucidate the magnetic phase diagram [20], which is presented in adapted

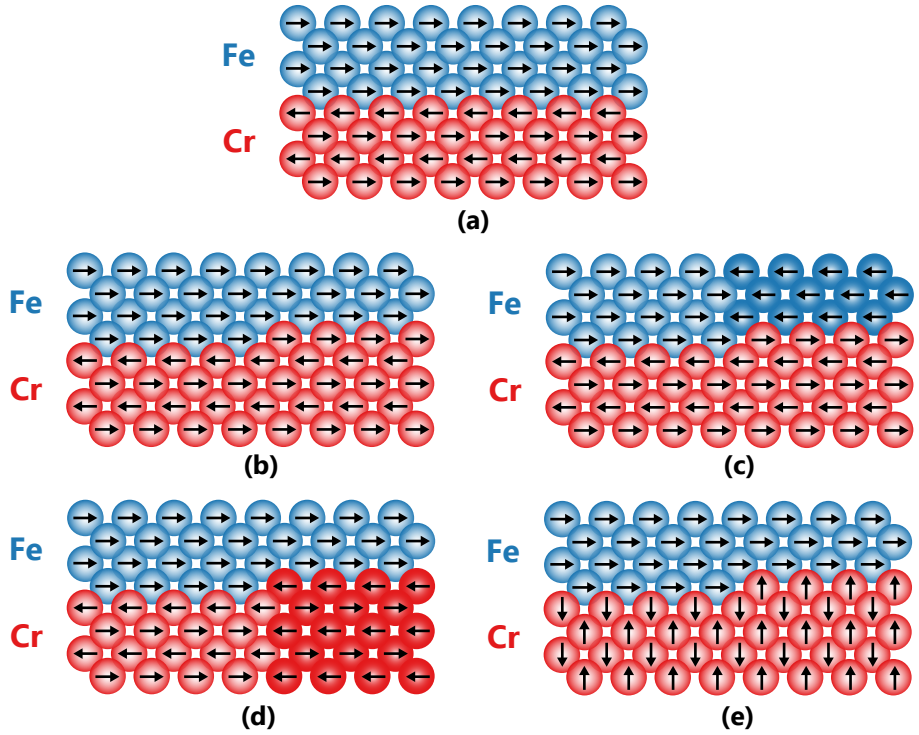


FIGURE 1.3: Cartoon of spin frustration at an atomic step in a Cr/Fe interface (adapted from Zabel [14]). (a) The ground state spin configuration with no step. (b) Upon introduction of a step, frustration arises as the antiferromagnetic Fe-Cr exchange is not satisfied. Some possibilities for configurations which may relieve the frustration are: (c) the formation of a domain wall in Fe; (d) the formation of a domain wall in Cr; (e) the reorientation of the SDW in Cr.

form in Fig. 1.4. With interfacial alloying, there are likely to be islands of such a spin glass state at sputtered Cr/Fe interfaces. Robinson et al. [21] demonstrated spin glass behaviour in a Fe/Cr multilayer stack through a measurement of the resistance as a function of applied field. $\mathrm{d}R(H)/\mathrm{d}H$ remained non-zero even as the applied field H was taken much higher than the saturation moment of the stack. This indicates the presence of frustrated moments at the interface which retain a finite angle with respect to the applied field even at fields much higher than the apparent saturation. A cartoon of frustration and spin glass formation at a Cr/Fe interface is presented in Fig. 1.5.

1.3 Spin-orbit coupling

Spin-orbit coupling (SOC) underlies many aspects of the devices in this thesis; in the following chapter it will be seen that SOC may rotate spins in the superconducting state. The subject is raised here as SOC is essential for the discussion of perpendicular magnetic anisotropy in the following section.

From the reference frame of an electron moving in an electric field, there is an effective magnetic field acting which couples to the spin (magnetic dipole) of the electron. This causes a splitting of the energy between spin-up and spin-down electrons. Spin-orbit coupling will therefore arise wherever there are local electric fields in a crystal or

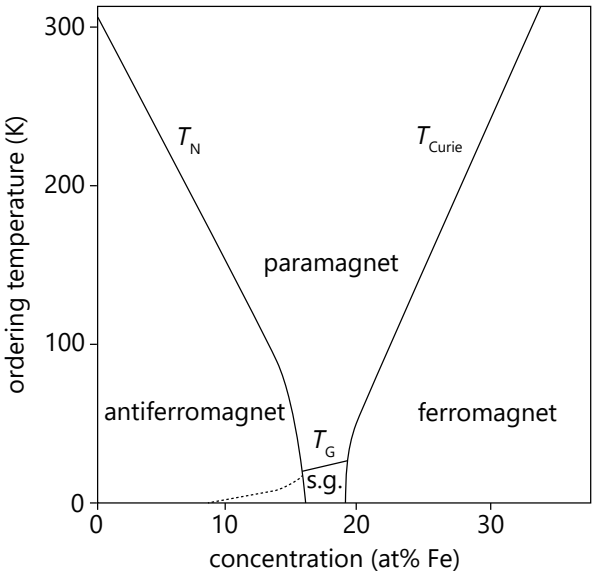


FIGURE 1.4: Magnetic phase diagram for CrFe alloys, adapted from Burke et al. [20]. The spin glass phase is denoted as 's.g.'. The dashed line shows the region where the antiferromagnetic and spin glass phases may coexist.

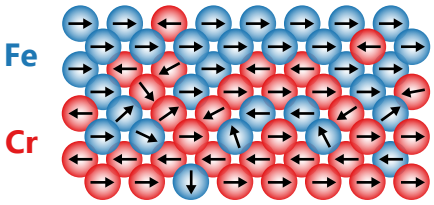


FIGURE 1.5: Cartoon of spin glass formation due to interdiffusion and roughness at a Cr/Fe interface.

multilayer structure. We can categorize SOC into symmetry-independent effects (due to atomic orbitals) and symmetry-dependent effects (due to a broken inversion symmetry). The latter can be further divided into SOC due to the crystal structure lacking inversion symmetry (a bulk effect, termed Dresselhaus SOC) or low dimensionality or interfaces between different materials (a surface effect, termed Bychkov-Rashba or just Rashba SOC).

The Rashba field $\boldsymbol{H}_{\mathrm{R}}$ is given by

$$\boldsymbol{H}_{\mathrm{R}} = \alpha_{\mathrm{R}}(\hat{\boldsymbol{z}} \times \boldsymbol{k}), \tag{1.21}$$

where α_{R} is a material parameter that quantifies the strength of spin-orbit coupling, $\hat{\boldsymbol{z}}$ is a unit vector in the direction of the local net field $\boldsymbol{E}$ due to the potential gradient in

the crystal or multilayer, and $\boldsymbol{k}$ is the electron wavevector. In the case of an interface, the local potential variation will be such that $\boldsymbol{E}$ is perpendicular to the interface. Conduction electrons moving perpendicular to $\boldsymbol{E}$ will rotate their spin towards the Rashba field vector $\boldsymbol{H}_{\mathrm{R}}$.

The strength of the Rashba SOC at an interface depends on the size of the local electronic potential gradient; this is large when there is a large difference of atomic number at an interface [22]. For this reason, incorporating layers of heavy elements such as Pt can provide high Rashba SOC.

1.4 Perpendicular magnetic anisotropy

Perpendicular magnetic anisotropy (PMA) describes the observation of an out-of-plane easy axis in a thin film, contrary to the in-plane anisotropy expected from the shape anisotropy. PMA is known to arise in a variety of systems, from crystalline Heusler alloys to amorphous CoFeB. Here, we will limit the discussion to PMA arising at interfaces, as this will be used in the experiments of this thesis.

There has been considerable interest in perpendicular magnetic anisotropy (PMA) in thin films for use in vertical magnetic recording systems to improve storage density, and more recently in spintronics for spin-transfer torque magnetoresistive random access memories. Néel was the first to propose that the origin of PMA was due to the broken symmetry at an interface [23]. Carcia et al. [24] found that PMA arises in Pd/Co thin film multilayers. The broken translational symmetry at an interface in a heterostructure gives rise to an asymmetry in the orbital angular momentum. This greatly increases the spin-orbit coupling at the interface. At the interface between a ferromagnet from the 3d group and a non-magnetic heavy metal from the 5d group, there will be strong hybridization of the ferromagnet 3d and heavy metal 5d orbitals. This causes a displacement of the d-orbital states in the ferromagnet at the Fermi level [25]. This distortion of orbitals near the interface creates strong spin-orbit coupling, favouring an alignment of the spin moment perpendicular to the interface [26]. This adds a uniaxial anisotropy term at the interface $-K_s(\boldsymbol{S}_i \cdot \hat{\boldsymbol{n}})^2$ (with $K_s > 0$) where $\hat{\boldsymbol{n}}$ is the unit normal to the plane of the interface. If this contribution to the anisotropy exceeds the thin-film shape anisotropy discussed previously, then PMA is attained.

It should be noted that interfacial strain also increases the interfacial anisotropy [27]. Bandiera et al. [28] found an asymmetry in the PMA at the two interfaces in a sputter deposited Pt/Co/Pt trilayer; where the bottom interface (Pt/Co) exhibited a higher PMA than the top interface (Co/Pt). This was attributed to interdiffusion at the top interface weakening the PMA. Roughness and interdiffusion will tend to reduce PMA [29].

In the next chapter, the potential roles of SOC and PMA at Pt/Co interfaces in causing spin-rotation of Cooper pairs will be described; such interfaces are employed in many of the experiments of this thesis.

Chapter 2

Superconductivity

Superconductivity is the phenomenon whereby a material exhibits zero electrical resistance below a critical temperature T_c, a critical magnetic field H_c and a critical current I_c. This was first observed in a sample of mercury by Kamerlingh Onnes in 1911. For spintronics, superconductivity offers dissipationless currents such that high current densities can be achieved. Furthermore, the coherence of the superconducting state offers new avenues in logic and memory.

Due to Maxwell's equations, a material of zero resistance cannot undergo any change in the magnetic flux density through it. However, the superconducting state has a further distinguishing feature; a material with a given magnetic flux density through it will expel this flux at the onset of the superconducting transition. This expulsion of magnetic flux from the material, enacted by screening currents, is known as the Meissner–Ochsenfeld effect.

The chapter will begin with a brief discussion of fundamental theoretical concepts necessary in describing the experimental work at hand. The Bardeen-Cooper-Schreiffer (BCS) theory is presented, which proceeds from a microscopic explanation of the behaviour of electrons forming paired states of opposing spin. Then, the Josephson effect is discussed, as measurements of Josephson junctions form the main experimental work of this thesis. As the goal of spintronics is to transport and manipulate spin currents for logic and memory applications, we are interested in converting the electron pairs of opposite spin to pairs with a net spin on the quantization axis. The methods for generating spin-triplet supercurrents will therefore be reviewed.

2.1 Fundamentals

2.1.1 The two-fluid model and London theory

Gorter and Casimir introduced a two-fluid model, splitting the density of electrons into a non-superconducting component and a superconducting component. The former is subject to scattering from the lattice and defects, while the latter was thought of as a superfluid and does not undergo any scattering. The fraction of superconducting electrons was assumed to grow from zero at the superconducting transition temperature to unity at absolute zero.

The London brothers took this two-fluid picture and introduced constitutive equations, which explain both the dissipationless current flow and the Meissner–Ochsenfeld effect. These equations were:

$$\frac{\partial \boldsymbol{J}}{\partial t} = \frac{n_s e^2}{m}\boldsymbol{E}, \tag{2.1}$$

and

$$\nabla \times \boldsymbol{J} = -\frac{n_s e^2}{m}\boldsymbol{B}. \tag{2.2}$$

$\boldsymbol{J}$ is the superconducting current density, n_s is the number density of superconducting electrons, e is the elementary charge, m is the electron mass, $\boldsymbol{E}$ is the electric field and $\boldsymbol{B}$ is the magnetic flux density. By applying Maxwell's equations, the two features discussed above emerge, along with a further subtlety; the magnetic flux does not become zero discontinuously at the material's boundary, but decays exponentially within a distance

$$\lambda(0) = \sqrt{\frac{m}{\mu_0 n_s e^2}} \tag{2.3}$$

at $T = 0$ K. λ is known as the London penetration depth. This is 39 nm for bulk Nb at 0 K [30], but in general the penetration depth will be larger than this; increasing the temperature, increasing scattering and reducing the dimensionality all increase this value. At T_c, the penetration depth diverges, but the variation from $\lambda(0)$ is small for $T/T_c < 0.5$ [31], a condition true for the majority of the measurements in this thesis. In the dirty limit, λ is dependent on the mean free path l between electron scattering events, such that $\lambda \propto l^{-1/2}$. In thin Nb films, a monotonic increase in λ is seen for reducing film thickness d_{Nb} [32]. This is due to the decreased T_c and the increase of the residual resistivity of the films as they are made thinner. In this thesis, we often take $\lambda = 90$ nm for Nb layers around 90 nm thick.

A further consequence of the London theory is that the magnetic flux through a superconducting loop must be quantized. This quantum of magnetic flux is given by

$$\Phi_0 = \frac{h}{2e} \tag{2.4}$$

where the appearance of $2e$ is the first hint that superconductivity is related to paired electrons.

2.1.2 BCS theory

Having discussed the phenomenological GL approach, we now discuss the microscopic theory of superconductivity proposed by Bardeen, Cooper and Schreiffer.

An important insight into the physics of superconductivity came in 1950, with a theoretical work by Fröhlich suggesting that the interaction of electrons with the ion cores in the metal may play a role in explaining superconductivity [33]. In the same year, it was found that the critical temperature of Hg was a function of the atomic mass M such that $T_c \propto M^{-\alpha}$ where the parameter $\alpha = 0.5$ for Hg [34] [35]. This dependence is termed the isotope effect and has been observed for many superconducting materials.

This confirmed that interactions between electrons and the lattice of ion cores were crucial in explaining superconductivity.

Cooper considered the introduction of a pair of electrons to the Fermi gas of a free electron metal [36]. He demonstrated that if an attractive interaction exists between the two electrons, the system would be unstable with respect to the formation of a bound state for this electron pair, henceforth referred to as a Cooper pair. The resulting model gave rise to an energy gap separating these bound states from excited states. An energy gap Δ was already known to be a feature of superconductivity from measurements of the electronic component of the heat capacity, which showed a dependence on a Boltzmann factor. It takes a value of around $\Delta_0 = 1.76\ k_B T_c$ for the common elemental superconductors [31], and is roughly constant at low T/T_c while the population of excited quasiparticles is low. Near T_c, Δ falls sharply to zero with a dependence given by:

$$\Delta(T) \propto \sqrt{1 - T/T_c}. \tag{2.5}$$

The role of the lattice and the need for an attractive interaction between the two electrons of a Cooper pair led Bardeen, Cooper and Schreiffer to construct a formalism appropriate to explaining many of the features of superconductivity [37]. They proposed a phonon-mediated interaction between the electrons of a Cooper pair. In rough terms, the action of an electron on the lattice of ion cores nearby is to cause them to displace from their equilibrium positions towards the electron. The resulting region of increased positive charge density will exert an attractive Couloumb force on a second electron. This simple picture may be described more formally as a phonon-mediated attraction between two electrons. This explains the observed isotope effect, and in addition it explains why superconductivity occurs at low temperatures or high pressures.

BCS theory yields expressions for the important length scales in a superconductor: the coherence length ξ, the length scale over which the order parameter ψ varies; and the penetration depth as introduced in the London theory. The BCS coherence length is given by

$$\xi_0 = \frac{\hbar v_F}{\pi \Delta}, \tag{2.6}$$

where v_F is the Fermi velocity. The subscript nought here refers to this being the coherence length that would be found in a pure, defect-free material (known as the clean limit). ξ_0 is defined as the length scale on which the superconducting order parameter can vary, but it may also be considered to describe the spatial extent of a Cooper pair.

In the free electron model at absolute zero, the probability of occupation falls sharply from one to zero on crossing the Fermi energy. However, the superconducting ground state emerging from the BCS theory shows a deviation from this, since the total energy can be reduced by forming bound states (i.e. Cooper pairs) until the pairing potential is insufficient to offset the occupation of higher energy states. The two electrons of a Cooper pair must have opposite momentum and opposite spin in order

to satisfy the Pauli exclusion principle. A Cooper pair has a net spin of zero, and may be treated as a boson. The ensemble of superconducting pairs may be considered as a Bose-Einstein condensate, sharing a common ground state and being described by a many-particle wavefunction.

The macroscopic superconducting wavefunction ψ (which may be identified with the energy gap Δ) can be written as

$$\psi = \sqrt{\rho_s}\exp(i\theta) \tag{2.7}$$

where ρ_s denotes the density of Cooper pairs (in the London theory, n_s referred to some density of superconducting carriers related with the electron density in some way) and θ is the superconducting phase, which is shared by all the Cooper pairs in the condensate.

We now consider excitations from the superconducting ground state. Supplying energy to a Cooper pair results in the formation of quasiparticles, which can be electron-like or hole-like. Breaking a Cooper pair means creating two excitations, at an energy cost of 2Δ. Hence incident photons on the superconductor must have $\omega \geq 2\Delta/\hbar$ to be absorbed. Consider the addition of one electron to a superconductor in the ground state. Since all possible Cooper pairs have already formed, the new electron must enter an excited state. We may define a superconducting density of states $D_S(E)$ as the number of excited states per energy interval available for occupation. We find:

$$D_S(E) = \frac{E}{\sqrt{E^2-\Delta^2}} D_N(E_F)\,, \tag{2.8}$$

where $D_N(E_F)$ is the normal density of states at the Fermi energy. Note that $D_S(E)$ diverges at $E = \pm\Delta$. The superconducting density of states can be probed experimentally through microwave absorption experiments, or quasiparticle tunneling experiments.

2.1.3 The proximity effect and Andreev reflection

Where a superconductor interfaces with another material, there will be a variation in the density of Cooper pairs, and a variation in ψ and Δ near the interface. At a superconductor/normal metal (S/N) interface, Cooper pair leakage into the normal metal will cause this metal to develop a non-zero value of Δ close to the interface (Fig. 2.1). This is known as the proximity effect. In the superconductor, Δ will fall from its bulk value close to the interface (the inverse proximity effect). These effects arise due to a scattering process involving Cooper pairs and quasiparticles at the interface known as Andreev reflection.

The variation within the superconductor is governed by the length scale ξ as defined previously. In the normal metal, the decay constant is ξ_N, given in the clean limit by:

$$\xi_N^0 = \frac{\hbar v_F}{2\pi k_B T}, \tag{2.9}$$

and in the dirty limit by:

$$\xi_N = \sqrt{\frac{\hbar v_F l}{6\pi k_B T}}. \tag{2.10}$$

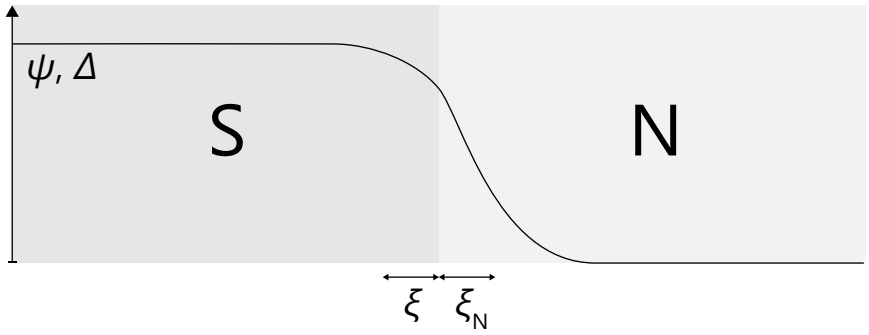


FIGURE 2.1: The variation of the order parameter ψ at an S/N interface, where ξ is the coherence length and ξ_N is the coherence length in the normal metal. The continuity of the wavefunction implies that there is no potential barrier at the interface; there will be a discontinuity at the interface in the general case.

Consider an electron with energy $E < \Delta$ encountering the N/S interface, illustrated in Fig. 2.2. It can be reflected, which incurs a relatively large momentum change of around $2k_F$. Alternatively, it can undergo Andreev reflection, where a hole is reflected from the interface with the opposite momentum and spin of the incoming electron. The momentum change is smaller; only $2E/\hbar v_F$ This net loss of two electrons from the normal metal is accompanied by the creation of a Cooper pair in the superconductor, which has zero energy (with respect to the Fermi energy) and where the electrons have opposite momentum and spin.

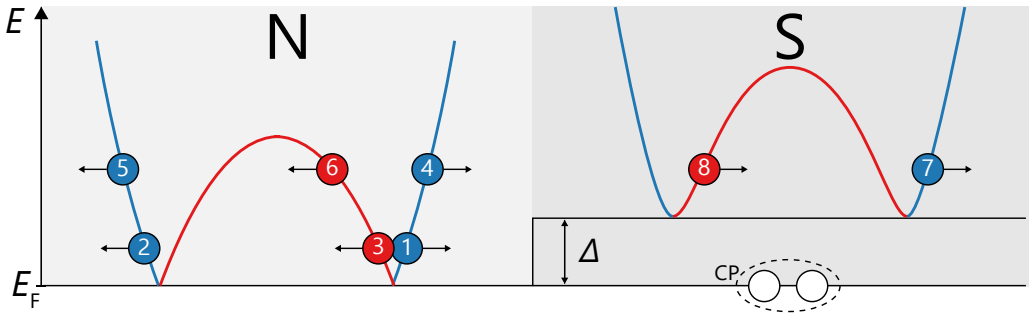


FIGURE 2.2: Scattering processes for quasiparticles at a N/S interface (adapted from Zagoskin [38]). Schematics of the quasiparticle band structure in both N and S are shown, with electrons in blue and holes in red. On the superconducting branch, quasiparticles have a mixed character (being electron-like or hole-like), and the blue and red indicate dominant electron-character and dominant hole-character respectively. Cooper pairs (CP) exist at the Fermi energy and are shown in white. Below the superconducting gap energy Δ, an electron (1) can be reflected (2) or Andreev reflected as a hole (3). Above the gap energy, an electron (4) can be reflected (5), Andreev reflected (6), or become a quasiparticle excitation in the superconductor (7), (8).

For an electron with energy $E > \Delta$ encountering the N/S interface, it can be reflected, Andreev reflected, or it can enter the superconductor as a quasiparticle excitation, with an electron-like character or a hole-like character.

2.2 Josephson junctions

2.2.1 The Josephson effect

In 1962, Josephson posited that Cooper pairs may tunnel elastically across a barrier [39] at zero junction bias. When two superconductors are joined by a non-superconducting weak link, such as an insulator, normal state metal or simply a physical constriction, the macroscopic superconducting wavefunction on each side of the junction may overlap, with locked phases, provided that the junction is sufficiently thin. This is termed a Josephson junction.

Josephson junctions may exhibit finite current flow at zero applied voltage (the d.c. Josephson effect) in accordance with

$$I = I_c \sin \phi \,, \tag{2.11}$$

where ϕ is the phase difference across the junction. This may be understood as the phase difference between the complex GL order parameters ψ on each side of the junction. I_c is the critical current of the Josephson junction. This is the maximum current that can be applied to the junction at zero voltage. Now consider the application of a finite voltage V to the junction. This causes a time-variation of the phase

$$\frac{\partial \phi}{\partial t} = \frac{2e}{\hbar} V \tag{2.12}$$

which in turn will cause an alternating current due to Equation 2.11. This is the a.c. Josephson effect.

2.2.2 The RCSJ model

To describe real device behaviour, one often considers a Josephson junction to be in parallel with a capacitance C and a resistance R, in the resistively and capacatively shunted junction (RCSJ) model. Hence the total current through the junction is given by

$$I = I_c \sin \phi + C\frac{dV}{dt} + \frac{V}{R} \,. \tag{2.13}$$

Solving this equation leads to a behaviour analogous to the motion of a ball on a 'washboard', a sinusoidal surface which may be angled such that the ball can roll above a critical angle of slope, the analogue of the critical current. The velocity of the ball is the analogue of the d.c. voltage, which is only-non zero above the critical current. The distance travelled by the ball is the analogue of the advancement of phase. Finally, we consider the ball to also incur a viscous damping force from a

surrounding fluid. The viscous damping is the analogue of the junction conductance, i.e. $1/R$. Junctions with a high conductance are said to be overdamped, and exhibit no hysteresis in their $V(I)$ characteristic ($V(I)$ as we are considering current-biased junctions). In the model, the velocity of the ball is a single-valued function of the angle of slope, independent of any previously applied angle of slope, since the viscous damping dominates over the inertia of the ball. This work deals with junctions that are well described by the overdamped limit. The characteristic voltage $I_c R_N$ is a useful measure of a Josephson junction, which is not dependent on the junction size. It can be related to the energy gap Δ through the BCS theory as

$$I_c(T)R_N = \frac{\pi\Delta(T)}{2e}\tanh\frac{\Delta(T)}{2k_BT}. \tag{2.14}$$

For the measurement and interpretation of $I(V)$ curves in this thesis, see Methods, Subsection 3.4.

2.2.3 Josephson junctions in a magnetic field

We now consider the application of a magnetic field in the plane of a Josephson junction. The field will penetrate the weak link, and will decay exponentially within the superconducting electrodes on the length scale of the penetration depth. The field gives rise to a gradient of the superconducting phase perpendicular to the field. We may integrate this to find the Josephson current, which we maximize with respect to an arbitrary constant term of phase arising from the integration. The resulting expression for I_c is periodic with the flux which passes through the junction:

$$I_c(\Phi) = I_c(0)\left|\frac{\sin(\pi\Phi/\Phi_0)}{\pi\Phi/\Phi_0}\right|, \tag{2.15}$$

where $\Phi_0 = h/2e$, the flux quantum. The flux through the junction as a result of the magnetic field is:

$$\Phi = d'L\mu_0 H, \tag{2.16}$$

where d' is the effective thickness of the junction and L is the junction length perpendicular to the applied field H. For the geometry of devices in this thesis, $d' = d + 2\lambda$, since the effective area penetrated by the flux is the physical barrier thickness d plus the London penetration depth on either side.

The variation of current density in the junction as a result of zero, one-half, and one flux quantum passing through the junction is sketched in Fig. 2.3. The resulting dependence of the critical current on applied field is sketched in Fig. 2.4. This is often referred to as a Fraunhofer pattern, after the intensity distribution from light diffracting through a single slit.

Experimentally, the measurement of a Fraunhofer pattern for $I_c(H)$ is regarded as definitive evidence of Josephson junction behaviour. The more uniform the junction, the better the fit to a Fraunhofer pattern will be.

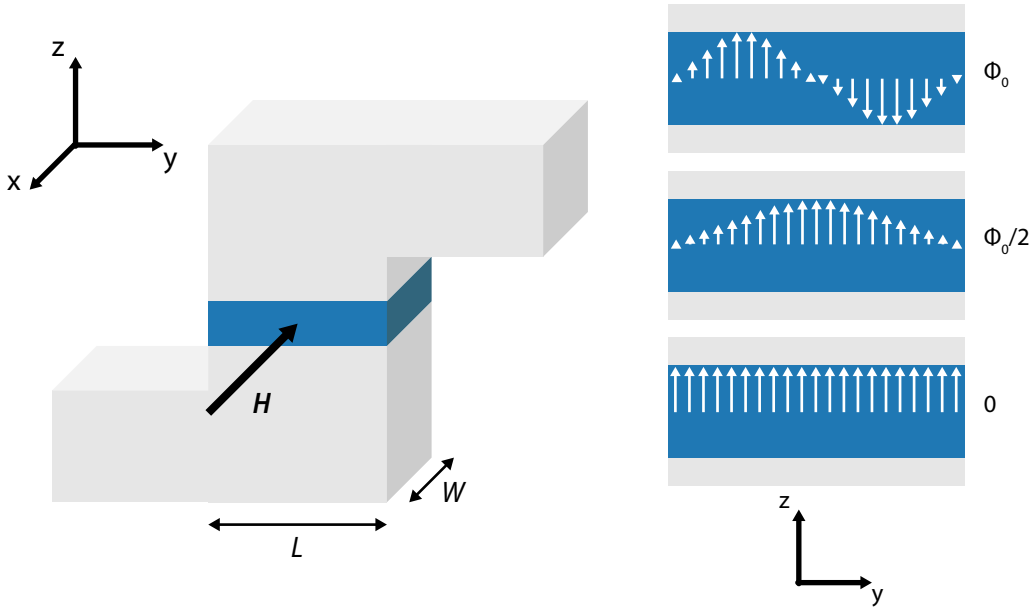


FIGURE 2.3: Behaviour of the current density in Josephson junctions with the application of an in-plane magnetic field. Left: A nanopillar Josephson junction of length L and width W, with a weak link indicated in blue (e.g. a normal metal) sandwiched between two superconducting electrodes, and the direction of application of magnetic field H defined. Right: Illustration of the current distribution across the junction for different values of flux through the junction, in terms of the flux quantum Φ_0. This shows how the applied flux gives rise to periodic oscillations in I_c.

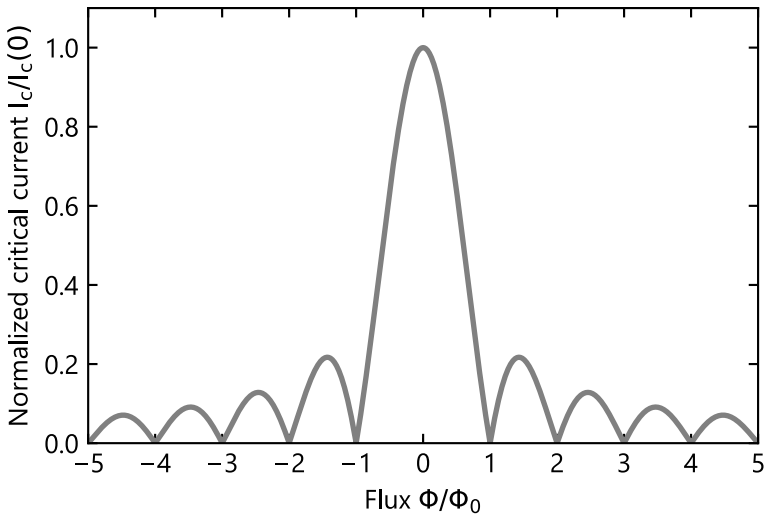


FIGURE 2.4: Idealized variation of critical current with magnetic flux in a rectangular Josephson junction, showing a Fraunhofer-like dependence.

2.2.4 Effect of size and current distribution

When treating the behaviour of a Josephson junction in a magnetic field, we assumed a uniform penetration of the magnetic field. This is only true if the junction is sufficiently small, with the Josephson penetration depth λ_J providing the length scale to determine this. It is given by:

$$\lambda_J = \sqrt{\hbar/2e\mu_0 J_c d'}, \tag{2.17}$$

where $J_c = I_c/LW$ is the junction critical current density, and $d' = d + 2\lambda$ as previously. If $L < \lambda_J$, the junction is in the short-junction limit. If $L \gg \lambda_J$, it is in the long-junction limit, with the consequence that the self-field generated by the current becomes significant, and the penetration of an applied magnetic field becomes non-uniform.

The modifications of Josephson junction behaviour due to self-field effects are presented in detail by Barone and Paternò [40]. The self-field effect will cause an asymmetric distortion in the Fraunhofer pattern; the central maximum will be found at a non-zero applied field which cancels the self-field due to the current. The current density in the junction becomes non-uniform; concentrated at the edges of the junction. As a result, the maximum Josephson current no longer scales linearly with the junction area but instead plateaus to a maximum value. These self-field effects are minimal at $L = \lambda_J$, with the non-uniformity of current density (suppression of current density below its value at the junction edges) only reaching 3%, while for $L = 4\lambda_J$ this non-uniformity reaches 35% [40]. This provides a guide as to where self-field effects should be considered non-negligible in the present work.

The devices in this thesis are for the most part in the short-junction limit. For devices with particularly high values of J_c, L becomes comparable with λ_J, and so self-field effects may begin to play a role. L ranges from around 150 nm to 700 nm in this thesis. For Nb/Pt/Nb devices with 23 nm Pt, $\lambda_J \approx 160$ nm, and for 77 nm Pt $\lambda_J \approx 500$ nm. The other device type which leaves the short-junction limit is the Nb/Py/Nb with thin Py of 1.6 nm, where $\lambda_J \approx 140$ nm. When the critical current densities are this large ($> 4\,\mathrm{mA}/\mu\mathrm{m}^2$) other issues are encountered, such as the entire pillar entering the normal state and the R_N of the junction disappearing in the differential resistance curves. Therefore, experiments were for the most part designed to give sufficiently small critical currents to avoid these issues, and so the short-junction limit can be assumed in most cases.

Another consequence of the device geometry in this thesis is that the additional flux penetration at the extremities of the junctions forms a significant contribution to the total flux. In deriving Equation 2.15, edge effects are ignored; the flux density is assumed to vary only along the z-direction of Fig. 2.3 and fall instantaneously to zero at $y = \pm L/2$. These edge effects may be expected to increase the total flux penetration in the nanopillar devices of this thesis.

In deriving Equation 2.15 it is assumed that the current density in the junction

is uniform. Barone and Paternò [40] treat several hypothetical current distributions. Along the analogy of the diffraction of light from a slit, the $I_c(H)$ pattern is simply the Fourier transform of the current density profile along the y-direction. Hence, the effect of a non-uniform current distribution can have effects such as changing how the amplitudes of the lobes decay with field, or introducing superposed oscillations. In general, Barone and Paternò found that when the current density is higher at the junction extremities than in the centre, the amplitudes of the subsidiary current lobes decay more slowly with increasing field. For the limit where all the current is carried in spikes as $\pm L/2$ from the junction centre, the lobes do not decay at all. Furthermore, where usually the distance between the two primary minima is twice that between subsidiary ones, the distance between all minima becomes the same (i.e. the central lobe of the pattern has been reduced to half its usual width). This particular current distribution is emphasized because Fraunhofer patterns approaching this behaviour are often seen in this thesis.

Barone and Paternò also considered the effect of random fluctuations in current density across the area of the junction, such as might be found due to roughness and microstructural defects. The most apparent effect of this is the presence of a constant background current independent of field, which means that I_c does not fall to zero at the minima, but to this background value. This effect is almost certainly present for the majority of the junctions in this thesis to differing extents.

2.2.5 S/N/S junctions

Although Josephson's original analysis was for junctions with an insulating barrier, De Gennes and Werthamer found that the same current-phase relation arises in the dirty limit for S/N/S junctions. When the weak link is a normal metal, the relevant length scale is ξ_N, previously introduced in Subsection 2.1.3 on the proximity effect. The critical current falls approximately as $I_c \propto \exp\{-d/\xi_N\}$ [31].

The high conductance (compared with insulating barriers) means that in the context of the RCSJ model, the damping is high. S/N/S junctions can usually be assumed to be overdamped, and so exhibit non-hysteretic $V(I)$ characteristics.

As discussed, Andreev reflection occurs at S/N boundaries. In an S/N/S Josephson junction with thickness of the N layer less than the phase coherence length, reflections at the two boundaries may maintain phase coherence and form Andreev bound states. This process is illustrated in Fig. 2.5. This requires that the total phase acquired around the closed path is an integer multiple of 2π.

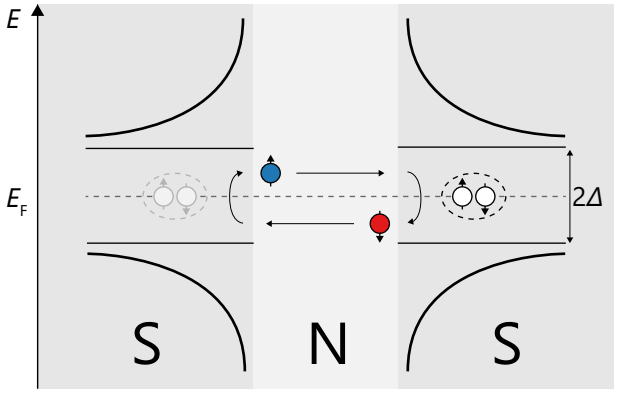


FIGURE 2.5: Andreev bound states in an S/N/S junction. Circles indicate electrons (blue), holes (red) and Cooper pairs (white). Arrows on the circles indicate the spin of the carrier. An electron with spin up travels to the right, and is Andreev reflected as a hole. A Cooper pair is created in the right-hand superconductor. The hole then travels left with spin down, where it is Andreev reflected. A Cooper pair is removed from the left-hand superconductor as a result, represented by the faint, greyed-out Cooper pair.

2.2.6 S/N/S/N/S junctions

Double-barrier Josephson junctions underpin many of the experiments of this thesis, as we are often interested in transport through intermediary superconducting regions.

A simple example is the S/N/S/N/S junction. When the thickness of the superconducting interlayer $d \gg \xi$, we simply obtain two non-interacting Josephson junctions, with the critical current being equal to that at either individual junction. A more interesting case is that where the thickness d is comparable to ξ or smaller. In this case, coherence is maintained between the two N barriers. Zapata and Sols [41] treat this situation assuming delta function-like barriers of strength g, where $g = L\xi(T)/\xi_N^2$, separated by a distance d. The spatial extent of the normal regions and microscopic Andreev reflection processes are ignored in this treatment. Fig. 2.6 shows quantitative results for the behaviour of critical current as a function of the distance d between the normal layers, and the contrasting temperature dependence near T_c for S/N/S and S/N/S/N/S junctions. Zapata and Sols predict that the $I_c(T)$ dependence of the junctions should decay as $\sqrt{T_c' - T_c}$ for S/N/S/N/S and $(T_c - T)^2$ for S/N/S junctions, where $T_c' < T_c$, i.e. the temperature at which I_c becomes zero is lower in the S/N/S/N/S case.

Chang and Chu [42] provided a theoretical treatment discussing Andreev-level tunneling and the current-phase relation, stressing that the central superconductor has a greater influence on the junction behaviour than the normal regions. The behaviour of the S/N/S/N/S junction can be explained through the coherence of the Andreev bound states, which is progressively lost as the spatial separation of the two N regions is increased, returning to simple S/N/S behaviour for $d \gg \xi$.

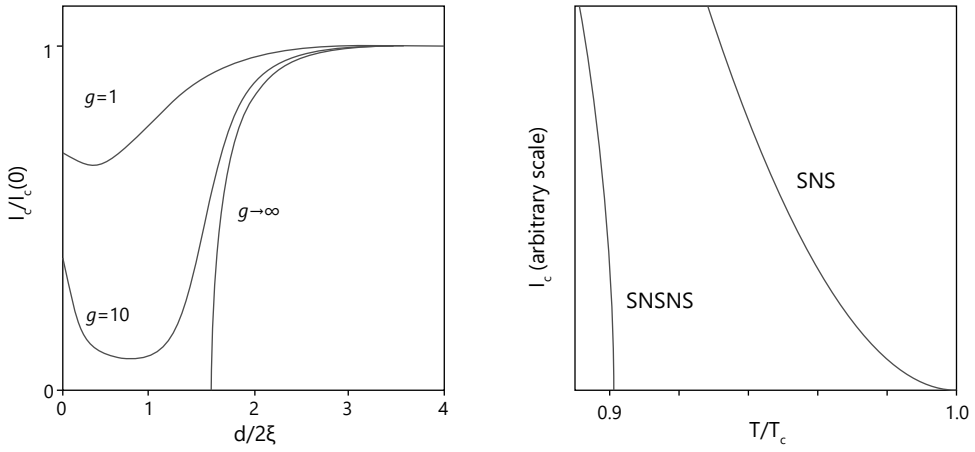


FIGURE 2.6: Features of the behaviour of S/N/S/N/S Josephson junctions, adapted from Zapata and Sols [41]. The paramater g quantifies barrier strength, where $g = L\xi(T)/\xi_{\mathrm{N}}^2$. Left: Critical current as a function of the distance d between the normal layers. Right: Temperature dependence near T_{c} for S/N/S and S/N/S/N/S junctions.

2.3 Superconductor/ferromagnet interfaces

2.3.1 The S/F proximity effect

Superconductivity and ferromagnetism are competing ordering phenomena in terms of spin; superconductivity favours electrons of opposite spin in the form of Cooper pairs, while ferromagnetism aligns electron spins. The exchange field of the ferromagnet breaks Cooper pairs, leading to a greatly reduced coherence length in a proximity-coupled ferromagnet ξ_{F} of just a few nanometres, compared with that in a normal metal.

Consider a Cooper pair entering a ferromagnet. The spin part of its wavefunction is in the singlet state, which may be represented as $\uparrow\downarrow - \downarrow\uparrow$ (omitting the normalization factor for convenience). In this notation, the first arrow of each term represents the spin of the first electron in a pair, and the second represents that of the second. The function is then antisymmetric with respect to exchange of the electrons. The exchange field of the ferromagnet causes a relative shift in the energy bands between spin-up and spin-down electrons (illustrated in Fig. 2.7). The wavevector $\boldsymbol{k}_{\mathrm{F}}$ is then different for spin-up and spin-down electrons, giving rise to a finite centre-of-mass momentum $\boldsymbol{Q}$ for the Cooper pairs. The spin wavefunction is then:

$$(\uparrow\downarrow - \downarrow\uparrow)\cos(\boldsymbol{Q}.\boldsymbol{R}) + i(\uparrow\downarrow + \downarrow\uparrow)\sin(\boldsymbol{Q}.\boldsymbol{R})\,, \tag{2.18}$$

where $\boldsymbol{R}$ is the position coordinate for the centre-of-mass of the Cooper pair. Since $\boldsymbol{Q}$ is perpendicular to the S/F interface, this leads to an oscillation of the pair amplitude with distance into the ferromagnet. In addition, a spin-zero triplet component

has appeared, also with oscillating pair amplitude, represented by the second term in Equation 2.18. The generation of superposed singlet and triplet pairing orders is termed spin-mixing, and the interface may be regarded as a spin-mixer.

Recalling Subsection 1.1.2, there were three possible states with total spin $S^2 = 1$, hence the term triplet. These differ in their spin projection on the quantization axis, (taken as the z axis here), taking values S_z = -1, 0, +1. Experimentally, the quantization axis is set by the direction of $\boldsymbol{M}$, the magnetization of the ferromagnet. Note that the triplet part of Equation 2.18 corresponds to $S_z = 0$, with no net spin along the quantization axis. Both the singlet and triplet component decay rapidly in the ferromagnet, due to the pair-breaking effect of the exchange field. An illustration of the variation of these components is given in Fig. 2.8. Propagation into the ferromagnet over a significant length scale requires the formation of spin-aligned triplet pairs ↑↑ and ↓↓, which are not subject to such pair-breaking.

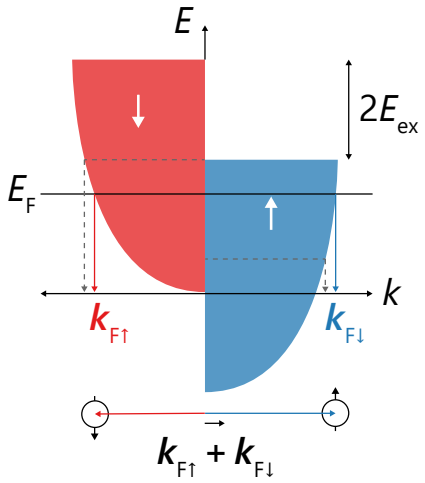


FIGURE 2.7: Illustration of the exchange splitting of bands for spin-up (blue) and spin-down (red) electrons. A Cooper pair (at the Fermi energy) acquires a net centre-of-mass momentum, illustrated by the small resultant vector in black from adding the red and blue vectors. Adapted from Eschrig [43].

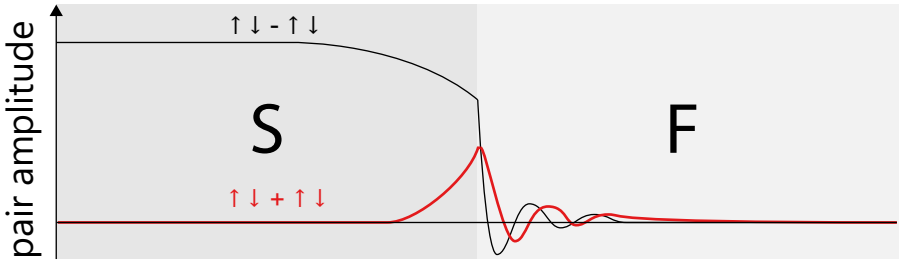


FIGURE 2.8: Schematic illustration of the spatial variation of the singlet (black) and spin-zero triplet (red) pair amplitudes in the vicinity of an S/F interface.

2.3.2 S/F/S Josephson junctions

As a consequence of the oscillating singlet pair amplitude in a ferromagnet, S/F/S Josephson junctions will exhibit oscillations in the critical current as a function of the thickness of the d_F layer. These are known as 0-π oscillations, since varying d_F switches the phase difference between the electrodes between 0 and π.

Further to the discussion of Josephson junctions in applied magnetic fields, we may consider how this behaviour will differ for S/F/S junctions. As the junction contains coupled magnetic flux even at zero applied field, there will be a shift of the Fraunhofer pattern $I_c(H)$ along the H axis. The flux Φ in Equation 2.15 can now be approximated as

$$\Phi = d' L \mu_0 H + d_F L \mu_0 M, \tag{2.19}$$

where d_F is the thickness of the ferromagnetic layer. The second term results in the shift of the Fraunhofer pattern. As M is a function of H, there may further modifications of the pattern; for example a reduction of the period between the minima in the pattern in the region of magnetization reversal. Additionally, any non-uniformity of the magnetization will cause further deviations from the expected absolute-sinc-function form. This is discussed in more detail in the experimental chapters of this thesis on a case-by-case basis.

2.3.3 Pair-conversion at S/F interfaces

In addition to spin-mixing, a spin-rotation step is required to convert the spin-zero triplet pairs into spin-one triplet pairs, with a spin projection along the magnetization direction of the ferromagnet. Unlike the singlet state, the three triplet states are not rotationally invariant, hence spin-rotation can interconvert the triplet states. Theoretical work by Bergeret, Volkov and Efetov [44][45] proposed that this would happen in S/F systems with the addition of magnetic moments at the interface which were misaligned with that of the bulk ferromagnet.

Consider an S/F′/F interface where F′ is an additional interfacial layer, with magnetization perpendicular to that of F. By the preceding arguments, a spin-zero triplet state $\uparrow\downarrow + \downarrow\uparrow$ will form due to the exchange splitting of F′. This state is equivalent to a superposition of the spin-aligned triplet states when viewed along a perpendicular quantization axis, i.e. $\uparrow\uparrow + \downarrow\downarrow$. The perpendicular magnetization of the F layer provides such a quantization axis, hence a spin-aligned triplet pairing amplitude can extend into F over a significant length scale (Fig. 2.9), comparable to that of singlet pairs penetrating normal metals. These pairing correlations will be termed the long-ranged triplet (LRT) in this thesis.

To obey the Pauli exclusion principle, electrons in Cooper pairs must have an overall antisymmetric wavefunction with respect to particle exchange. The wavefunction may be considered as the product of a spatial, spin, and temporal part. Conventional superconductors with singlet Cooper pairs have the spin part antisymmetric.

In the case of triplet pairing, it is found that the temporal part becomes antisymmetric. Hence this is often called odd-frequency superconductivity.

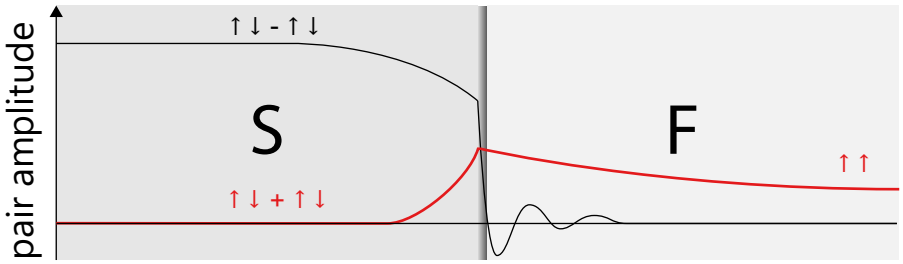


FIGURE 2.9: Schematic illustration of the variation of the singlet (black) and triplet (red) pair amplitudes for the case of a thin interfacial layer of magnetization perpendicular to that of the bulk ferromagnet. Spin-one triplet correlations are generated, which have a long range in the ferromagnet.

2.3.4 Magnetically inhomogeneous interfaces

Prior to the development of the theoretical insights regarding spin-mixing and rotation, in the late 1990s, two groups [46] [47] measured S/F proximity effects on considerably longer length scales than the expected ξ_F. This led Bergeret, Volkov and Efetov [44] to explain the results in terms of transport by a long-ranged triplet component generated by an inhomogeneity in the magnetization at the interface, such as a domain wall.

Eschrig et al. undertook theoretical studies of S/F/S junctions (where F is a half metal, i.e. it has 100% spin polarization), demonstrating that an indirect Josephson effect would be induced through triplet correlations generated by spin rotation [48]. The first evidence of the generation of a long range triplet supercurrent in a Josephson-type S/F/S device was by Keizer et al. [49]. The ferromagnet in this case was the half-metal CrO_2. There was a large variation in device behaviour, attributed to lack of control of the magnetic inhomogeneity generating the triplet supercurrent.

In the search for a controllable means of generating a magnetic inhomogeneity at an S/F interface, attention turned to the conical ferromagnet Ho [50], which has an intrinsic rotation of the magnetization between atomic layers. This structure is similar to a Bloch domain wall, except for the additional out-of-plane component of the magnetization.

Houzet and Buzdin predicted that in a ferromagnetic trilayer F′/F/F″, where F′ and F″ have magnetizations non-collinear with that of F, a long range triplet supercurrent could be supported [51]. Robinson et al. [52] verified this experimentally using a trilayer of Ho/Co/Ho between Nb electrodes, where the conical magnetization of Ho provides a reliable means of introducing the required non-collinear magnetization. The decay in the Josephson critical current with increasing thickness of Co was

found to be far slower than in control experiments without the Ho layers, meaning that a supercurrent propagates in the Co over distances much greater than the singlet coherence length (around 1 nm) and instead comparable with the decay length in a non-magnetic metal. This suggests electrical transport through a triplet supercurrent. The critical current varied in a non-monotonic fashion as the Ho thickness was varied, reaching maxima where the Ho thickness corresponded to a half-integer number of spiral wavelengths. This had been predicted in calculations [53] which were then further developed [54]. Furthermore, the group demonstrated a Fraunhofer-like dependence of the critical current on the applied in-plane field, providing firm evidence of coherent Josephson coupling through the junction. Another experimental work showed that large enhancements in critical current could be achieved by control of a Bloch domain wall in Ni/Gd/Ni, depending on Gd layer thickness and field annealing [55].

Khaire et al. [56] studied S/F′/F/F′/S structures, where F′ is a weakly ferromagnetic alloy such as PdNi or CuNi and F is Co. They too observed a slow decay in critical current in measurements for Co thicknesses of 12 nm-28 nm (indicative of triplets), as well as a Josephson effect. The authors posit that the required magnetic inhomogeneity for generation of the triplet supercurrent arises due to the interplay of domain size, magnetocrystalline anisotropy and shape anisotropy in the F′ layers. These competing factors may give rise to non-collinear magnetizations of the type discussed by Houzet and Buzdin. The group later showed [57] that an enhancement in the critical current by a factor of 20 could be achieved if the magnetization of the F′ layers was made almost perpendicular to that of the F layers. This emphasized the importance of non-collinearity of magnetization at the interface to generate the triplet component efficiently.

Robinson et al. [21] used Cr/Fe interfaces as spin mixers. As described in Subsection 1.2.2, such interfaces host an inhomogeneity in the form of a spin glass. In Nb/Cr/Fe/Nb nanopillar current-perpendicular-to-plane devices, a non-monotonic decay in the critical current is observed with Cr thickness, providing evidence of enhanced triplet generation at particular Cr thicknesses, which can be related to the length scale of the spin density wave state of Cr. Furthermore, the decay of I_c with Fe thickness is shown to be slower in Nb/Cr/Fe/Cr/Nb than in either Nb/Fe/Cr/Fe/Nb or Nb/Fe/Nb, providing evidence for the generation of spin aligned triplet pairs. The use of this structure and comparisons with the data of Robinson et al. can be seen in Chapter 5.

2.3.5 Spin-orbit coupling

After the generation of long-ranged triplet correlations through a magnetic inhomogeneity, Bergeret and Tokatly [58] demonstrated that spin-orbit coupling (SOC) offers an alternative method of generating such triplet pairs. Rashba SOC, arising at certain interfaces, was introduced in Section 1.3 of the previous chapter; a key point was that conduction electrons moving perpendicular to the potential gradient due to the

interface will rotate their spin towards the Rashba field vector $\boldsymbol{H}_{\mathrm{R}}$. This effect can lead to the rotation of triplet Cooper pairs, and hence provide an alternative for the spin-rotation step than the magnetic inhomogeneities previously described.

Bergeret and Tokatly [58] demonstrated that spin-orbit coupling (SOC) can generate long-ranged triplet (LRT) correlations, even in diffusive systems. They propose that this may be the main source of triplet generation in lateral S/F/S devices, where only Rashba SOC at the S/F interface is needed, independent of magnetization direction. In multilayer transverse structures (as in this thesis), the condition for triplet generation is more stringent. If the magnetization is in-plane (common for thin films), both Rashba and Dresselhaus SOC are required, and the two components of magnetization in the plane must differ.

However, if the magnetization is out-of-plane, only a pure Rashba SOC is required to generate the LRT. Jacobsen et al. [59] expanded upon this theory, presenting an S/N/F/N/S device, where the N layers are heavy metals and F is a single, homogeneous ferromagnet where the magnetization has an out-of-plane component. Furthermore, they find that the LRT is immune to spin-flip processes, and charge and spin currents can be tuned separately through the superconducting phase difference. These characteristics are highly promising for spintronics applications.

2.3.6 Enhanced spin pumping with high spin-orbit coupling

With growing interest in the relationship between SOC and spin transport in the superconducting state, evidence of enhanced spin transport mediated by SOC was observed in a different kind of experiment to the ones discussed thus far.

Jeon et al. [7] performed a dynamic ferromagnetic resonance (FMR) experiment on Nb/Py/Nb trilayers, where a precession of the magnetization of Py causes spin-pumping into the Nb layers. The FMR spectrum linewidth is a measure of the flow of spin angular momentum from a ferromagnet into an adjacent material, related to the Gilbert damping of the precession. Above T_{c}, Nb/Py/Nb trilayers show an increased linewidth compared with Py alone due to spin absorption in the Nb. For a given trilayer, the linewidth decreases as the temperature is lowered below T_{c}, as the opening of the superconducting gap blocks spin transport. When Pt layers (5 nm thick) are added symmetrically about the trilayer, the behaviour is dramatically different, showing an increase of linewidth below T_{c} compared to that above T_{c}. This effect is only observed for Nb thicknesses shorter than the coherence length, and is at its strongest around 30 nm. Hence spin transport is now enhanced, rather than inhibited in the superconducting state. Other heavy metals W and Ta were substituted with Pt which also resulted in an enhancement of the spin-pumping, while control materials such as Cu did not.

The enhanced spin-pumping was attributed to a spin-triplet supercurrent, generated through a combination of the exchange field and the SOC at the heavy metal layers. This recent result is highly promising for spin-transport in superconductors, but still leaves many questions about the precise details of the spin transport.

Chapter 3

Methods

This chapter outlines the methods used to create the Josephson junction devices in this thesis, as well as the characterization and measurement techniques employed.

For all the devices in this thesis, the aim is to make a device in which current must pass between two Nb electrodes across intermediary layers which constitute the weak link of the Josephson junction. The weak link will usually be referred to as the barrier in this thesis (however it should be noted that there are no tunnel barriers in this work). Such a barrier may consist of one or more layers and be composed of normal metals, ferromagnets and intermediary superconductors. To fabricate such devices, I use sputter deposition to obtain a thin-film multilayer with relatively thick Nb layers top and bottom. Photolithography is used to define contact pads and a micron-scale region (henceforth referred to as the 'track'). The track can then be patterned into the finished device with a focused ion beam system. To define the current path incorporating the weak link, two slot cuts must be made through the two Nb electrodes to leave a current-perpendicular-to-plane device.

An advantage of using FIB (rather than multiple lithography steps) is that the whole multilayer can be deposited without the need to break vacuum, hence interface quality is more easily optimized [60].

Finally the setup and methodology of the low-temperature electrical transport measurements will be discussed.

3.1 Thin-film growth

3.1.1 Substrate preparation

The substrates in this work are (100) oriented Si with a 250 nm-thick SiO_2 thermally grown surface layer. With the aid of scores on the underside made with a diamond scribe, the wafer is cleaved into 10 mm by 5 mm pieces. The substrates are then cleaned. First, the substrates are immersed in acetone under ultrasonication for 5 min. Then, they are rinsed with isopropanol before being immersed in isopropanol for a second ultrasonication for 5 min. After a final isopropanol rinse they are dried with a nitrogen gun.

3.1.2 Sputter deposition

The thin-film multilayers in this work were deposited by d.c. magnetron sputter deposition. In this technique, a high voltage is applied to a metal target in a chamber containing a low pressure of Ar gas. The voltage generates a plasma from the gas, with the resulting Ar ions bombarding the negatively-biased target. This causes ejection (sputtering) of atoms from the target. The flux of sputtered atoms has a low degree of directionality, and will form a coating over a wide angular range. It is thus necessary to use a mask to achieve the desired deposition onto the substrate. For this work, rotating the substrates on a turntable underneath a simple slot-shaped mask suffices, where deposition only happens while the substrate is in the line-of-sight of the target (neglecting indirect scattering around the mask). By use of a motor, it is possible to set a precise rotational speed, such that the total flux received at the substrate, and hence film thickness, is controllable. A schematic of the sputter deposition system used in this work is shown in Fig. 3.1.

The application of a large negative bias voltage to the target is sufficient to ionize the sputtering gas, however, this work additionally uses a magnetic field near the target - hence 'magnetron' sputter deposition. Targets are mounted to a holder containing a samarium-cobalt magnet. During sputtering, this has the effect of confining electron motion near the target through the Lorentz force. Electrons may be described as 'hopping' along the target surface. This leads to a higher rate of ionization of the Ar in this region and therefore an increased sputtering efficiency. The rectangular cross-section of the magnet causes the localization of electrons (and hence a localization of ion bombardment on the target) to a 'racetrack' shaped locus. The system used allows for up to six sputtering targets to be mounted for a deposition. Separators confine the flux, avoiding unwanted deposition and contamination of other targets. This enables several metals to be deposited in the same run to form a multilayer heterostructure. Each target is allowed to sputter for around 10 minutes before deposition onto the substrate, in order to minimize the incorporation of surface oxides or impurities into the film.

The deposition is performed under constant power (current-voltage product) by a power supply unit. Table 3.1 shows the conditions used for each metal target. A wider mask slot is used for Nb to allow faster deposition. In all cases, pressure is 1.5 Pa and the target-substrate distance is 50 mm. The pressure is controlled by setting a dynamic equilibrium with the needle valve allowing Ar gas into the chamber, and gas leaving the chamber through the gate valve to the turbomolecular pump.

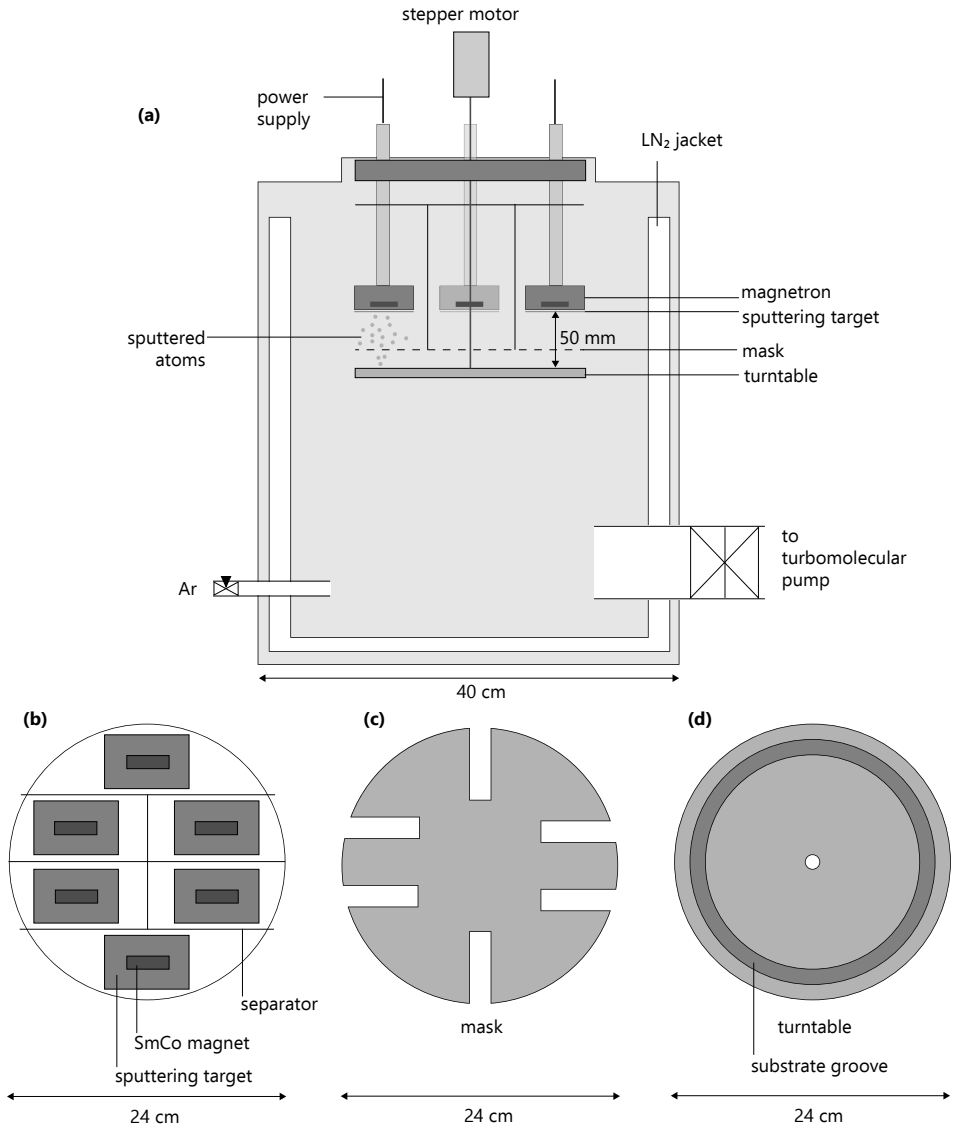


FIGURE 3.1: A schematic illustration of the sputter deposition system: (a) the vacuum chamber with Ar inlet through a needle valve, a gate valve to a turbomolecular pump, LN_2 jacket, and a loaded flange with magnetrons and the sample turntable, controlled by a stepper motor; (b) top-view of the magnetrons and separators; (c) top-view of the mask; (d) top-view of the turntable.

Before each deposition, the chamber is pumped and baked by a heating tape for at least 12 hours to remove contaminants which may outgas during deposition (mainly water). Furthermore, the chamber has an outer jacket which is filled with liquid nitrogen during deposition. This significantly reduces the pressure of any remaining gases by causing them to condense on the chamber walls. A base pressure of 2×10^{-9} mbar or better can then be achieved.

TABLE 3.1: Sputtering conditions used for the targets in this thesis. Sputtering is performed at constant power, and the current and voltage reflect the typical values under self-sustaining discharge under 1.5 Pa Ar atmosphere. The angular range is that which the turntable rotates through while the substrate is in the line-of-sight of the sputtered flux. The mask slot width is identical except for Nb, where a wider slot facilitates faster deposition. The deposition rate used in practice for this setup is measured in nm×rpm/W, since rotation at a given angular speed past the slot should always result in the same deposited thickness for a given power. Finally, the deposition in nm/s is inferred, but it should be noted that this is a lower bound only as it depends on the angular range chosen, which always includes some buffer to ensure the line-of-sight is fully broken at the start and end.

Target	Power (W)	Voltage (V)	Current (mA)	Angular range (deg)	Mask slot width (mm)	Rate (nm×rpm/W)	Rate (nm/s) (lower bound)
Nb	90	253	356	40	24	0.0429	0.58
Nb	60	236	254	40	24	0.0429	0.39
Cr	30	260	115	30	6.8	0.0110	0.07
Pt	30	315	95	30	6.8	0.0206	0.12
Cu	30	297	101	30	6.8	0.0237	0.14
Fe	30	292	103	30	6.8	0.0140	0.08
Co	30	290	103	30	6.8	0.0210	0.13
Py	30	292	103	30	6.8	0.0150	0.09

3.1.3 Thickness calibration

In order to calibrate the growth rate of each metal, a film of thickness in the order of tens of nanometres is grown on a substrate with a line drawn on with a marker pen. This provides a simple means of lift-off patterning, since the residue from the pen can be removed with acetone, along with the metal deposited on it. The step height from the exposed substrate to the film can then be found with tapping mode atomic force microscopy. This allows calculation of actual film thicknesses grown on that deposition run, to the nearest nanometre. This calibrated rate can then be used for subsequent depositions.

3.2 Device fabrication

A nanopillar is a device geometry which defines a perpendicular-to-plane current path through a multilayer, by removing material to constrain the current. To obtain such a structure from an unpatterned multilayer, it is necessary to first use an optical lithography and etching process to create a narrow 4 µm track. Then, focused-ion beam (FIB) milling is used to create the nanopillar.

The mask used for optical lithography (designed by a previous group member) includes a 4 µm track, along which are a total of 7 junctions, with connections to contact pads for subsequent wire bonding. Experimentation with photoresist, spin speed, exposure time and development time resulted in the development of a satisfactory and reproducible process, summarized as follows:

- dip the sample in acetone before spraying with isopropanol from an airbrush, then dry with a nitrogen jet from the airbrush;
- spin AZ 4533 positive photoresist at 8000 rpm for 30 s to coat the sample;
- bake the sample on a hotplate at 115 °C for 30 s;
- using a square mask, expose the edges of the photoresist (the edge bead) to UV light for 60 s;
- submerge the sample in a solution of one part AZ 351B developer to two parts distilled water for 60 s, transfer to distilled water to stop the development, then dry with the airbrush;
- using the pattern mask, expose the remaining photoresist to UV light for 7 s;
- develop in the same solution for 30 s.

A thick resist is used because of the thickness of the multilayer (usually around 600 nm in this thesis), which needs to be protected in the subsequent milling step. The times are indicative; with careful observation during development it is possible to avoid under- or over-development, and under-developed resist can simply be developed for additional time.

A schematic of the mask used to define the track and contact pads is shown in Fig. 3.2 (a) and (b). After the photolithography step, the resist on top of the multilayer is only present in the grey regions in the figure. The next step is to mill away the multilayer film in the exposed regions, leaving film underneath the resist intact. This is achieved with an Ar ion miller. The milling parameters used for this work are as follows: Ar flow rate 1.43 sccm, discharge voltage 40 V, beam voltage 700 V, accelerator voltage 100 V. The cathode filament current was varied in order to maintain the beam current at 20 mA during milling. Milling through a typical multilayer film in this work (of which the bulk is 600 nm Nb) takes around 30 minutes under these conditions. Sufficient milling can be confirmed by visual appearance; the SiO_2 substrate surface layer

is initially violet, and runs through yellow and blue as it is thinned. If the film is over-milled, grey Si appears, and is a slightly different colour to Nb. A multimeter can be used to verify semiconducting rather than metallic resistance.

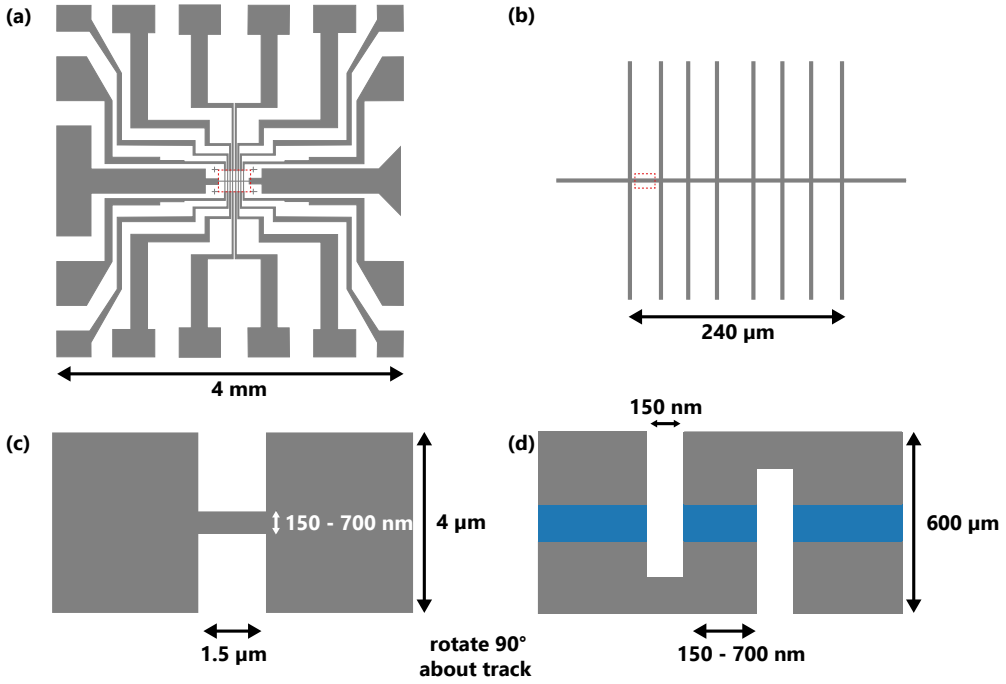


FIGURE 3.2: Schematic of the photolithography and FIB fabrication route: (a) shows the positive mask used for photolithography, with 18 contact pads; (b) a close-up of the red dashed box in (a), showing the central track region with spaces for 7 devices to be fabricated; (c) close-up of the track region in the red dashed box in (b), showing rectangular regions milled away by FIB in the initial track-thinning step; (d) a view after rotating about the track by 90° and milling the two slots from the side by FIB, to define the finished nanopillar.

A Zeiss Crossbeam 540 with both scanning electron microscope (SEM) and focused ion beam (FIB) functionality was used in this work. In the FIB, a Ga liquid metal source is ionized by an electric field. The ions generated are then accelerated to 30 kV and focused by electromagnetic lenses. When the beam encounters the sample surface, it can cause atoms to be ejected (as ions or neutral atoms), with the rate of milling being dependent on the beam current. Several detectors are available in the Crossbeam, but usually images were formed by secondary electron detection from an Everhart-Thornley detector.

The FIB nanopatterning process is performed in three stages. A custom-made stub with a 45° face is used to mount the sample (Fig. 3.3); this is necessary to allow the appropriate angular range between the sample surface and FIB beam for milling from both above and from the side of the track. Fig. 3.3 shows Position 1 (FIB beam perpendicular to the sample surface) and Position 2 (FIB beam almost parallel to the sample surface), which will be referred to in the following description. The angle between the electron beam and the ion beam is fixed at 54° in the Crossbeam. The accelerating voltage is 30 kV in all three stages.

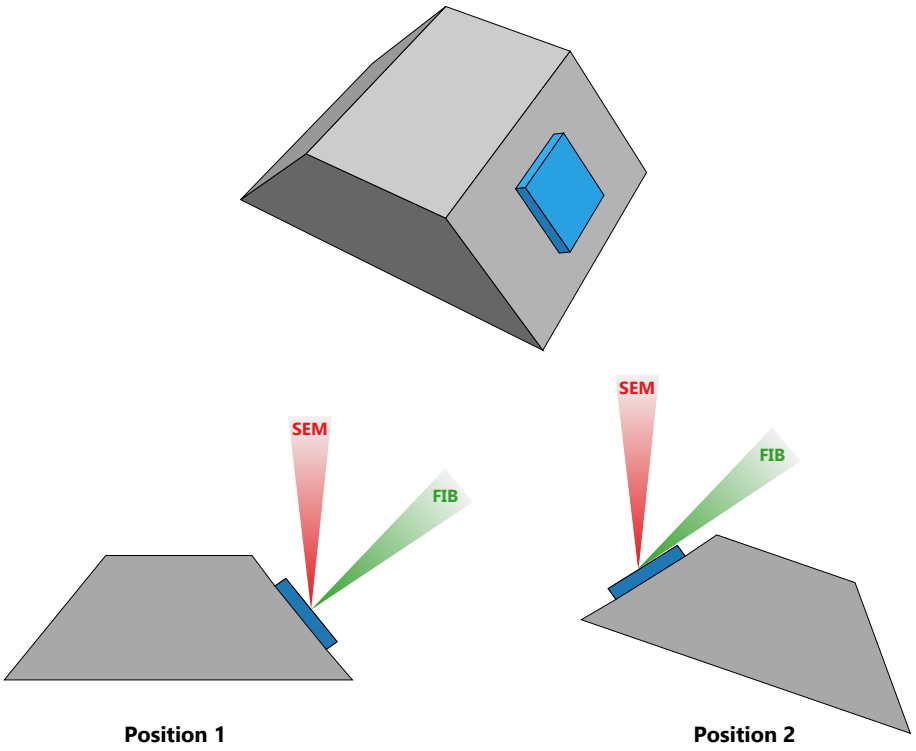


FIGURE 3.3: Top: Illustration of the 45° stub used to mount the 5 mm × 5 mm chip (shown in blue) during FIB nanopatterning. Bottom: The two positions relative to the SEM (red) and FIB (green) beams used during nanopatterning. Position 1 is used during the bulk track thinning and edge polishing steps, and Position 2 is used during the milling of the side slots.

Stage I, bulk track thinning. Starting with the 4 µm track, rectangular patterns are milled in Position 1 to achieve a thinner track of approximately 550 nm (chosen to result in a 400 µm track after Stage II). The beam current is 100 pA. The milling procedure is to raster the beam across the whole rectangular region repeatedly until the required dose is reached, which takes about 100 seconds for each rectangle of approximate size 1.5 µm by 2.5 µm, to a dose of 2.0 nC/µm^2. This dose was sufficient to mill through the total thickness of around 600 nm generally deposited in this thesis, although this can be verified in-situ by observing the disappearance of the granular film structure in the secondary electron signal and the accompanied sudden fall in intensity. The raster direction is chosen to end at the track, such that the ejected material is largely directed away from it.

Stage II, edge polishing. Still in Position 1, the walls of the thinned track region are milled further at a smaller current of 10 pA. This step ensures that all the sides of the finished nanopillar have been milled at the same small current, designed to limit Ga ion damage and implantation and to achieve a small spot size to make the walls more vertical. A rectangle of 200 nm is set with roughly half of this width overlapping the track, i.e. the edge being cleaned is in the centre of this rectangle. The dose used is 0.4 nC/µm^2. This step takes around 20 seconds per edge, and usually results in about

75 nm of material being removed from each wall, reducing the final device dimension by 150 nm. The nanopillars in this work varied from widths of 150-600 nm; greater thicknesses make it difficult to perform Stage III successfully. This step uses a line-by-line milling procedure, administering the full dose to each line of pixels before moving to the next, as is typically done in a polishing procedure.

Stage III, side slot milling. The sample is moved to Position 2 by rotating the stub 180° about the vertical axis and tipping it back until the sample surface is in the line-of-sight of the FIB beam. The final angle between the sample normal and the FIB beam is around 87°; 90° is impractical as visibility of the FIB image is lost. A beam current of 10 pA is used at the same accelerating voltage to remove two slots of width around 150 nm, defining a nanopillar of roughly rectangular cross-section. A dose of around 1.0 nC/µm^2 is sufficient to mill through a 400 nm thick track, and the moment of breakthrough is easily identified by the large increase in the electron signal. This step takes about 15 s. The result is sketched in Fig. 3.2 (d). The slots must be positioned so as to clip the central barrier layer; this is easy when the barrier is sufficiently thick and has a sufficient contrast with Nb (e.g. materials with a high atomic number such as Pt). In many cases however, the barrier is not visible in the secondary electron image. Here, the position of barrier in the film is determined as being at a height of half of the thickness of the entire multilayer (which is easily discernible from the substrate). The slots are then positioned clipping this height, with an additional buffer of around 50 nm. The nanopillars in this work varied from side lengths of 150-700 nm. Fig. 3.4 shows both a schematic and a secondary-electron image of a finished nanopillar.

While this technique has advantages over multiple lithography and deposition steps as described by Blamire et al. [60], there are some limitations of the technique. The beam shape results in a tapering of the sidewalls rather than the idealized perfectly orthogonal ones sketched. This means the analysis of $I_c(H)$ assuming rectangular junctions will not match the measured form precisely, although the incorporation of ferromagnetic layers does far more to modify the form of $I_c(H)$. Another issue is that Ga ions may implant to a certain depth, and cause damage to the crystal structure. The typical stopping distances for Ga ions at 30 kV have been extensively studied, and are found to be around 11.3 nm in Nb, 10 nm in Fe and 6.8 nm in Pt [61]. These distances are much smaller than the dimensions of the devices. Furthermore, the beam direction is always perpendicular to the nanopillar, so the scenario of head-on stopping distances described is the very worst-case one as regards this fabrication process. The milling procedures described above are designed to mitigate these effects, but their presence is borne in mind when interpreting the data.

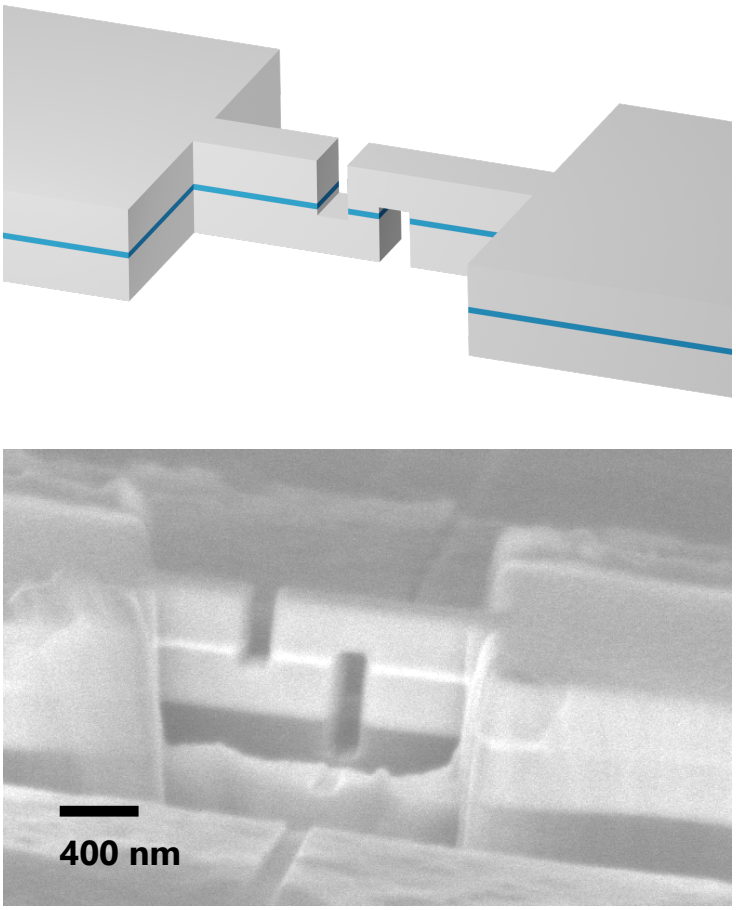


FIGURE 3.4: Top: Schematic 3D model of a finished nanopillar device. The blue layer is the barrier layer, while the thick grey layers are the superconducting Nb electrodes. Bottom: Secondary electron image from the SEM showing a finished nanopillar device. Here, the barrier layer (46 nm Pt) is clearly visible as a bright line in the middle of the deposited film. The mid-grey regions above and below are Nb, while the dark region underneath the lower Nb is the substrate.

3.3 Film microstructure and interface roughness

Sputter deposition gives rise to a polycrystalline microstructure, which can vary from small crystallites separated by voids, through to relatively large, equiaxed grains. The determining factor is the mobility of the deposited atoms on the surface of the growing film. Higher growth temperatures and/or slower deposition rates increase the mobility of the atoms, which leads to denser films and larger grain sizes. In the experiments of this thesis, the substrates are at room temperature (or below due to imperfect isolation of the substrate table from the liquid nitrogen jacket) and deposition rates are relatively high at several Å/s as seen in Table 3.1. This means we expect a small grain size.

Unfortunately, systematic structural characterizations of the films in this thesis

were not carried out due to time constraints, however some aspects of the microstructure can be ascertained. The mean free path for Cooper pairs in the interlayer Nb of Nb/Cr/Fe/Nb/Fe/Cr/Nb devices was found to be about 11 nm in Chapter 6. The probable cause of the scattering is the presence of grain boundaries, and so we expect the grain size to be on this order of magnitude. This tells us that the devices in this work should be considered to be in the diffusive limit.

Interface roughness is another important issue to address, as it has wide ranging consequences for many aspects of the physical phenomena being studied in this work. Atomic-force microscopy scans were performed on some 300 nm Nb films, the thickness chosen for the Nb electrodes of the devices in this thesis. It was found that the films had a roughness of around 2-3 nm, although it should be noted that Nb oxidizes in atmospheric conditions and so this is not wholly representative of conditions at the interface in a multilayer device. Some of the sputtered layers in these experiments have thicknesses of 1 nm or less, meaning they might start to become discontinuous. This is perhaps most relevant to the thin Cr layers employed, although here the roughness may in fact confer an advantage in promoting a spin glass state, as described in Subsection 1.2.2. The micromagnetic state of magnetic thin films will in general be affected by roughness in a complex way. One well-known phenomenon is that of so-called 'orange-peel' coupling between ferromagnetic layers with a thin spacer between them. The stray fields from the asperities of the rough magnetic layers will interact, which is known to increase their coercivities. This may well be relevant for the devices of this thesis which have multiple ferromagnetic layers. As described in Section 1.4, roughness is expected to decrease perpendicular magnetic anisotropy. The data in Chapter 7 show that good PMA is attained in Nb/Pt(2)/Co(1.5)/Pt(2)/Nb devices, evidenced by an out-of-plane easy axis. This indicates that the roughness is not detrimental in this case at least.

The potential effects of microstructure and interfacial roughness will be discussed where they might affect the interpretation of the data. Since many of the experiments involve varying one of the layer thicknesses in a device structure, interfacial effects are usually readily distinguished from the parameters of interest.

3.4 Low-temperature transport measurements

After fabrication, devices are mounted into 20-pin chip carriers with GE varnish, and bonded to the contact pads with 20 µm Al wire. The chip carrier is then inserted into a proprietary Cryogenic Ltd 3483 LCC20 resistivity probe for use with the same company's Mini Cryogen-Free system. The system is illustrated schematically in Fig. 3.5.

This system features a closed-circuit gas flow (hence the term 'cryogen-free') and a 1 T superconducting magnet. The system has an integrated variable temperature insert (VTI) in which the sample probe is inserted. Liquid He-4 passes through a two-stage cryo-cooler to reach 4.2 K before condensing in the helium pot. A needle valve

is used to control the flow of liquid He-4 into the VTI, with the associated volume expansion causes further cooling down to the base temperature of 1.6 K. If a higher temperature than the base temperature is desired, the VTI heat exchanger then allows the helium to be heated to a set temperature, as used in warming $R(T)$ curves in this work. The gas then flows past the sample and is pumped by a room-temperature pump to return to a helium dump, completing the closed cycle. The VTI heat exchanger temperature and the sample temperature are measured by Lake Shore Cryotronics Cernox thin-film resistance cryogenic temperature sensors. The sample probe additionally has a small heater for fine temperature control. A Lake Shore 350 temperature controller is used for PID control of the temperatures of the sample, the VTI heat exchanger, and the helium pot. The distance between the sample and the Cernox temperature sensor is about 10 mm and thermal lag is noticeable; for example when loading the probe while measuring resistance, an apparent T_c around 1 K higher than that of bulk Nb is observed. For this reason, temperature dependence in this thesis is usually measured through gradual ramping of the temperature with the VTI heat exchanger at a rate of about 2 K/h.

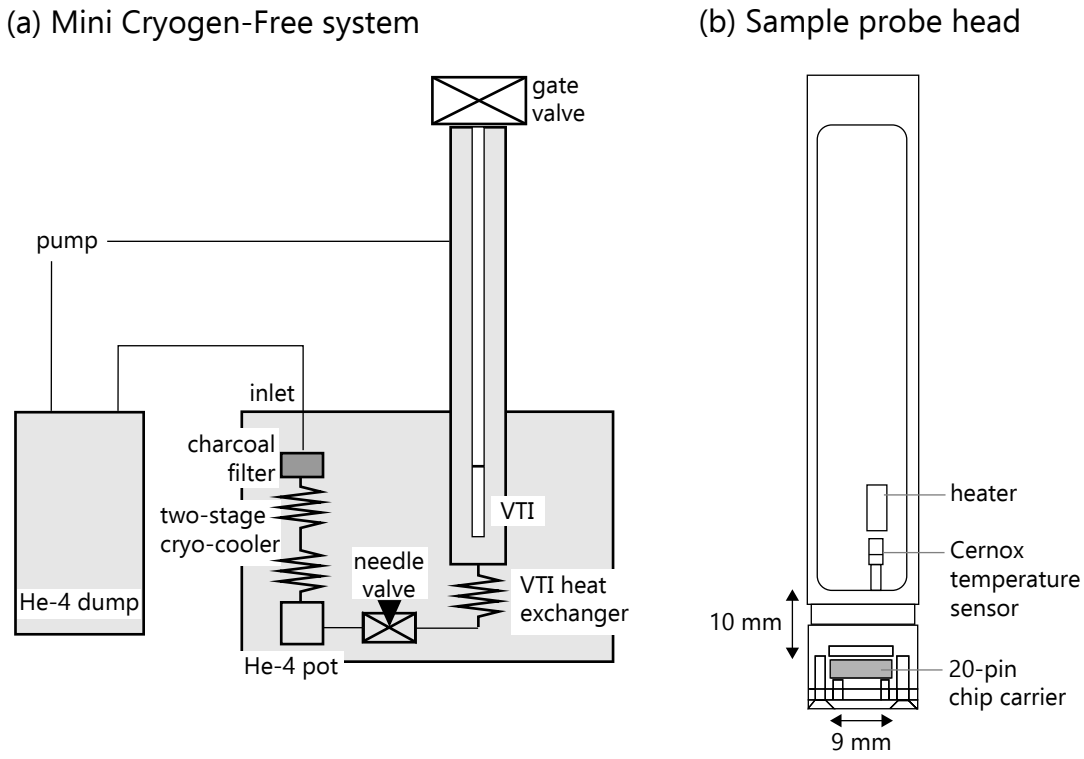


FIGURE 3.5: Schematic illustration of the low-temperature transport measurement system used; Cryogenic Ltd's Mini Cryogen-Free system: (a) a simplified schematic drawing of the closed He-4 circuit used to achieve a base temperature of 1.6 K; (b) a schematic drawing of the sample probe head, with approximate dimensions. The sample is mounted to the 20-pin chip carrier and sits directly in the circulating gas.

Transport measurements on the nanopillar devices are taken in a four-point configuration, using a Keithley Model 6221 current source paired with a Keithley Model

2182A nanovoltmeter. The differential conductance mode is used, whereby an alternating current $\mathrm{d}I$ is superposed onto a linear sweep of the current from $-I_{\mathrm{max}}$ to $+I_{\mathrm{max}}$. $\mathrm{d}I$ was usually 10 µA in this thesis. The nanovoltmeter measures the voltage at each step and calculates $\mathrm{d}V$. In this way, the differential resistance $\mathrm{d}V/\mathrm{d}I$ is measured as a function of I, in addition to the $V(I)$ characteristic. An example of a $\mathrm{d}V/\mathrm{d}I$ plot and a $V(I)$ plot obtained in this way are shown in Fig. 3.6. Further details can be found in Keithley's white papers [62] [63]. Note that the Josephson junction measurements are current-biased, hence the reference to $V(I)$ characteristics, but the convention is chosen in this thesis that voltage is on the horizontal axis.

In order to define I_{c} and R_{N}, I fit an overdamped RSJ model (see Subsection 2.2.2) to the $V(I)$ characteristics. Capacitance is small for metallic junctions, hence I refer here to a RSJ model rather than a RCSJ model. The fitted equation is:

$$I_{\pm} = \pm\sqrt{I_{\mathrm{c}}^2 + (V/R_{\mathrm{N}})^2} \tag{3.1}$$

and an example of the fit is shown in the lower panel of Fig. 3.6. Graphically, $\pm I_{\mathrm{c}}$ are the intercepts of the curve with zero voltage, while R_{N} is the slope of $V(I)$ for $I \gg I_{\mathrm{c}}$.

The $I_{\mathrm{c}}R_{\mathrm{N}}$ product (also known as the characteristic voltage) is an important quantity in this thesis, since it is independent of junction size, under the assumption that the current density in the junction is uniform. The current density J_{c} will also be reported often, as well as the area-resistance product AR_{N}, which is an important indicator of accurate fabrication as it should be constant for a given device structure.

Measurements of critical current as a function of applied field $I_{\mathrm{c}}(H)$ are performed using the superconducting magnet in the Mini Cryogen Free system, with the field applied in the plane of the junction, in the direction perpendicular to the track from which the nanopillars are cut. This orientation is defined as $\phi = 0°$, and where the orientation with respect to the field differs from this, it will be noted in the text. The geometry described is shown in Fig. 3.7. Differential resistance measurements are performed at each applied field in the same manner as described above, before stepping the field and taking the next sweep. I_{c} is then extracted at each field by fitting an RSJ curve as described. A typical Fraunhofer pattern obtained in this way is shown in Fig. 3.8.

The Fraunhofer-like $I_{\mathrm{c}}(H)$ dependence of Josephson junctions is a good indicator of successful device fabrication. The periodicity of the oscillation can be compared to that expected from the device dimensions. For junctions containing ferromagnetic layers, I_{c} is dependent not only on the applied field but also on the internal flux from the ferromagnet. This has the effect of shifting the maximum I_{c} away from zero field. Furthermore, the reversal of the magnetization during the sweep may result in a sudden discontinuity in the Fraunhofer pattern, or for a more gradual reversal over a range of applied field, a shrinking of the periodicity. Field sweeps in this thesis are always performed starting from ± 200 mT unless otherwise stated. This is significantly higher than the coercivity of all the ferromagnetic materials used, although it should

be noted that the micromagnetic behaviour of the nanopillars has not been measured or modelled.

Where field sweeps are performed, $I_c R_N$ is defined by the maximum I_c value (which is not necessarily found at zero applied field) and the median R_N value (R_N does not vary significantly during such sweeps).

Temperature sweeps are performed in an equivalent fashion to field sweeps. A PID-controlled heater steps the temperature from base temperature upwards in increments and a differential resistance sweep is performed at each temperature. This yields both $I_c(T)$ (via RSJ-fitting as usual) and accurate $R(T)$ curves, obtained by taking the value of differential resistance at zero current at each temperature.

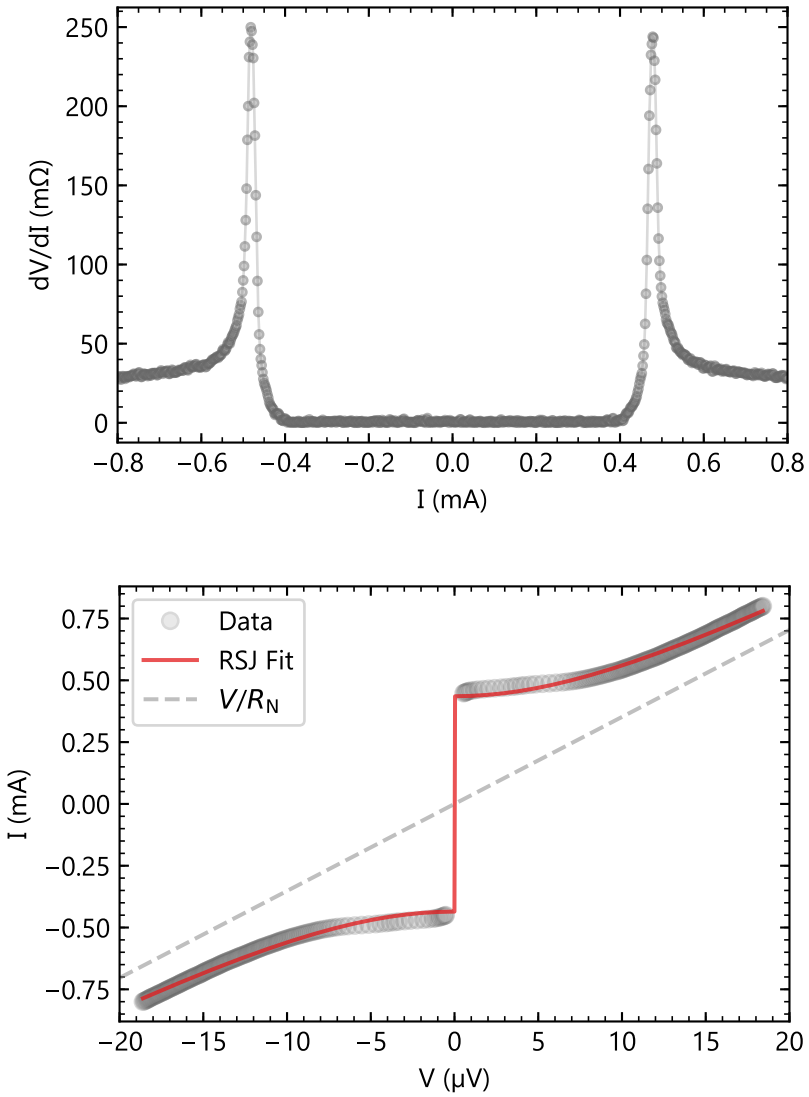


FIGURE 3.6: Top: Differential resistance measured for a current sweep on a Nb/Cr(1)/Fe(2)/Nb(5)/Fe(2)/Cr(1) device at 1.6 K. Bottom: $V(I)$ from the same measurement at 1.6 K, with an RSJ model for an overdamped Josephson junction fitted (red). The data points around zero voltage (where $I < I_c$) have been removed since the RSJ function only applies for $I > I_c$. The grey dashed line has slope $1/R_N$ and represents the ohmic behaviour which the $V(I)$ characteristic should asymptotically approach.

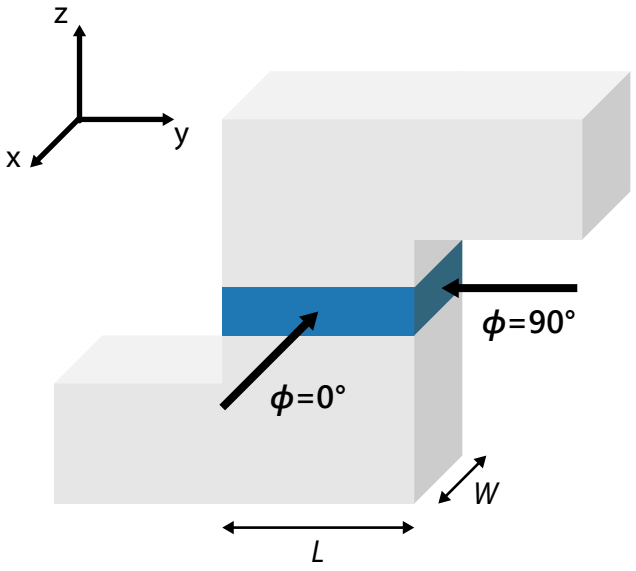


FIGURE 3.7: Definition of geometry and coordinate ϕ, giving the angle between the pillar and the applied magnetic field. When $\phi = 0°$, the applied field is perpendicular to the track from which the pillars are milled (the default measurement angle in this thesis) and when $\phi = 90°$, the applied field is parallel to the track. L is defined as the pillar dimension between the slot cuts, and W is the dimension fixed by the initial track thinning and edge polishing.

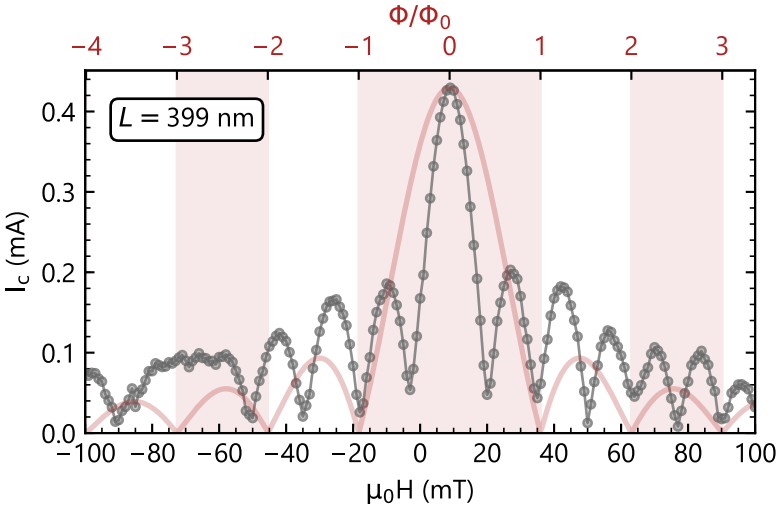


FIGURE 3.8: $I_c(H)$ dependence (after saturation at -200 mT and sweeping in the positive direction) of a Nb/Cr(1)/Fe(2)/Nb(5)/Fe(2)/Cr(1) device at 1.6 K (grey points). A model Fraunhofer pattern based on the junction length L (red line); the London penetration depth is taken to be 90 nm. The model Fraunhofer has been re-centred on the peak of $I_c(H)$, which is shifted from zero applied field due to the internal flux from the magnetic layers. Shaded regions are an aid to visualize the expected periodicity.

3.5 Magnetic characterization

3.5.1 Vibrating sample magnetometry

The magnetization of a sample can be measured by the voltage it generates when moved relative to a pick-up coil, due to Faraday's law of induction. This is the principle used in vibrating sample magnetometry (VSM). A schematic of the Princeton MicroMag VSM system used in this work is shown in Fig. 3.9. Samples undergo vibration at a frequency of up to 75 Hz in the vicinity of two pairs of pickup coils. A lock-in amplifier allows the signal due to the sample magnetization to be isolated, since the voltage generated in the coils will oscillate with the same frequency as that of the vertical drive. Sample magnetization can be measured in a VSM with the application of a magnetic field using the electromagnet, such that $M(H)$ loops can be measured.

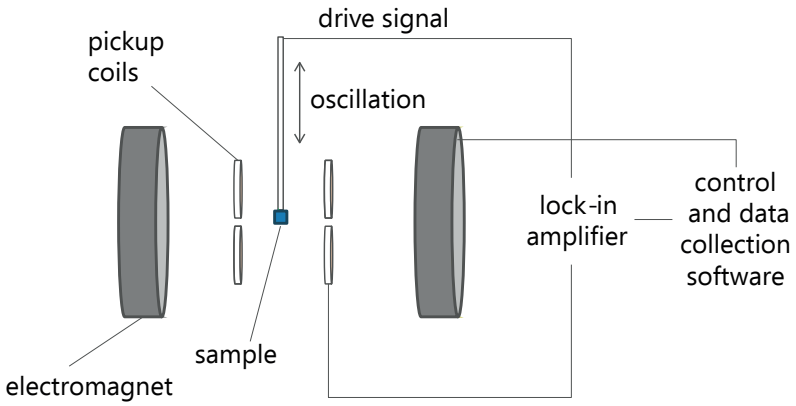


FIGURE 3.9: Schematic diagram of the VSM system used.

Chapter 4

Effect of area and aspect ratio on ferromagnetic nanopillar Josephson junctions

This thesis is largely concerned with the behaviour of ferromagnetic nanopillar Josephson junctions fabricated via a focused ion beam technique from a thin-film multilayer. In order to draw reliable conclusions in later chapters, it is of fundamental importance to understand the effects of varying the nanopillar dimensions on the critical currents and normal state resistances of the devices. The effects of varying the aspect ratio will also be studied, since this may be expected to influence the magnetic behaviour via shape anisotropy.

Nb/Py/Nb junctions are chosen as a simple model system to study, where the low magnetocrystalline anisotropy of Py allows for the dominance of shape anisotropy effects.

The device fabrication and measurements in this chapter are the sole work of the author.

4.1 Nb/Py/Nb junctions

Fig. 4.1 defines the nanopillar dimensions and field measurement angles referred to in this chapter.

Firstly, I study the effect of varying area on devices with a 3.4 nm Py barrier. It can be seen that both $I_c R_N$ and J_c decrease with increasing area (Fig. 4.2), whereas these quantities would be expected to be constant for ideal Josephson junctions with a spatially uniform current distribution. Aspect ratio is controlled in these devices to be approximately one; the tolerance of FIB fabrication means that an aspect ratio range of 0.9-1.1 is achieved in practice. Additionally, the junctions will deviate from the rectangular shape assumed due to the beam shape and milling procedure (see Methods, Subsection 3.2).

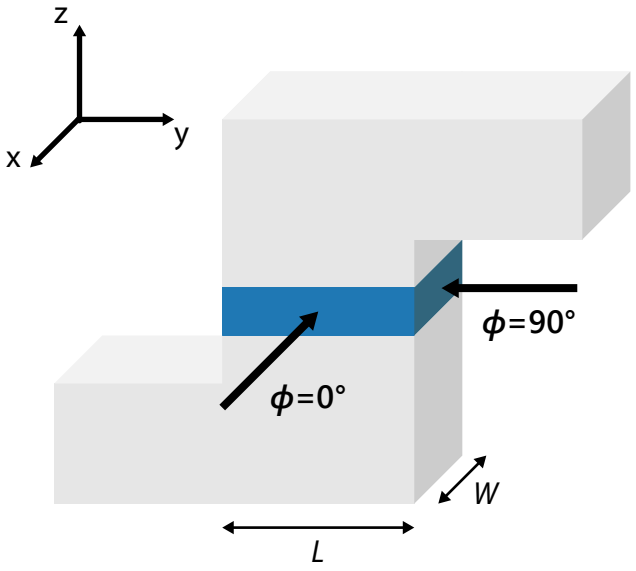


FIGURE 4.1: Definition of geometry and coordinate ϕ, giving the angle between the pillar and the applied magnetic field. When $\phi = 0°$, the applied field is perpendicular to the track from which the pillars are milled (the default measurement angle in this thesis) and when $\phi = 90°$, the applied field is parallel to the track. L is defined as the pillar dimension between the slot cuts, and W is the dimension fixed by the initial track thinning and edge polishing (see Subsection 3.2).

Next, I study the variation of I_cR_N and J_c (maximized as a function of field, i.e. measured at the central peak of the Fraunhofer pattern, which may be at non-zero applied field) with aspect ratio L/W (Fig. 4.3). These measurements indicate that I_cR_N and J_c are independent of aspect ratio in the range studied.

AR_N gives a good indication of junction quality and should be constant for a junction of a given barrier thickness, depending only upon the resistances of the interfaces and barrier. Fig. 4.4 shows that AR_N is independent of both area and aspect ratio. This means R_N is inversely proportional to area as may be expected.

I now try to understand why I_cR_N and J_c decrease with increasing area. Plotting the critical current I_c against area would give a straight line through the origin if the current were spatially uniform. Instead, we observe that the critical current increases non-linearly with area, curving downward below a direct proportionality (Fig. 4.5). This explains the decrease of I_cR_N and J_c at higher areas.

I consider whether the junctions may be considered to be in the short-junction limit; i.e. $L \ll \lambda_J$ (see Subsection 2.2.4). L/λ_J varies from around 0.5 for the smallest area device to around 1.0 for the largest area device. Self-field effects may lead to the current adopting a non-uniform spatial dependence in the junction, more concentrated towards the nanopillar walls. However, in Chapter 5 of Barone and Paternò [40] it seems this variation in current is negligible for $L/\lambda_J = 1$. Self-field effects should not therefore play a significant role, nonetheless, the data are consistent with a non-uniform current distribution.

A crude model may be adopted whereby the current is assumed to be carried only by the edges of the nanopillar, and assume that the maximum critical current would be proportional to the perimeter $2(L + W)$. This leads to a surprisingly good fit to the data shown in Fig. 4.5.

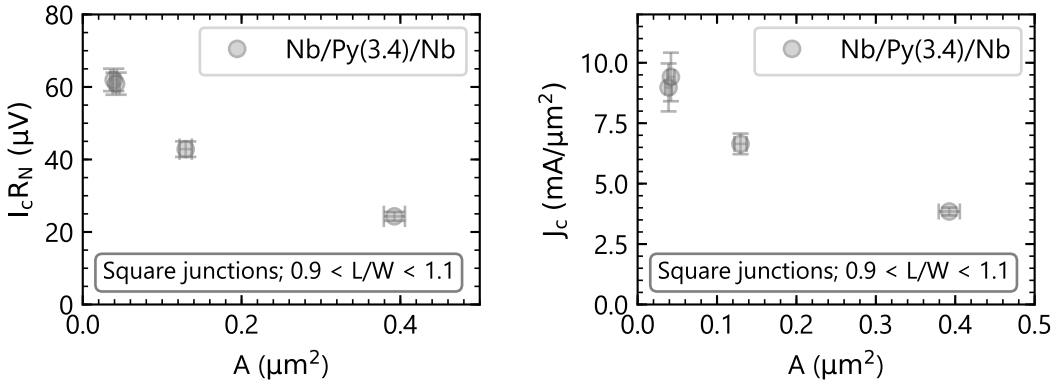


FIGURE 4.2: Left: I_cR_N variation with device area at 1.6 K. Right: J_c variation with device area at 1.6 K.

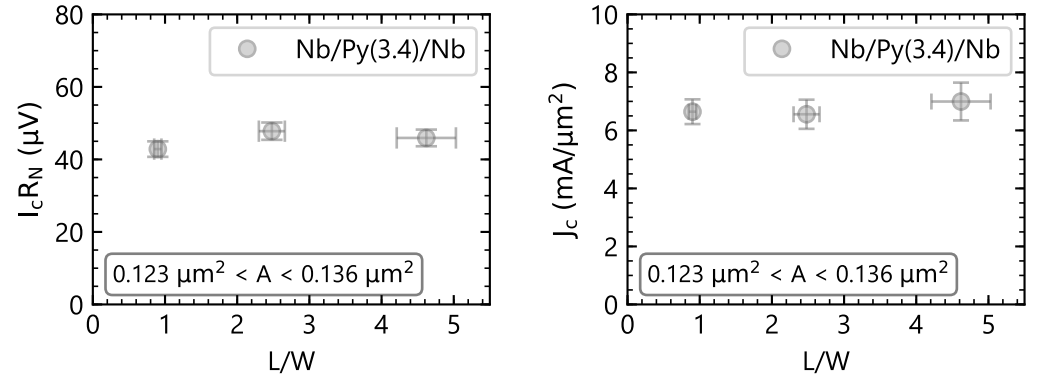


FIGURE 4.3: Left: I_cR_N variation with device aspect ratio at 1.6 K. Right: J_c variation with device aspect ratio at 1.6 K.

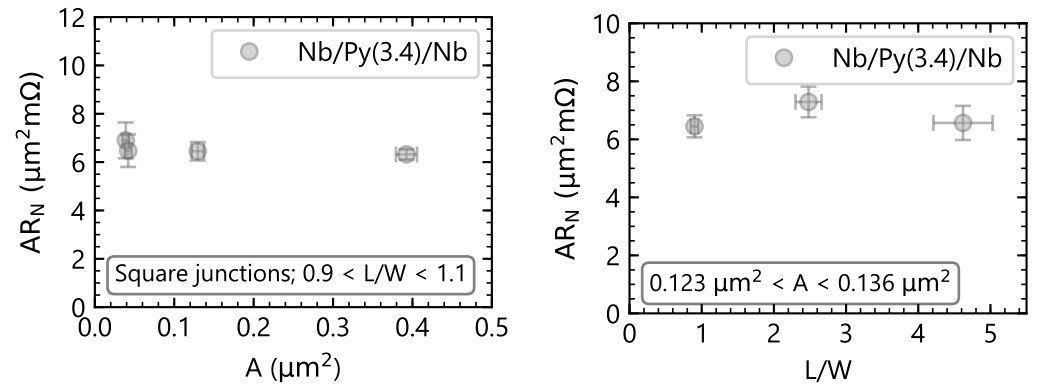


FIGURE 4.4: Left: AR_N variation with device area at 1.6 K. Right: AR_N variation with device aspect ratio at 1.6 K.

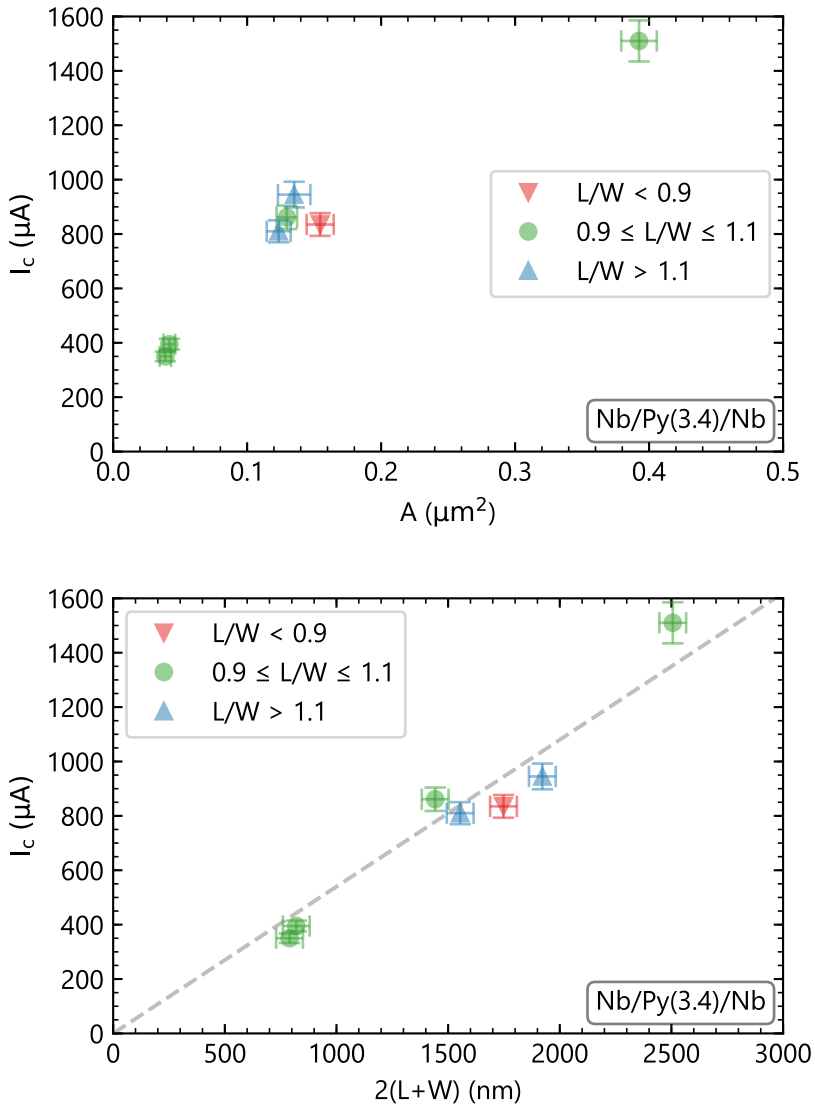


FIGURE 4.5: Top: I_c variation with device area at 1.6 K. Bottom: I_c variation with device perimeter at 1.6 K.

The data suggest that the current is non-uniform in the junction and confined to the nanopillar edges. According to Barone and Paternò [40], such a current profile would modify the Fraunhofer patterns by increasing the subsidiary lobe amplitudes. The Fraunhofer patterns (Fig. 4.6) show increased subsidiary lobe heights in general for these devices, but this appears to be independent of the junction length L. Therefore it is not entirely clear if this is the cause of the variation in I_cR_N and J_c.

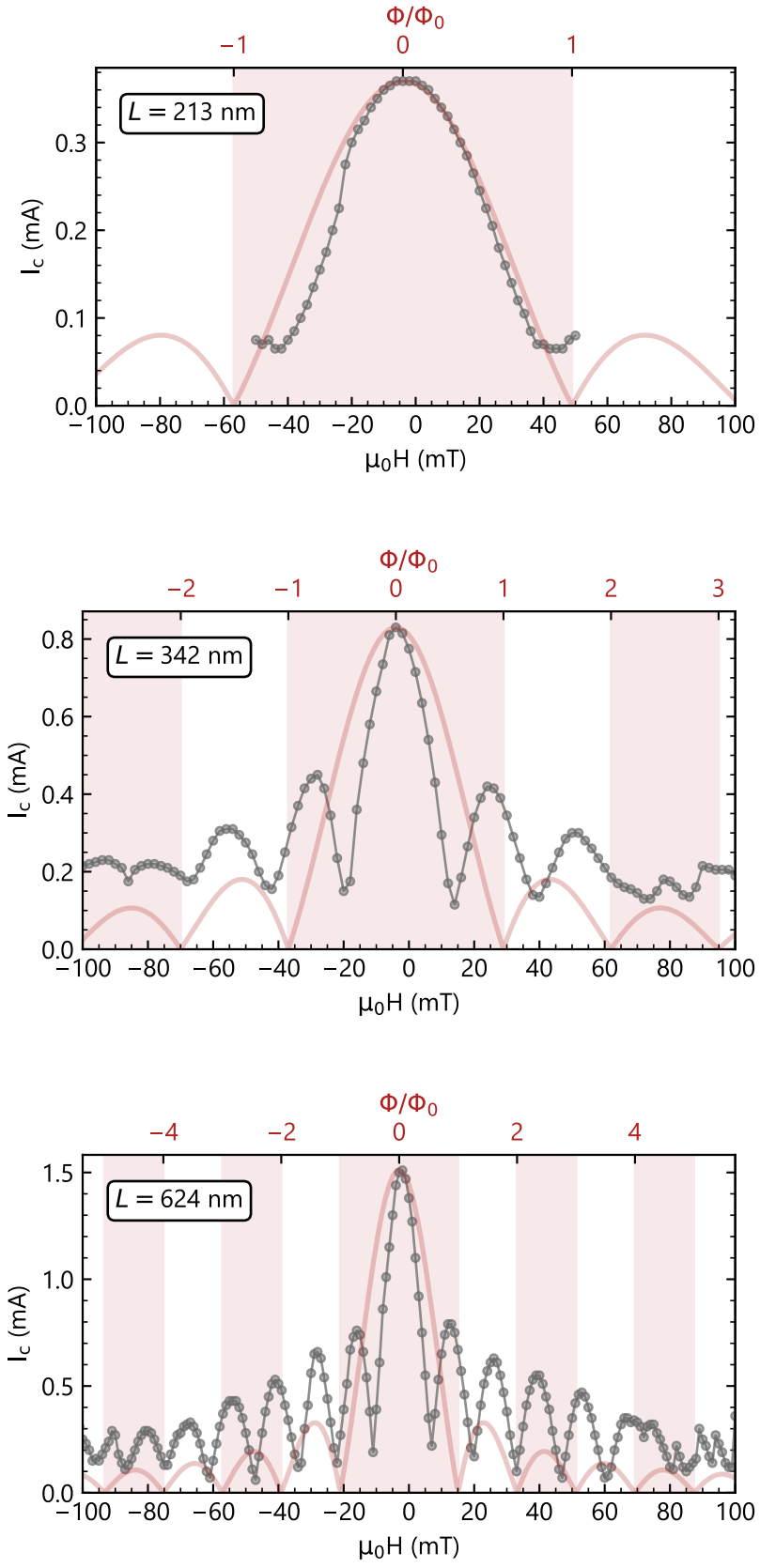


FIGURE 4.6: Fraunhofer patterns for Nb/Py(3.4)/Nb devices at 1.6 K. The red shaded regions, top axis and red model pattern are calculated from the device dimension L and show the expected periodicity. The grey points are the measured data, with the grey line joining subsequent measurements as a guide to the eye.

Thicker devices (5.3 nm Py) show a similar lack of dependence on aspect ratio - the differences in I_cR_N and J_c observed across the aspect ratio studied are not statistically significant (Fig. 4.7). Critical currents are very small at this thickness of Py, approaching the limit of detection in our apparatus.

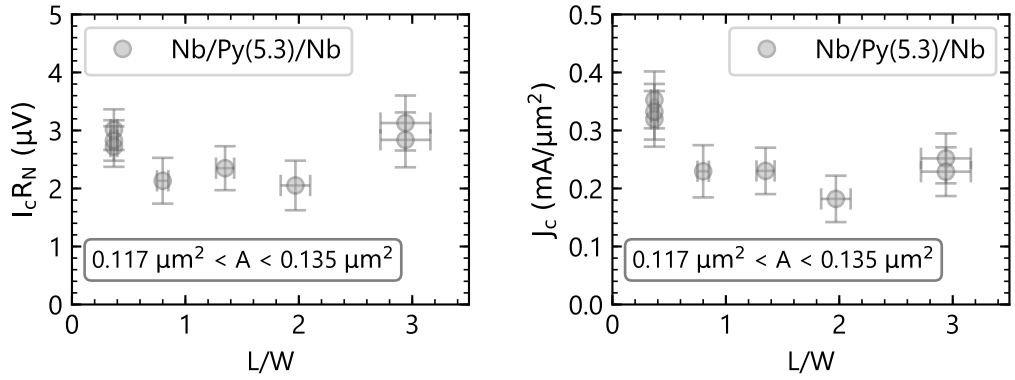


FIGURE 4.7: Nb/Py(5.3)/Nb devices of varying aspect ratio. Left: I_cR_N variation with device aspect ratio at 1.6 K. Right: J_c variation with device aspect ratio at 1.6 K.

I now study the effect of varying the angle ϕ of the magnetic field in the plane of the barrier. It should be noted that the device fabrication may lead to an asymmetry in ϕ even for a square junction, due to the possible influence of the 4 micron track from which the devices are subtractively fabricated. The track may influence the nanopillar through the stray field of its magnetic layer, and through the Meissner magnetic screening of its superconducting layers (see Methods for a discussion of the nanopillar and track geometry). I define $\phi = 0°$ when the magnetic field is applied perpendicular to the track (the default in this thesis) and $\phi = 90°$ when the field is applied parallel to the track.

Fig. 4.8 shows the behaviour of I_cR_N against aspect ratio again, but this time with additional measurements at $\phi = 45°$ and $\phi = 90°$. It can be observed that the difference in the maximum I_cR_N achieved is independent of angle, within error. From this I conclude that (1) pillar shape (and the associated shape anisotropy) is not important in determining the maximum I_cR_N, (2) effects due to the track discussed above are negligible.

Table 4.1 shows the hysteresis shift ΔH for angles of $\phi = 0°$ and $\phi = 90°$ for selected devices with a high aspect ratio. Most often, a higher value of ΔH is observed when the field is applied such that the flux penetrates the short edge of the pillar. In Fig. 4.9, the dependence of the hysteresis shift ΔH on aspect ratio is plotted for all the devices. It can be seen that in general, higher aspect ratios (where the field penetrates the longer side of the junction) lead to smaller values of ΔH. This can be explained by the shape anisotropy of the ferromagnetic layer tending to favour magnetization parallel to its long edge. Reversing the magnetization along the long edge of the nanopillar requires a higher coercive field, leading to a greater hysteresis shift. Reversing the magnetization parallel to the short edge requires less field. In terms of shape anisotropy this is

the hard axis, and so when the field is returned to zero, the tendency of the magnetization will be to return parallel to its long edge, lessening the hysteresis.

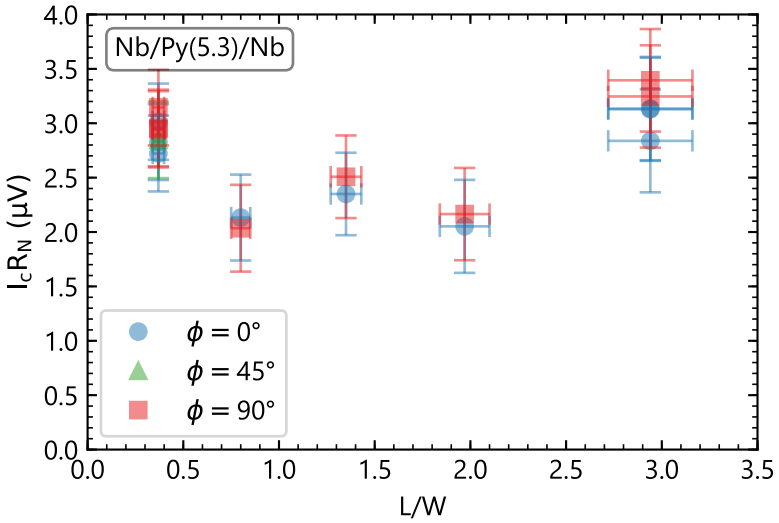


FIGURE 4.8: I_cR_N against aspect ratio at different angles ϕ with respect to the applied field at 1.6 K.

TABLE 4.1: Hysteresis shift ΔH measured along perpendicular axes for selected devices with high aspect ratios at 1.6 K. $\phi = 0°$ means that the effective junction length facing the applied magnetic field is L, whereas at $\phi = 90°$ it is W.

Device	L (nm)	W (nm)	$\Delta H_{\phi=0°}$ (mT)	$\Delta H_{\phi=90°}$ (mT)
Nb/Py(5.3)/Nb	212	575	12	8
Nb/Py(5.3)/Nb	621	211	2	18
Nb/Py(3.4)/Nb	554	223	2	14

4.2 Conclusions

This chapter has provided a brief insight into the effect of varying the device dimensions on a simple ferromagnetic nanopillar Josephson junction. I conclude that varying the aspect ratio does not have an appreciable effect on the critical current density or I_cR_N product, however the junction area causes a monotonic decrease in both of these. The reason for this is that the critical current does not increase in proportion to the junction area. Self-field effects do not seem likely based on calculations of the Josephson penetration depth; significant drops in the critical current are only observed when the device dimension is several times this depth. However, a crude model assuming that all the current is carried in the nanopillar walls does match the data well. The data alone are insufficient to explain the size dependence definitively, but size

effects are taken into consideration when analysing the rest of the device data in this thesis.

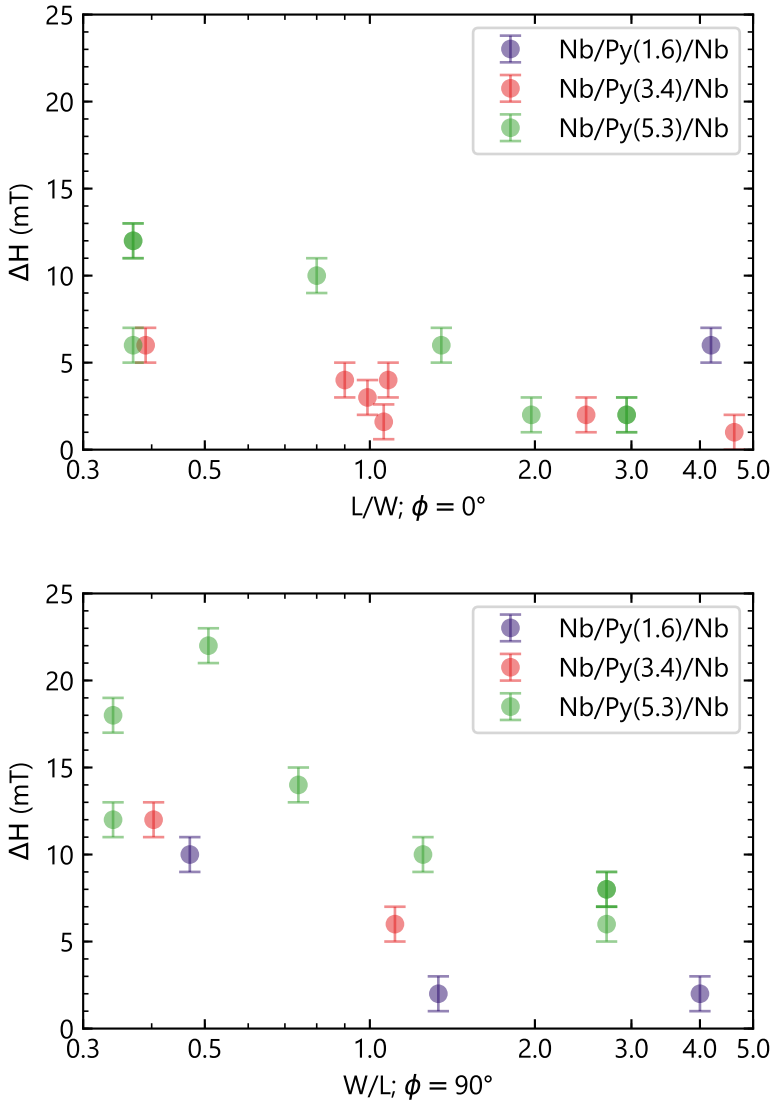


FIGURE 4.9: ΔH variation with aspect ratio at 1.6 K. Top: measurements performed with the applied field at $\phi = 0°$. Bottom: measurements performed with the applied field at $\phi = 90°$. To compare like-with-like, the top plot uses L/W for the aspect ratio, whereas the bottom uses W/L, hence a high value of aspect ratio always means that the long side of the junction is penetrated by the applied magnetic flux.

Chapter 5

Josephson junctions with spin glass interfaces

Cr/Fe interfaces host a spin glass at low temperature (see Subsection 1.2.2). This presents a potentially advantageous type of magnetic inhomogeneity for generating long-ranged triplet supercurrents; the relatively small number of interfaces needed to obtain magnetic inhomogeneity (compared with magnetic multilayers) allows for better resistance matching.

Cr/Fe spin glass spin mixers have been studied by Robinson et al. [21], where a long-range triplet (LRT) supercurrent was measured through a layer of Fe much thicker than the singlet decay length. Firstly, we seek to corroborate the generation of the LRT with an analogue of a S/F′/F/F′/S device with spin glass interfaces as F′.

The fabrication and measurement of the devices in this chapter were performed jointly by Dr Sachio Komori and the author.

5.1 Nb/Cr/Fe/Cr/Nb junctions

We deposited a series of Nb/Cr(1)/Fe/Cr(1)/Nb films with Fe thicknesses of between 3 nm and 12 nm, along with a limited number of Nb/Fe/Nb control devices with Fe thicknesses of 6 nm and 9 nm. The $V(I)$ characteristics at 4.2 K for the Fe devices were found to be ohmic, while the Nb/Cr(1)/Fe(9)/Cr(1)/Nb device showed a relatively large critical current (see Fig. 5.1). This follows what was observed by Robinson et al. [21], and gives a potential indication that a LRT component has been generated.

We now wish to compare our devices against suitable control experiments. The singlet critical current in ferromagnetic Josephson junctions oscillates in amplitude (via 0-π oscillations) and decays rapidly with increasing ferromagnetic thickness over a few nanometres, as discussed in Subsection 2.3.1. The decay of the singlet supercurrent in similarly fabricated Nb/Fe/Nb devices has been studied by Piano et al. [64], with the I_cR_N data being reproduced in Fig. 5.2. This study limited the range of thicknesses to below 5.5 nm in order to sample the 0-π oscillations sufficiently. Our own control Nb/Fe/Nb junctions have thicker Fe than those of Piano et al. and showed no supercurrent, appearing as zeroes on the plot. We recognize that the small number

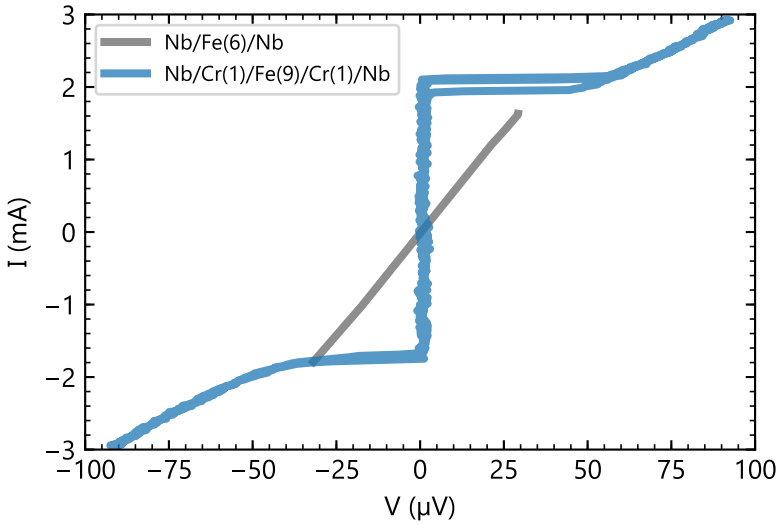


FIGURE 5.1: $V(I)$ characteristics measured at 1.6 K for a Nb/Fe(6)/Nb device (no spin-mixer interface) and a Nb/Cr(1)/Fe(9)/Cr(1)/Nb device with spin-mixers.

of control devices limits their usefulness; these may coincide with zeroes in the oscillation by chance. However, this is fairly unlikely; the data of Piano et al. contain no zeroes. It should also be noted that Fe-only devices do not control for the role of Cr and its effect on singlet supercurrents.

Another control is provided in the form of Nb/Fe/Cr(2)/Fe/Nb devices from Robinson et al. [65]. This allows us to see both the effects of adding 2 nm Cr and two Cr/Fe interfaces. In that study, the Fe layers were found to couple parallel magnetically at this thickness, and so the data provide a good control for the single Fe layers in our new data. In this structure, the Cr/Fe interfaces are separated from the Nb electrodes, and so they do not act as spin-mixers. Cr causes strong spin scattering, and so may be expected to break both singlet and triplet pairs. Additionally, the Cr/Fe interfaces cause further scattering. The result is that the measured supercurrents are severely diminished by the addition of Cr. This is seen in the lower values of $I_c R_N$ for Nb/Fe/Cr(2)/Fe/Nb devices than for Nb/Fe/Nb devices.

For further comparison, Nb/Cr(0.8)/Fe/Nb(40)/Pt(4.4)/Nb devices from Chapter 8 of this thesis are also plotted. LRT generation was anticipated in these devices, however as described in Chapter 8 I believe the measurements here to result from singlet supercurrents alone. Therefore the device structure may be considered as effectively Nb/Cr/Fe/Nb; the Pt layer is simply a second Josephson junction in series with a far higher critical current, and so does not significantly impact the behaviour. These devices therefore consist of a single spin-mixer, with no complement on the other side of the ferromagnet; in this case a LRT is not expected, and indeed we see a rapid decay with Fe thickness on a length scale of around 0.5 nm, indicative of a singlet supercurrent.

Now turning to the Nb/Cr/Fe/Cr/Nb devices with spin-mixers, both the Robinson et al. data and our new data are plotted on Fig. 5.2. Our Nb/Cr(1)/Fe/Cr(1)/Nb

data show that in these devices the amplitude of I_cR_N recovers up to that seen in Nb/Fe/Nb devices at the very least, despite the additional Cr. The Robinson et al. Nb/Cr(2.5)/Fe/Cr(2.5)/Nb data show I_cR_N exceeding the same group's Nb/Fe/Cr(2)/Fe/Nb devices, despite a total Cr thickness of 5 nm. This recovery of the amplitude of I_cR_N is another hint of LRT generation; rather than the Cooper pairs scattering, they are converted into spin-aligned triplet pairs which continue through the Fe layer.

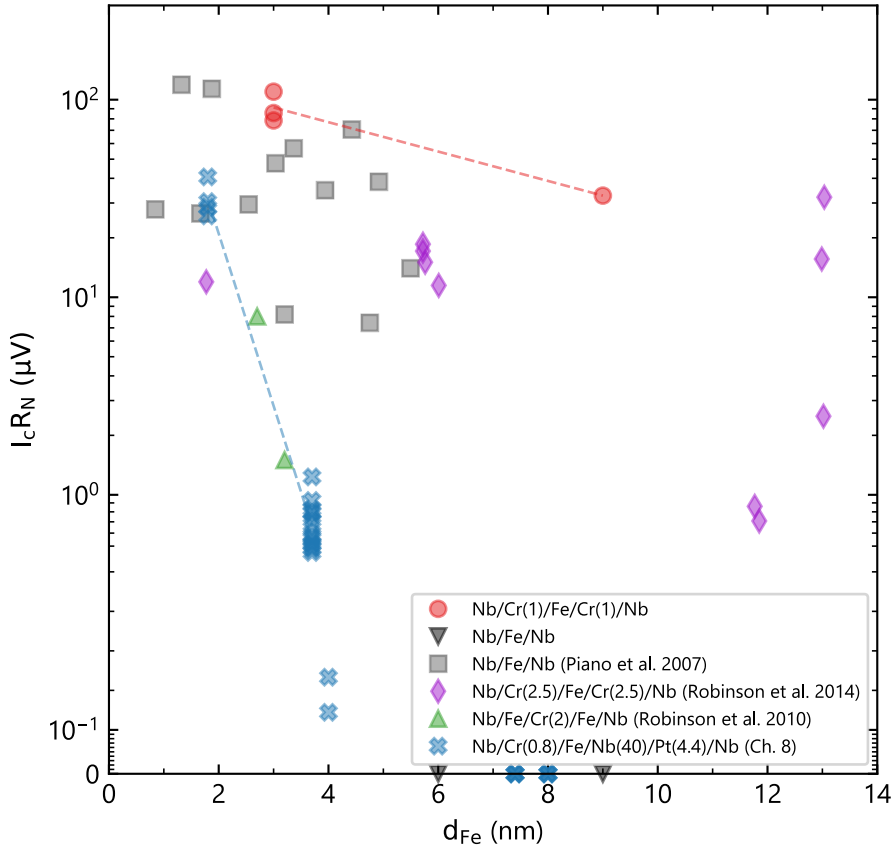


FIGURE 5.2: Decay of I_cR_N with thickness of ferromagnet d_{Fe} at 4.2 K in Nb/Cr(1)/Fe/Cr(1)/Nb devices (our data, red circles). Comparative data are provided for Nb/Fe/Nb from Piano et al. [64] up to 5.5 nm Fe (grey squares) and from our own data for 6 nm Fe and 9 nm Fe (black triangles). Data for Nb/Cr(2.5)/Fe/Cr(2.5)/Nb from the original Robinson et al. study [21] are included (purple diamonds), as well as Nb/Fe/Cr(2)/Fe/Nb devices from an earlier work by this group [65], where the Fe thickness plotted here is the total thickness of the two Fe layers. Data from Nb/Cr(0.8)/Fe/Nb(40)/Pt(4.4)/Nb devices from Chapter 8 of this thesis are provided for further comparison. The dashed lines are exponential fits to the data for Nb/Cr(1)/Fe/Cr(1)/Nb (red dashed line) and Nb/Cr(0.8)/Fe/Nb(40)/Pt(4.4)/Nb (blue dashed line), corresponding to decay lengths of 6 nm and 0.5 nm respectively. Note that the vertical scale changes from log to linear below 0.1 μV to allow for the plotting of zeroes in the critical current.

The decay length of the supercurrent in the ferromagnet is often used to provide evidence for LRT generation, as it is significantly greater for spin-aligned triplets compared with singlets, as described in 2.3.1. The Robinson et al. Nb/Cr(2.5)/Fe/Cr(2.5)/Nb data show considerable scatter and no decay length was reported in that work. Indeed, a horizontal line could describe the data well. It may be hypothesized that at lower thicknesses both singlet and triplet components are present, and that the proportion of supercurrent constituted by triplet correlations is increasing as the Fe thickness increases and the singlet component decays.

Our present Nb/Cr/Fe/Cr/Nb data is scant, but some interesting observations can be made. At 3 nm Fe, our data points lie around the highest of the Fe-only I_cR_N values. Together with the point at 9 nm, we can extract a first estimate of the decay length of around 6 nm, which is not strikingly different from that of the Piano et al. Nb/Fe/Nb data, but is much higher than that in the Nb/Fe/Cr(2)/Fe/Nb and Nb/Cr(0.8)/Fe/Nb(40)/Pt(4.4)/Nb devices for which it is < 1 nm.

Fig. 5.3 shows our Nb/Cr/Fe/Cr/Nb device measurements at 1.7 K. At this temperature, a supercurrent is seen also at 12 nm Fe, providing us with another data point from which to estimate the decay length in Fe. Table 5.1 summarizes the results of extracting the decay length from fitting an exponential decay to the I_cR_N and J_c at 1.7 K and 4.2 K (note that this results in asymmetrical one-sigma errors). The decay envelope for singlets reported by Piano et al. is 3.8 nm at 4.2 K. In our data, the triplet decay length at 4.2 K is slightly larger than 3.8 nm, but similar to this value at 1.7 K, where there are more data points. However, it is possible that the 3.8 nm decay constant reported by Piano et al. for singlets is an overestimate. Elsewhere it is reported to be around 1 nm [21]. Another worthwhile observation is that fitting a simple exponential decay to the Nb/Cr/Fe/Cr/Nb data is inaccurate for low d_{Fe} where the singlet contribution to the supercurrent remains significant. This will tend to decrease the estimate of $\xi_{Fe}^{triplet}$, the triplet decay length in Fe.

We recognize that the number of data points is far too few to make robust comparisons, but the differences in measured decay lengths, in particular against other devices incorporating Cr, are at least consistent with LRT generation in the devices with symmetric Cr/Fe spin-mixer interfaces. Our Nb/Cr(1)/Fe/Cr(1)/Nb devices show a decay length of around 5 nm where for asymmetric Nb/Cr(0.8)/Fe/Nb(40)/Pt(4.4)/Nb devices or Nb/Fe/Cr(2)/Fe/Nb devices with the spin-mixers separated from the electrodes, the decay length is an order of magnitude less. Furthermore, the measurement of supercurrents through 9 nm Fe at 4.2 K and 12 nm Fe at 1.6 K is unexpected for a purely singlet supercurrent in both our control devices and in the literature.

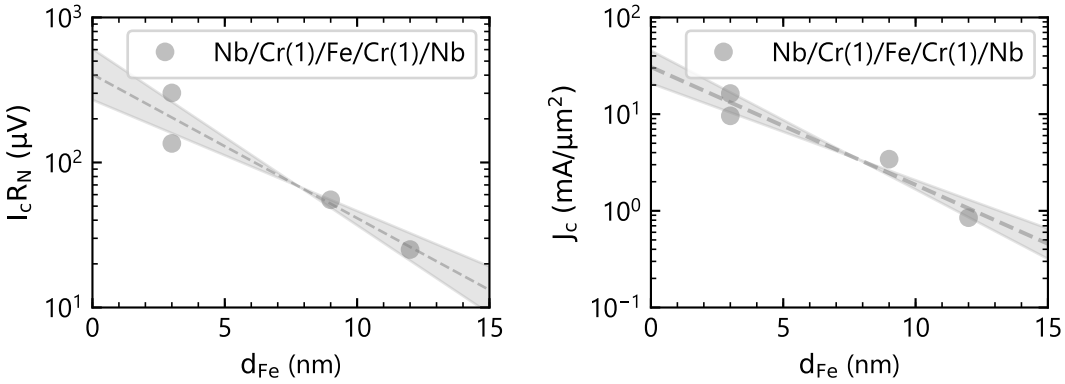


FIGURE 5.3: Left: Decay of I_cR_N with thickness of ferromagnet d_{Fe} at 1.7 K in Nb/Cr/Fe/Cr/Nb devices. At this temperature, supercurrent can be detected up to d_{Fe} = 12 nm. Right: Critical current density J_c for the same devices, showing a similar trend. In both plots, the errors on individual points are smaller than the markers.

TABLE 5.1: Summary of fitting to decay data to estimate the decay length of triplets in Fe.

T (K)	Decay fit	$\xi_{Fe}^{triplet}$ (nm)
1.7	I_cR_N	4 ± 1
	J_c	4 ± 1
4.2	I_cR_N	6^{+2}_{-1}
	J_c	7^{+4}_{-2}

For a model S/F′/F/F′/S Josephson junction, Houzet and Buzdin [51] found the triplet supercurrent to be given by $I_c = I_c(0) \sin\phi_1 \sin\phi_2$, maximized when ϕ_1 and ϕ_2 (angles between F and each F′ magnetizations) are $\pi/2$. In our case, the interface magnetizations may be considered as a spin glass with randomly magnetized clusters. The length scale of these clusters is around 1 nm [66]. Averaging over the possible values of ϕ_1 and ϕ_2 gives us a triplet Josephson current of $(2/\pi)^2 I_c(0)$ - i.e. we expect a conversion efficiency of around 40 per cent of the ideal case of the Houzet-Buzdin model.

We found our intended long-range devices had a success rate of around 15-20%. If we postulate that these are LRT-dominated devices, this could be due to the spin glass forming in some areas, while others have a more uniform magnetization. Additionally, we observed that working devices tend to be found adjacent to each other on the chip. This could indicate the relevance of some magnetic heterogeneity on this length scale between devices (around 30 μm).

The $I_c(H)$ dependence of each device was obtained to verify the expected Josephson junction behaviour. These show an approximate $|\mathrm{sinc}(\Phi)|$ dependence as expected, but exhibit an asymmetric shift in field (Fig. 5.4). This shift reverses direction upon reversal of the field sweep direction, and is due to the additional flux coupling the junction due to the magnetization of the Fe layer. We may define $\Delta H = \frac{1}{2}(H^+_{\mathrm{peak}} - H^-_{\mathrm{peak}})$, where H^+_{peak} (H^-_{peak}) is the applied field for which peak I_c is measured on the positive (negative) field sweep from saturation ($\pm 200\,\mathrm{mT}$), i.e. the applied field at which the internal flux is cancelled. ΔH is found to increase proportionally with d_{Fe} (plotted along with the unpatterned film magnetizations in 5.5), giving a good indication that the magnetic junctions are behaving as expected. The expected gradient of ΔH (d_{Fe}) can be determined from a simplified model. The additional flux due to a uniform magnetic layer of magnetization M is $\Phi_{\mathrm{M}} = dL\mu_0 M$. The plot should therefore be shifted by Φ_{M}/Φ_0 periods. Multiplying by the period $\Phi_0/d'L$ (where $d' = d + 2\lambda$) gives the expected ΔH as $\mu_0 M(d/(d+2\lambda))$ or for $d << 2\lambda$, $\Delta H = \mu_0 M d/2\lambda$. Therefore the slope should be given by $\mu_0 M/2\lambda = 4.3\,\mathrm{mT/nm}$ (using the volume magnetization determined above), whereas we find $0.55\,\mathrm{mT/nm}$, around 13% of the expected value. The discrepancy is unsurprising as the model does not account for magnetic dead layer, and assumes a perfectly uniform single ferromagnetic domain directed opposite to the applied field. In reality, some magnetization reversal may have begun before the cancellation field H_{peak} is reached.

Fig. 5.5 shows the areal magnetization of unpatterned Nb/Cr(1)/Fe/Cr(1)/Nb films. The slope of the fit against thickness gives the volume magnetization as $(619 \pm 2)\,\mathrm{emu/cm^3}$. This is low compared with the literature value of $1714\,\mathrm{emu/cm^3}$ for bulk Fe [67], but in the region of the $830\,\mathrm{emu/cm^3}$ measured by Robinson et al. [68], where it is attributed to film quality and interfacial effects. From the intercept, the dead layer thickness is found to be $(0.5 \pm 0.2)\,\mathrm{nm}$.

5.2 Conclusions

The primary aim of this chapter was to reproduce the results of Robinson et al. on generating long-ranged triplet correlations with Cr/Fe spin glass interfaces. The observation of Josephson supercurrents in the range of Fe thickness 9 nm - 12 nm along with the lack of a supercurrent in control Nb/Fe/Nb devices gives some indication that a LRT may be generated in these devices. Furthermore, data from devices with Cr not acting as a spin-mixer show a decay length of $< 1\,\mathrm{nm}$, where our Nb/Cr/Fe/Cr/Nb devices show a decay length of around 5 nm. However, the evidence for LRT generation here relies on very few devices and so caution must be exercised. A new control study of Nb/Fe/Nb or Nb/Fe/Cr/Fe/Nb devices across the range of Fe thicknesses up to 15 nm would be required, as well as many more measurements of Nb/Cr/Fe/Cr/Nb devices in order to characterize the behaviour across this range and obtain more accurate estimates for the decay lengths. Only then could LRT generation in such spin glass devices be definitively claimed.

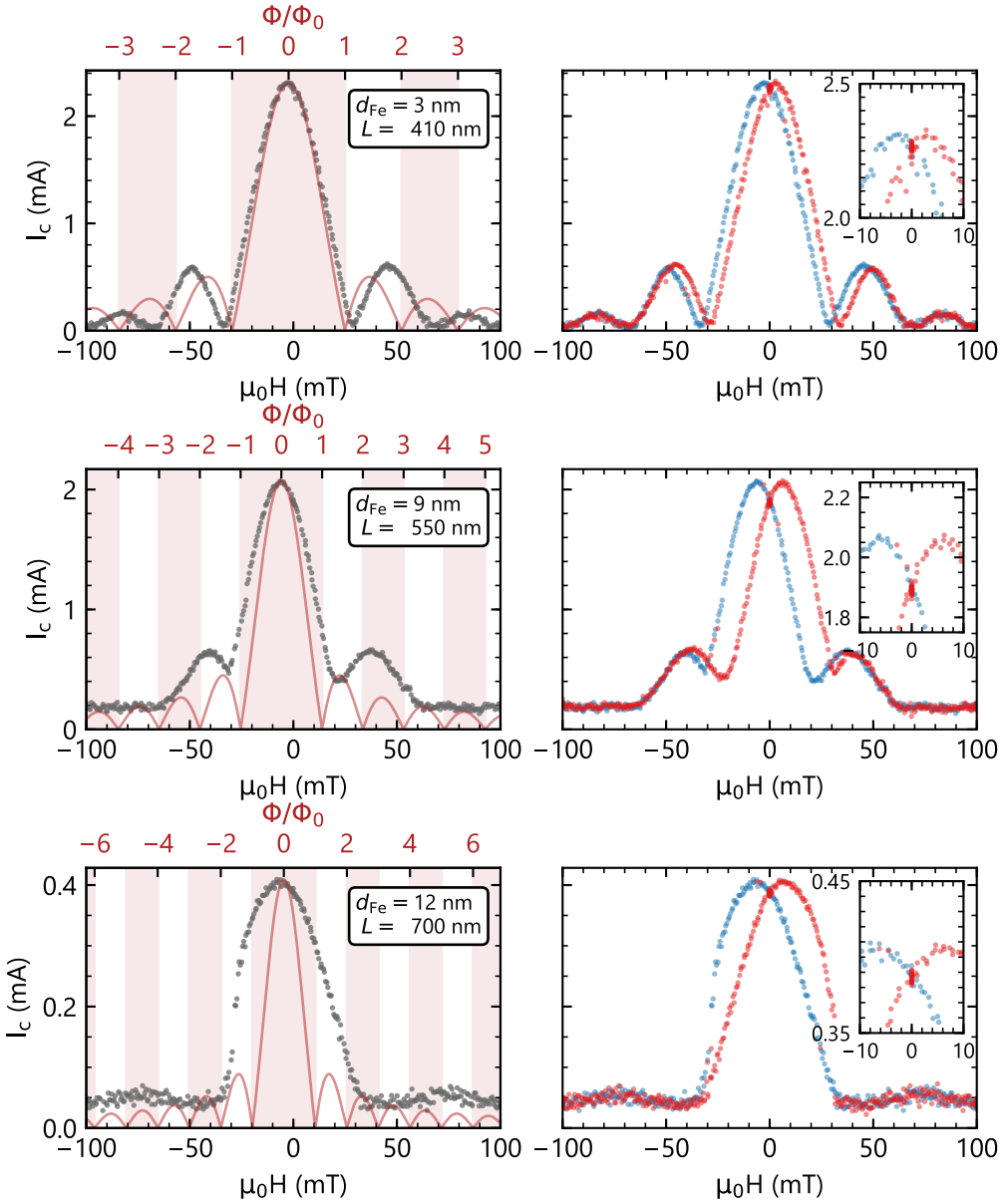


FIGURE 5.4: Left: $I_c(H)$ dependence of the devices from saturation at 200 mT applied field, swept in the negative direction (grey points) at 1.7 K. A model Fraunhofer pattern based on the junction length L (red line); the London penetration depth is taken to be 90 nm. The model Fraunhofer has been re-centred on the peak of $I_c(H)$, which is shifted from zero applied field due to magnetic hysteresis. Shaded regions are an aid to visualize the expected periodicity. Right: $I_c(H)$ dependence for positive (red) and negative (blue) sweep directions from saturation. The vertical scale is shared between each pair of plots.

While the Cr/Fe system creates magnetic inhomogeneity without the need for multiple magnetic layers and therefore allows for devices with relatively few interfaces, the spin glass is very difficult to control and characterize. Despite attempts to, this study did not elucidate the conditions required to optimize the spin glass and LRT generation, and found that the yield of devices showing supercurrent with greater than 6 nm Fe was small, at around 20%. The Cr/Fe interface as a spin-mixer is perhaps less convenient than it appears at first glance and presents many experimental challenges in controlling and optimizing the micromagnetic structure. Initial optimism

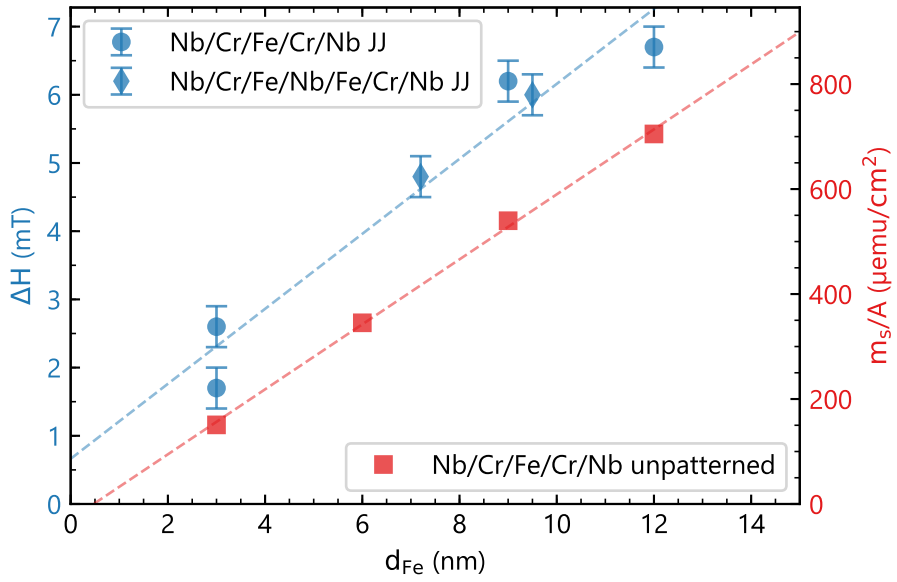


FIGURE 5.5: Right axis: Saturation magnetization per unit area as a function of Fe thickness (red squares) for unpatterned Nb/Cr(1)/Fe(d_{Fe})/Cr(1)/Nb films at 293 K, showing a linear dependence (slope (619 ± 2) emu/cm^3) with a small magnetic dead layer of (0.5 ± 0.2) nm. Left axis: Absolute offset of peak $I_c(H)$ from zero field when sweeping field from saturation ΔH at 1.6 K (blue circles). Data for two Nb/Cr(1)/Fe/Nb/Fe/Cr(1)/Nb devices are also included in this plot, falling on the same trend (blue diamonds). The thicknesses of the Fe/Nb/Fe layers in these two devices were Fe(2.4)/Nb(4.8)/Fe(4.8) and Fe(2.0)/Nb(4.0)/Fe(7.5), and they are plotted such that d_{Fe} is the sum of the two Fe layer thicknesses.

about the Cr/Fe devices here however meant that several of the other experiments in this thesis incorporated this spin-mixer interface; where they appear, the data will be interrogated in view of the doubts raised in this chapter.

Chapter 6

Josephson junctions with spin glass interfaces and a superconducting interlayer

The aim of this chapter is to extend previous work on the generation of long-ranged triplet (LRT) supercurrents to explore their propagation outside the typical S/F′/F/F′/S device structures. Here we study the as yet little-investigated behaviour of spin triplet supercurrents encountering another superconductor with a conventional s-wave density of states. A major question to address is the decay constant of the triplet supercurrent inside a conventional superconductor. It is not known whether the triplet is supported by the s-wave superconductor or rapidly decays. Understanding this behaviour is fundamental to the development of devices for superconducting spintronics, as we need to know how spin information can be propagated through intermediary superconducting regions.

The experiments of this chapter rely on Cr/Fe spin-mixer interfaces. As discussed in the previous chapter, some doubts remain over whether we are generating significant triplet correlations in these devices and doing so reliably. The results in this chapter will be discussed under the hypothesis that only singlets are present, and in addition, under the speculative hypothesis that LRT correlations are present. We will see that some of the results are difficult to explain assuming purely singlet supercurrents, providing a rationale to invoke our speculative LRT-based explanation.

The fabrication and measurement of the devices in this chapter were performed jointly by Dr Sachio Komori and the author.

6.1 Nb/Cr/Fe/Nb/Fe/Cr/Nb junctions

Having seen some possible indications of long-ranged triplet generation with Cr/Fe interfaces, we now turn to the question of the propagation of the LRT in an intermediary singlet superconductor. It is not known whether an intermediary superconductor increases, diminishes or has no effect on a triplet supercurrent. To answer this question, a superconducting interlayer of 4 nm-40 nm will be inserted into the structure,

where the total Fe thickness is > 7.2 nm; at these thicknesses we do not observe a supercurrent in our control Nb/Fe/Nb devices. However, we first perform a control experiment for lower Fe thicknesses where the singlet component remains the dominant contribution. Comparisons with the devices with thicker Fe will then be made to discern whether there are significant differences, possibly attributable to LRT correlations.

6.1.1 Singlet-dominated interlayer junctions

The device structure for our control experiment is:

Nb/Cr(1)/Fe(2)/Nb'($d_{Nb'}$)/Fe(2)/Cr(1)/Nb;

with a total Fe thickness of 4 nm, the singlet component of supercurrent is supported across the whole junction. The I_cR_N product is plotted as a function of Nb thickness in Fig. 6.1. There seem to be two regimes of behaviour in the thickness range investigated. From 5 nm to 20 nm, there is a decrease in I_cR_N. Nb thin films must reach a critical thickness to support superconductivity since the order parameter is suppressed near the boundary of a superconductor (see Subsection 2.1.3). The I_cR_N decay may therefore be explained by the greater thickness of normal state Nb presenting an increased barrier thickness to the supercurrent. Then, at a critical thickness, the interlayer supports superconductivity and so I_cR_N rises again. It rises above the value at 5 nm, because now there is no normal state Nb component to the barrier. While no devices with $d_{Nb'} > 40$ nm were produced, we expect the value of I_cR_N to plateau as the Nb thickness exceeds the coherence length, and the behaviour approaches two independent S/F/S junctions in series (c.f. later double-barrier experiments in Chapters 7 and 8).

$AR_N(d_{Nb'})$ provides further verification of consistent device fabrication, and allows us to extract a value for the resistivity of the normal state Nb at 1.6 K as $(8 \pm 1)\,\mu\Omega\,\mathrm{cm}$ (Fig. 6.2). Note that R_N is extracted for current bias $I > I_c$, hence there is no discontinuity at the thickness where the Nb interlayer achieves superconductivity. Current-biasing the junction into the normal state necessarily drives the interlayer into the normal state.

The effective electron mean free path l is therefore $l = m_e v_F / N_d \rho_{Nb} e^2 = (11 \pm 2)\,\mathrm{nm}$, where m_e is the electron rest mass, $v_F = 1.37 \times 10^6\,\mathrm{m\,s^{-1}}$ is the Fermi velocity, $N_d = 5.57 \times 10^{28}\,\mathrm{m^{-3}}$ is the number density of conduction electrons in Nb, and e is the elementary charge. Hence, the electron diffusivity is given as $D_N = v_F l/3 = (5.1 \pm 0.7) \times 10^{-3}\,\mathrm{m^2\,s^{-1}}$. This gives $\xi_{Nb}^{singlet} = (\hbar D_N / 2\pi k_B T)^{1/2} = (62 \pm 4)\,\mathrm{nm}$.

It is difficult to define with certainty the thickness at which the interlayer becomes superconducting. However, we might expect the decay constant in I_cR_N with increasing $d_{Nb'}$ to match the diffusive-limit coherence length calculated above from the device resistivities. Fig. 6.1 shows this decay as a dashed line; it agrees with the data within error. Fitting an exponential decay to the points between 5 nm and 20 nm yields a decay constant of $(50 \pm 20)\,\mathrm{nm}$. The data points are therefore consistent with the interlayer being in the normal state in this thickness range.

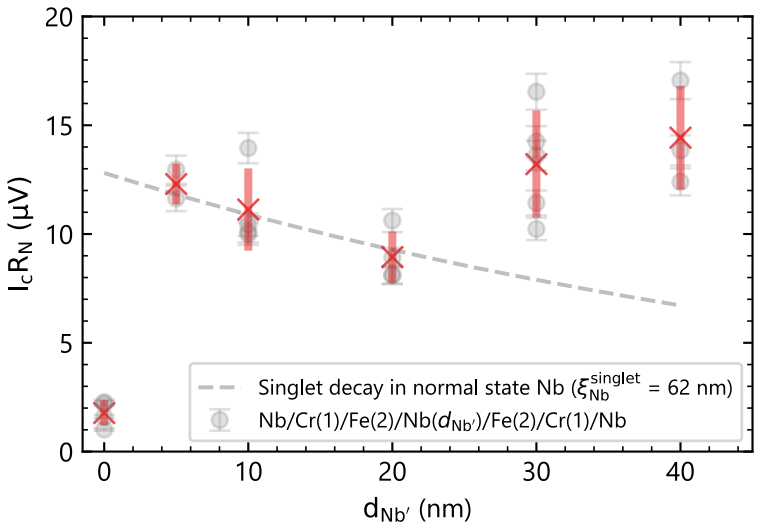


FIGURE 6.1: I_cR_N dependence on the Nb interlayer thickness for Nb/Cr(1)/Fe(2)/Nb′($d_{Nb'}$)/Fe(2)/Cr(1)/Nb devices at 1.6 K. Grey circles are measurements from individual devices. Red crosses and red vertical bars indicate the mean value of I_cR_N and the sample standard deviation respectively at each interlayer thickness. The dashed line is an exponential decay assuming a diffusive decay length for singlets of 62 nm calculated from the device resistivities, showing good agreement with the data for interlayers of thickness 5 nm, 10 nm and 20 nm where the interlayer is assumed to be in the normal state.

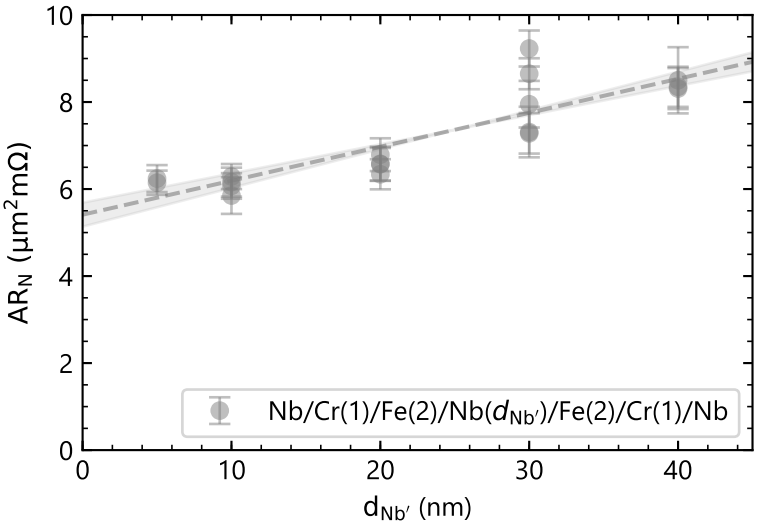


FIGURE 6.2: Area-resistance product against thickness of the Nb interlayer at 1.6 K.

The $R(T)$ behaviour of the devices (shown in Fig. 6.3) provides further insight into the device behaviour. All show a sharp drop where the electrodes become superconducting, followed by a plateau, and then another decrease as the supercurrent proximitizes the junction fully. As $d_{Nb'}$ increases from 5 nm to 30 nm, this full proximitization moves to successively lower temperatures. This can be attributed to the greater thickness of non-superconducting Nb which must be penetrated. The 40 nm device

then proximitizes fully at a higher temperature than the 30 nm device. This indicates a regime change in the behaviour, consistent with the interlayer becoming superconducting. The interplay between the effects of increasing barrier thickness and onset of superconductivity in the interlayer lead to a crossover at around $d_{\mathrm{Nb'}} = 30$ nm. Fig. 6.4 sketches the assumed singlet pair amplitude through the devices in the two regimes.

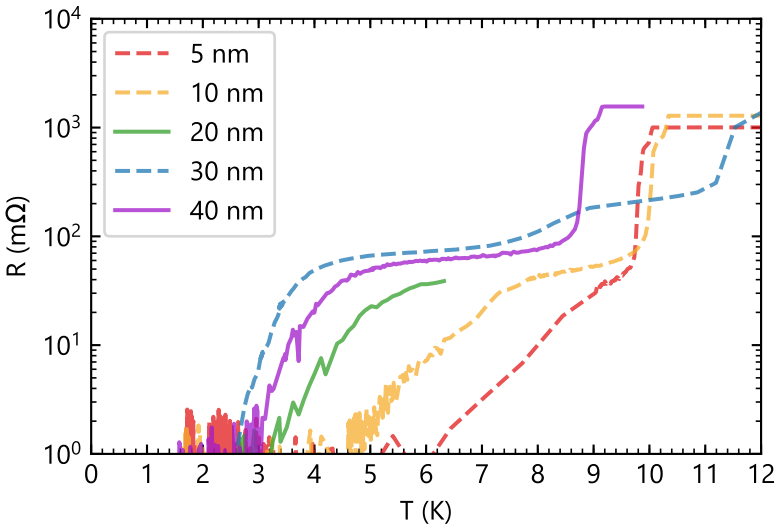


FIGURE 6.3: Top: $R(T)$ curves for a representative Nb/Cr(1)/Fe(2)/Nb'($d_{\mathrm{Nb'}}$)/Fe(2)/Cr(1)/Nb device at each Nb interlayer thickness. Dashed lines indicate quick and uncontrolled cooling upon loading the device into the cryostat, meaning that these curves have errors due to thermal lag between the thermostat and sample. Solid lines indicate slow warming by a PID controlled heater, and so are more reliable. The errors in the red and yellow curves are at most 1 K (by inspecting the superconducting transition of the electrodes) and the error cannot exceed this as the cooling rate slows significantly upon approaching base temperature. Shifting these curves 1 K down in temperature would not change the analysis provided. Similarly, the blue curve with a larger error at the bulk transition can only be shifted to lower temperature in order to correct the error, which again would not change the order in which the curves reach zero resistance.

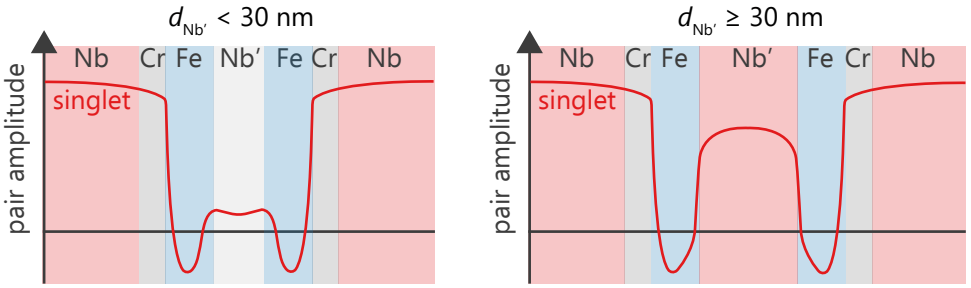


FIGURE 6.4: Schematic illustrations showing the supposed singlet pair amplitude across the devices for both non-superconducting and superconducting interlayers.

Fig. 6.5 shows the $I_c(H)$ dependence of a representative device at each of the interlayer thicknesses studied. We again observe a rough $|\mathrm{sinc}(\Phi)|$ dependence, offset

in field due to the internal magnetic flux. In order to study the periodicity, the model Fraunhofer pattern based on the junction length L is plotted (assuming a rectangular non-magnetic junction with a London penetration depth λ = 90 nm). The model is re-centred on the maximum I_c. With no interlayer, $I_c(H)$ is complicated and lobes beyond the central one become indistinct. Cleaner $I_c(H)$ patterns are observed for the devices with an interlayer. This may indicate that a cleaner magnetic monodomain is formed in the Fe layers when they are separated rather than as a single 4 nm layer. We observe that the central lobe is often narrower than expected from the model. This might be expected from the reversal of the magnetizations of the Fe layers. While others [69] have observed a sharp discontinuous jump in the $I_c(H)$ upon magnetization reversal, here we instead see a gradual reversal roughly over the field range of the principal lobe.

At $d_{Nb'}$ = 30 nm, there appears to be a halving of the period. In addition to inflections in the $R(T)$ and I_cR_N behaviour around this thickness, this is further evidence of the onset of superconductivity in the interlayer. This is thought to be due to the interaction of Andreev bound states at this thickness (see Subsection 2.1.3). When the interlayer is smaller than the coherence length, Andreev states can maintain coherence across both Cr/Fe regions, leading to a larger effective Josephson junction. At $d_{Nb'}$ = 40 nm, the Cr/Fe layers are too far apart for the Andreev states to interact significantly, and the behaviour approaches that of two disconnected Cr/Fe junctions.

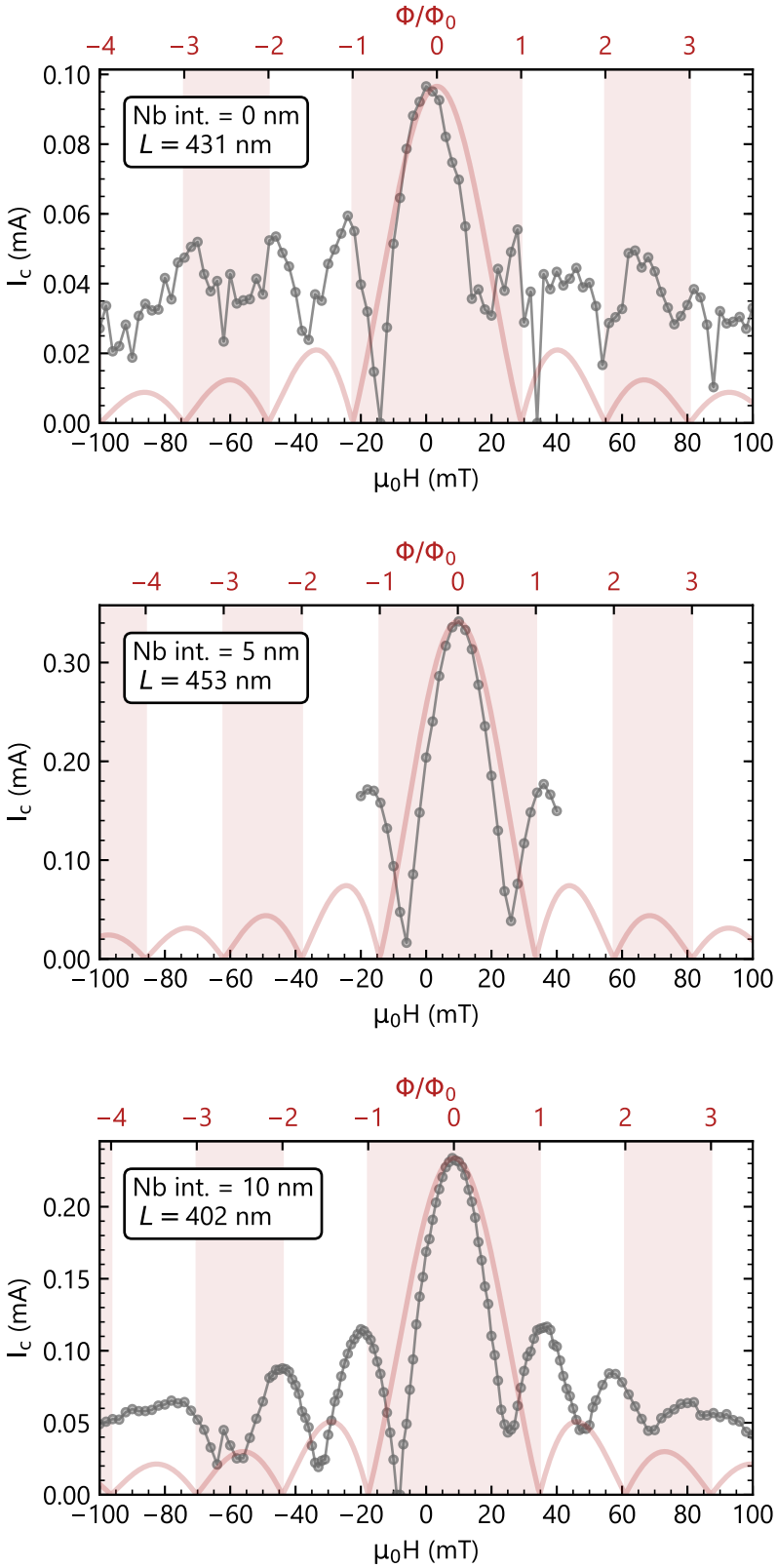


FIGURE 6.5: $I_c(H)$ dependence at 1.6 K (positive sweeps from saturation at −200 mT) of a representative device at each interlayer thickness (grey points). A model Fraunhofer pattern based on the junction length L (red line); the London penetration depth is taken to be 90 nm. (Continues opposite)

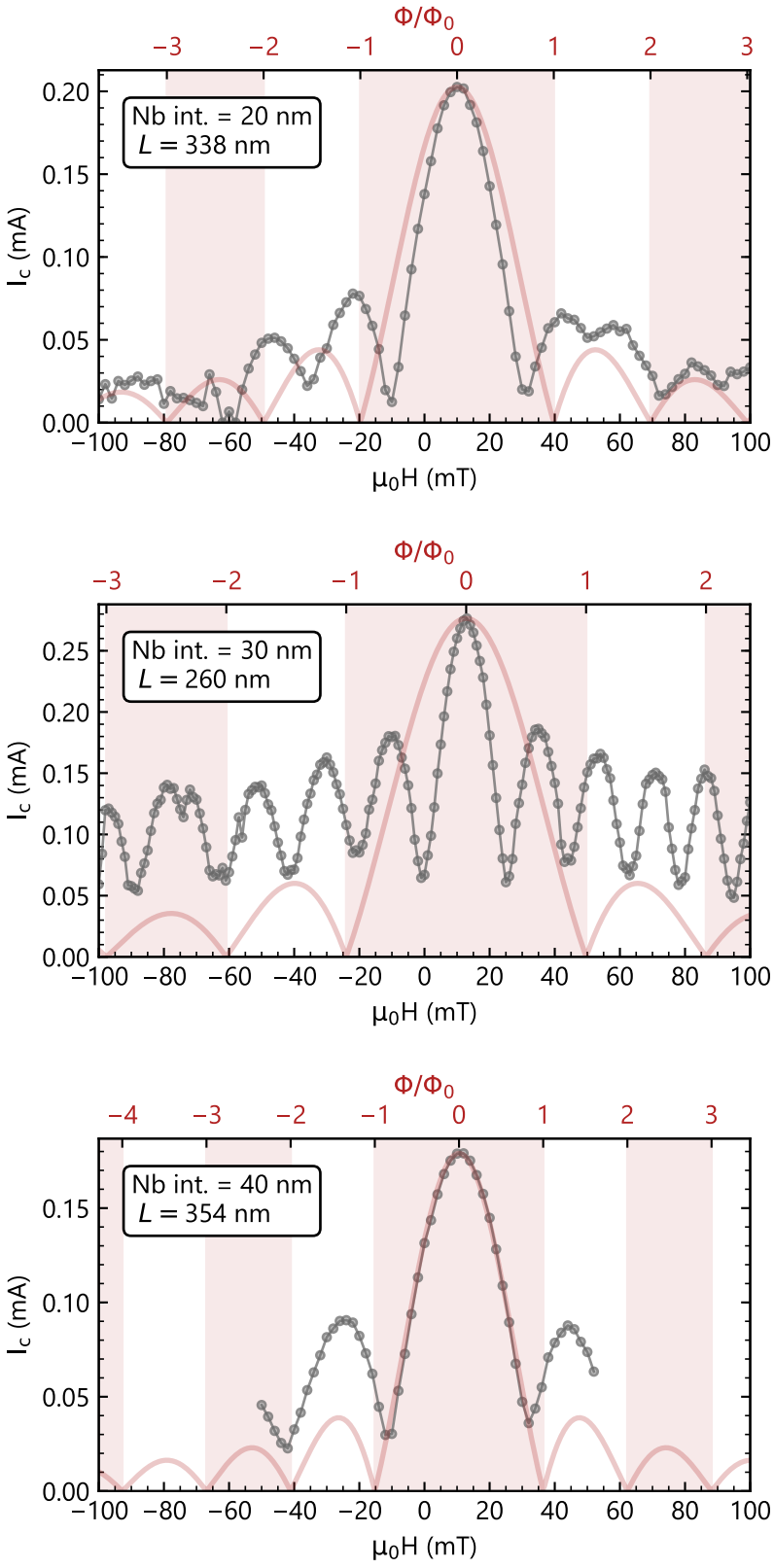


FIGURE 6.5: (Continued) The model Fraunhofer has been re-centred on the peak of $I_c(H)$, which is shifted from zero applied field due to magnetic hysteresis. Shaded regions are an aid to visualize the expected periodicity.

6.1.2 Triplet-dominated interlayer junctions

Now we study the same junction structure with thicker Fe, with the aim of completely suppressing the singlet current. As in the discussion of the previous chapter, in retrospect we cannot be certain that the singlet is completely suppressed in these devices, so we will consider whether subsequent results can be explained in terms of singlet-dominated behaviour. Two thickness combinations were fabricated:

Nb(300)/Cr(1)/Fe(7.5)/Nb'($d_{Nb'}$)/Fe(2.0)/Cr(1)/Nb(300) and
Nb(300)/Cr(1)/Fe(4.8)/Nb($d_{Nb'}$)/Fe(2.4)/Cr(1)/Nb(300).

Choosing asymmetric Fe thicknesses allows us to check for any magnetoresistance effect as the magnetic coercivities of the two layers differ. No magnetoresistance behaviour (i.e., changes of resistance between parallel and antiparallel magnetizations of the Fe layers) was observed at any temperature, which can be explained by the short spin-diffusion length of Nb.

The I_cR_N dependence on interlayer thickness is plotted in Fig. 6.6. Like with the singlet case, there is a decrease in I_cR_N with $d_{Nb'}$ at lower thicknesses, as the triplet pair experiences an increased normal state barrier. The decay constant is < 5 nm, markedly lower than the singlet decay length in normal state Nb of around 50 nm. Unlike in the singlet case, the supercurrent is completely suppressed beyond 10 nm. Even at 40 nm, where we expect the central Nb to be superconducting, I_c remains at zero. Typical $I_c(H)$ measurements for these devices are shown in Fig. 6.7. The $R(T)$ curves of these junctions are shown in Fig. 6.8.

To interpret the behaviour, we offer a speculative explanation in terms of three distinct regimes:

Regime I, $d_{Nb'} < 15$ nm. First we discuss the rapid decay at low Nb thickness compared with the singlet devices; we observe a decay length an order of magnitude smaller, measured here as between 3 nm and 5 nm. Nb has relatively strong SOC [70] [71], which does not break singlets due to time-reversal-symmetry preservation, however it breaks triplet pairs [45]. If we assume the supercurrent is triplet-dominated, the strong SOC is therefore a reasonable explanation for the very short decay length of I_cR_N in Nb compared with the earlier results shown in Fig. 6.1. $I_c(H)$ dependence for devices in this regime are plotted in Fig. 6.7, and show a periodicity reasonably close to the model, again with a slightly narrower central lobe in some cases.

Regime II, 15 nm $\leq d_{Nb'} <$ 30 nm. Secondly, there is a rather sharp transition to zero critical current for the devices beyond 9 nm Nb. Several devices were measured at 15 nm, and none exhibited a supercurrent. The detection limit of our transport measurement corresponds to around $I_cR_N = 0.5\,\mu$V. Extrapolating the decay plotted in Fig. 6.6 we would expect to measure a supercurrent at $d_{Nb'} = 15$ nm, particularly for the thinner Fe devices. The reason for the sudden drop is unclear. Assuming the triplet-dominated interpretation is correct, while the Nb remains normal state between 15 nm-30 nm, the triplet supercurrent cannot traverse the barrier.

Regime III, $d_{Nb'} \geq 30$ nm. In this regime, the Nb is superconducting, as evidenced by secondary drops in the $R(T)$, although a finite resistance remains down to base

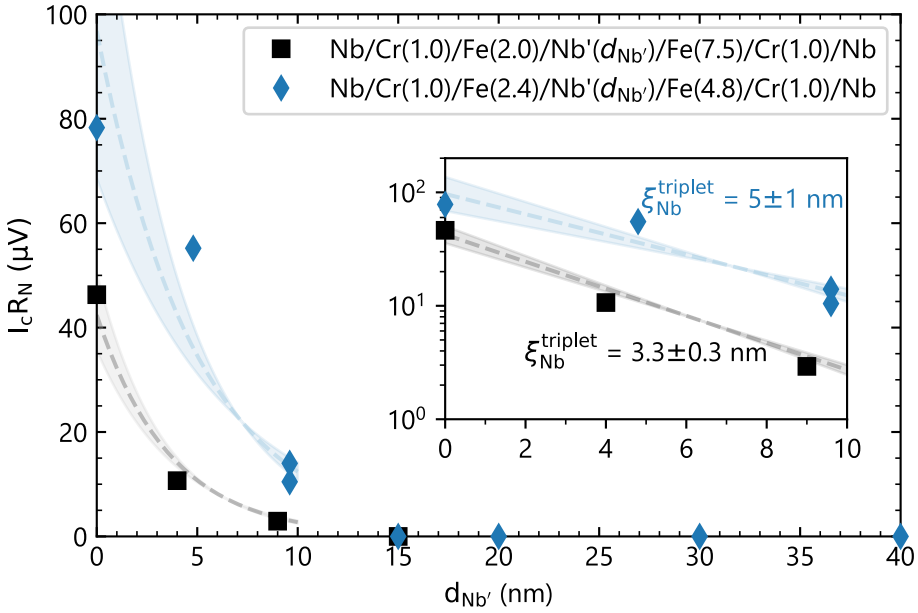


FIGURE 6.6: Decay of I_cR_N with thickness of the Nb interlayer $d_{Nb'}$ at 1.6 K in Nb(300)/Cr(1)/Fe(7.5)/Nb'($d_{Nb'}$)/Fe(2.0)/Cr(1)/Nb(300) devices and Nb(300)/Cr(1)/Fe(4.8)/Nb'($d_{Nb'}$)/Fe(2.4)/Cr(1)/Nb(300) devices. The points at $d_{Nb'} = 0$ nm have been interpolated from the data in Fig. 5.3. Inset: The same data on a log scale concentrating on the first regime where the supercurrent decays with the increasing thickness of normal state Nb interlayer. As discussed in the text, we speculate that this is the decay length of triplet pairs in normal state Nb. A least-squares fit for each set of devices allows us to estimate the decay length. The shaded region represents the standard deviation of the fit. The estimates obtained from each set are shown on the plot along with their standard errors. A variance-weighted average of the two estimates gives $\xi_{Nb}^{triplet} = (3.4 \pm 0.3)$ nm.

temperature. The lack of any recovery of the supercurrent is a marked contrast to the measurements of devices with thinner Fe layers in Fig. 6.1, where the supercurrent increased again as the interlayer became superconducting. This difference is difficult to explain under the hypothesis that singlet correlations dominate the device behaviour. We would expect the value of I_cR_N to increase above even the values measured with no interlayer as we would now have effectively two Josephson junctions in series. This difference in behaviour motivates a triplet-based explanation, suggesting that the supercurrents measured for lower interlayer thicknesses were triplet-dominated. Under such an explanation, we might still hypothesize that the onset of superconductivity in Nb would lead to a supercurrent being recovered. In the absence of spin-mixers at the interfaces of the superconducting interlayer, the supercurrent would need to be mediated by a double-Andreev reflection process, and therefore dominated by a second-harmonic component. Since our devices show no supercurrent, we conclude that no such process occurs here. Unlike in the singlet-case where we observe a transition to a double-junction regime and an increase in I_cR_N, no superconducting transport occurs. This is because the singlet component falls to zero in the thicker F layer, and the triplet

component falls to zero in the superconducting Nb interlayer. We conclude that the recovery of singlet superconductivity in the interlayer does not result in a supercurrent being supported across the device.

The schematic illustration in Fig. 6.8 shows the proposed explanation for the device behaviour by considering the singlet and triplet components of the supercurrent. In these triplet devices, the singlet component decays and oscillates in the ferromagnetic layers, falling to zero (at least below the detection limit) inside the junction. The triplet component decays exponentially in Fe, with a decay constant comparable to that of singlets in a normal metal $\xi_{\mathrm{Fe}}^{\mathrm{triplet}} = (\hbar D_{\mathrm{F}}/2\pi k_{\mathrm{B}}T)^{1/2}$.

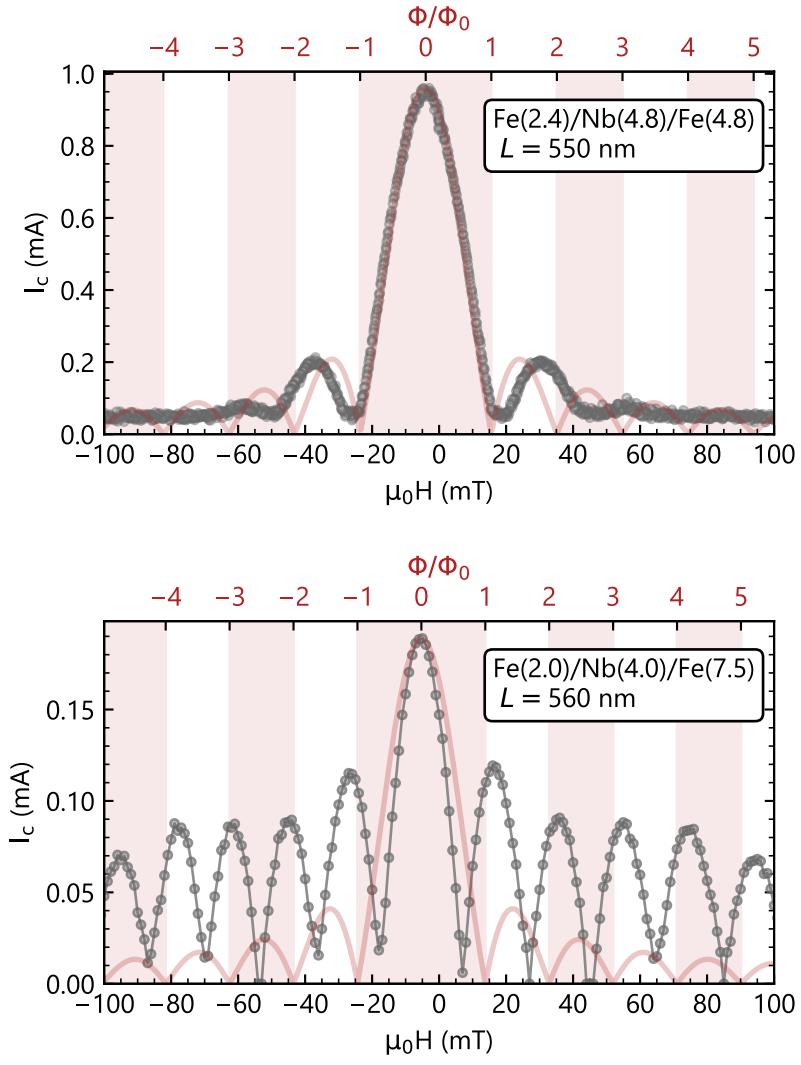


FIGURE 6.7: $I_{\mathrm{c}}(H)$ dependence of the Nb/Cr(1)/Fe/Nb′/Fe/Cr(1)/Nb devices at 1.6 K (where the central Fe and Nb′ layer thicknesses are quoted in the boxes on the plots) from saturation at 200 mT applied field, swept in the negative direction (grey points). A model Fraunhofer pattern based on the junction length L (red line); the London penetration depth is taken to be 90 nm. The model Fraunhofer has been re-centred on the peak of $I_{\mathrm{c}}(H)$, which is shifted from zero applied field due to magnetic hysteresis. Shaded regions are an aid to visualize the expected periodicity.

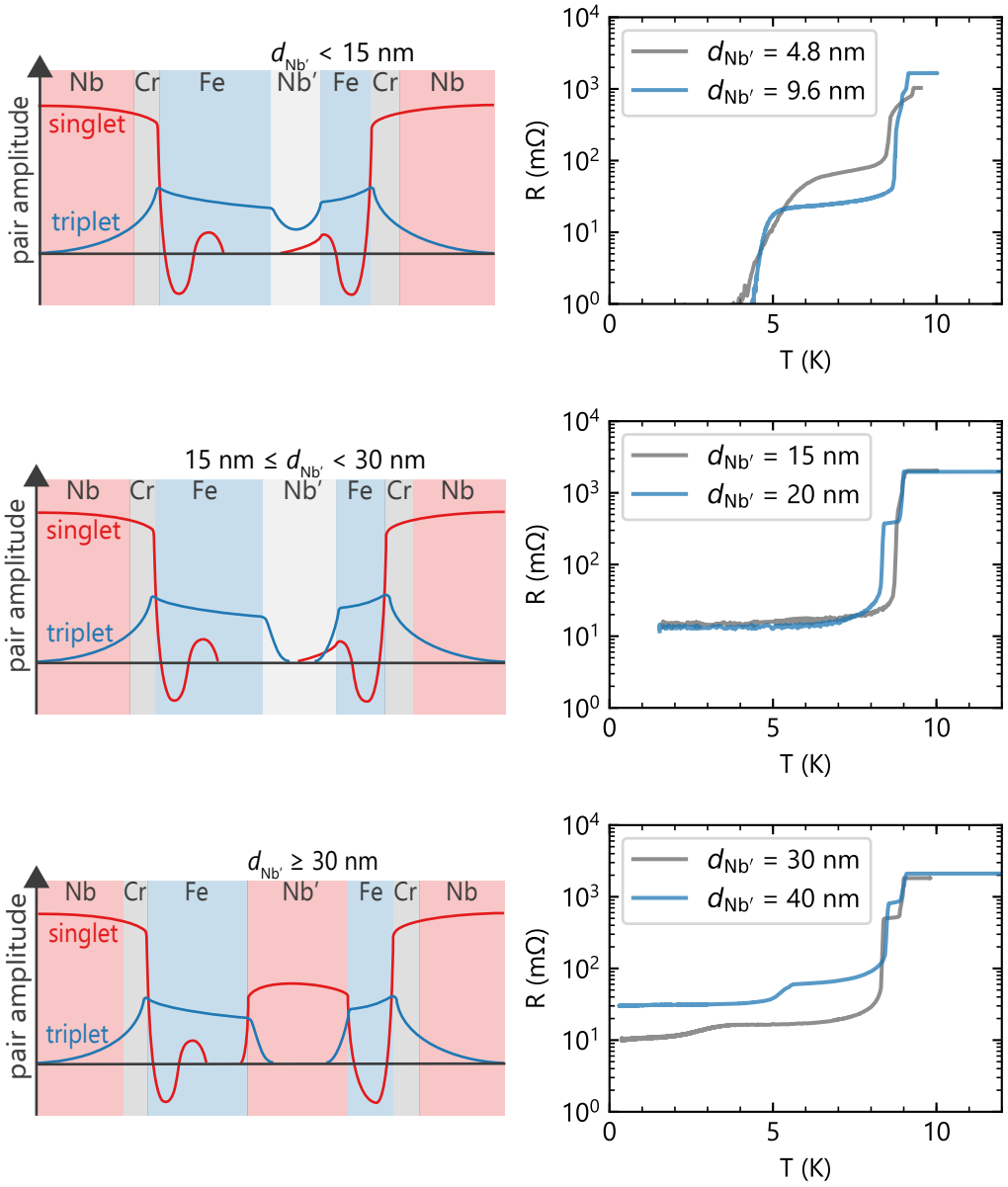


FIGURE 6.8: Left: schematic illustrations showing the proposed variation of the singlet and triplet pair amplitudes across the junctions for each of the three regimes dependent on the Nb interlayer thickness. Right: $R(T)$ curves for devices in each of these three regimes. For $d_{Nb'} < 15\,nm$, the devices support a Josephson supercurrent carried by spin-triplet pairs. For $15\,nm \leq d_{Nb'} < 30\,nm$, the triplet component has decayed below the detection limit in the Nb interlayer. For $d_{Nb'} \geq 30\,nm$, the interlayer becomes superconducting (as evidenced by the drops in resistance at around 3.0 K for $d_{Nb'} = 30\,nm$ and 5.5 K for $d_{Nb'} = 40\,nm$) and so the singlet pairs are present, but the triplet component does not recover and so no Josephson supercurrent is observed.

6.2 Conclusions

The previous chapter showed some indications of Cr/Fe interfaces generating long-ranged triplet correlations, but the limited data left ample room for doubt. The aim of the experiments of this chapter was to propagate triplets through an intermediary

superconductor, but without robust evidence of triplet generation we must interpret the results here more carefully.

Devices with relatively thin ferromagnetic layers provide a control experiment dominated by singlet superconductivity, where we see that there is a transition from a non-superconducting to a superconducting Nb interlayer at a critical interlayer thickness of around 30 nm. While the interlayer is non-superconducting, the decay constant of the singlet supercurrent in normal state Nb is around 50 nm. When the interlayer becomes superconducting, a rise in critical current is seen. For devices with thicker ferromagnetic layers, which we hypothesized to be dominated by long-ranged triplet correlations, we study a similar thickness range for the interlayer. In this case, the decay of the supercurrent in normal state Nb is much more rapid than it was for the thinner Fe control experiment, with a decay constant of only 3 nm-5 nm. In the regime where the interlayer is superconducting, instead of reaching a singlet-supported double Josephson junction, the critical current remains at zero. This is a dramatic contrast to the thinner Fe experiment where the critical currents increase again for thicker interlayers. This suggests that in the thicker Fe experiment, the Fe layers are sufficient to suppress the singlet supercurrent. The smaller decay constant and the lack of recovery of the supercurrent, even with thicker superconducting interlayers, motivates us to conclude that the supercurrents in the thicker Fe experiment are dominated by spin-aligned triplet pairs. However, we recognize that once again data points are limited, and without more robust and reproducible device behaviour these conclusions are somewhat speculative.

If the triplet-based explanation is correct, we further note that the lack of recovery of a supercurrent for superconducting interlayers means that there is no conversion from triplet to singlet at the interlayer. Under this explanation, although at every position between the superconducting electrodes at least one of the singlet component or the triplet component is non-zero, there is no interconversion possible at the Fe/Nb' interfaces, and so no supercurrent is measured across the device.

Chapter 7

Josephson junctions with strong spin-orbit coupling

Several theoretical works have described how spin-orbit coupling may rotate the spin of Cooper pairs and generate a LRT (see Subsection 2.3.5). Following on from the work of Jeon et al. on spin-pumping through a superconductor in the presence of strong spin-orbit coupling (see Subsection 2.3.6), the next question was whether spin-orbit coupling could be used to generate a spin-triplet supercurrent in an equilibrium experiment.

To work towards answering this question, I first study the decay of supercurrents in Pt, the material which will be used to provide the spin-orbit coupling. Then, S/N/S/N/S junctions where N is Pt will provide a useful control for the behaviour of singlets where there is a superconducting interlayer. Finally, I attempt to generate a long-ranged triplet supercurrent through a ferromagnet Co, where spin-mixing is expected to be achieved through a combination of spin-orbit coupling and an exchange field. This will provide the groundwork for the more directly comparable experiments to those of Jeon et al. presented in the following chapter.

The device fabrication and measurements in this chapter are the sole work of the author.

7.1 Nb/Pt/Nb junctions

To study the basic properties of Pt as a Josephson barrier, two series of Nb/Pt/Nb S/N/S junctions were fabricated. In the first deposited series (Depo. 1) the thickness of Pt was limited to 23-49 nm, and in the second (Depo. 2) a range of 34-77 nm was used. The resulting J_c values are shown in Fig. 7.1. The data are consistent with an exponential decay of J_c with increasing Pt thickness d_{Pt}; this is the expected dependence of J_c on the thickness of the normal-state layer [31]. The Depo. 2 data have considerably greater scatter. Run-to-run variation in the deposition conditions means that the data are best viewed as two separate sets, and fits to the data will be performed on them separately. Performing a least-squares straight line fit to $\ln(J_c)$ against Pt thickness for each deposition yields an estimate of the gradient $m = -1/\zeta_{Pt}$. The standard error of the estimate m can then be used to find one standard deviation upper and

lower limits for ξ_{Pt}. Note that the error in ξ_{Pt} is asymmetric due to the reciprocal relationship between ξ_{Pt} and m. Table 7.1 shows the results. The best estimate of ξ_{Pt} can be found by performing a weighted average of the Depo. 1 and Depo. 2 estimates of m, with the weights as $1/(\Delta m)^2$. This gives the best estimate for the normal-state coherence length of Pt as $\xi_{Pt} = (24 \pm 2)$ nm, using the standard error of m. Fig. 7.2 shows $I_c R_N$ against d_{Pt}, showing similar behaviour to J_c.

TABLE 7.1: Estimation of the normal state coherence length of Pt from the decay of J_c. m is the gradient of a straight-line least-squares fit to $\ln(J_c)$, such that $m = -1/\xi_{Pt}$. The weighted and combined data is used to give the final estimate and its error.

	m	Δm	ξ_{Pt}^{lower} (nm)	ξ_{Pt}^{best} (nm)	ξ_{Pt}^{upper} (nm)
Depo. 1	-0.04311	0.00271	21.8	23.2	24.8
Depo. 2	-0.03441	0.00931	22.9	29.1	39.8
Weighted combined data	-0.04243	0.00237	22.3	**23.6**	25.0

We can also estimate the value of ξ_{Pt} from the theoretical expression for the coherence length in the ballistic limit ξ_{Pt}^0, together with an estimate of the mean free path l_{Pt} from the resistivity ρ_{Pt} to find the coherence length in the diffusive limit ξ_{Pt}. In the clean limit, where the mean free path is longer than the coherence length, $\xi_N^0 = \hbar v_F / 2\pi k_B T$. Using $v_F = 4.40 \times 10^5$ m/s [72] gives $\xi_{Pt}^0 = 127$ nm at 4.2 K. In the diffusive limit, the coherence length is instead $\xi_N = \sqrt{\xi_N^0 l/3}$ [31]. We can calculate l_{Pt} from the resistivity ρ_{Pt}, extracted as the gradient of the fit to $AR_N(d_{Pt})$ in Fig. 7.3. From Ashcroft and Mermin [73], $l = 9.2\,\text{nm} \times [(r_s/a_0)^2/\rho]$ where $r_s/a_0 = 5.44 \times [n_{22}]^{1/3}$ and $n = n_{22} \times 10^{22}/\text{ cm}^3$. The gradient of the graph gives $\rho_{Pt} = 7.5\,\mu\Omega\,\text{cm}$ and using $n_{22} = 4.96$ [72] gives $l = 13^{+4}_{-3}$ nm, with errors from the fit. Therefore we obtain $\xi_{Pt} = 23^{+4}_{-3}$ nm, using the standard error in estimating ρ_{Pt}. This agrees with the coherence length calculated from the decay of the critical current density. The diffusive-limit coherence length is dependent on the residual resistivity ρ_{Pt} and therefore on the microstructural defects of the sputtered thin films. Studying the $I_c(H)$ dependence of the Nb/Pt/Nb Josephson junctions is useful to confirm proper device fabrication. Fig. 7.4 shows $I_c(H)$ for one of the devices with a 34 nm Pt barrier. The data follow the expected theoretical dependence of a $|\text{sinc}(\Phi)|$ function quite well. The I_c values within the tertiary lobes fall below the theoretical ratio of the $I_c(0)$ value, which may be due to a combination of device imperfections and the method of extracting I_c (see Section 3.4). Fig. 7.5 shows the comparison of the fitted model $|\text{sinc}(\Phi)|$ function against the junction length L measured under SEM. For the model, we take $\lambda = 90$ nm and assume that the electrode thickness (300 nm) is much greater than the penetration depth (see Subsection 2.2.4). It can be seen that the Fraunhofer patterns follow what we expect from the device dimensions well, again with more scatter in Depo. 2 than

Depo. 1. This provides confidence that the junction fabrication is reliable.

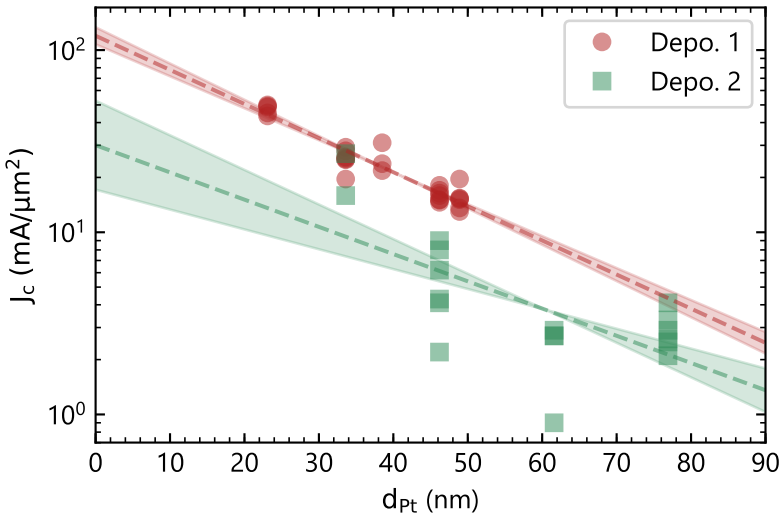


FIGURE 7.1: Decay of J_c with Pt thickness in Pt S/N/S junctions at 4.2 K. The shaded regions indicate the one standard deviation range of the gradient and intercept from the least-squares fit. Errors in individual measurements are smaller than the markers.

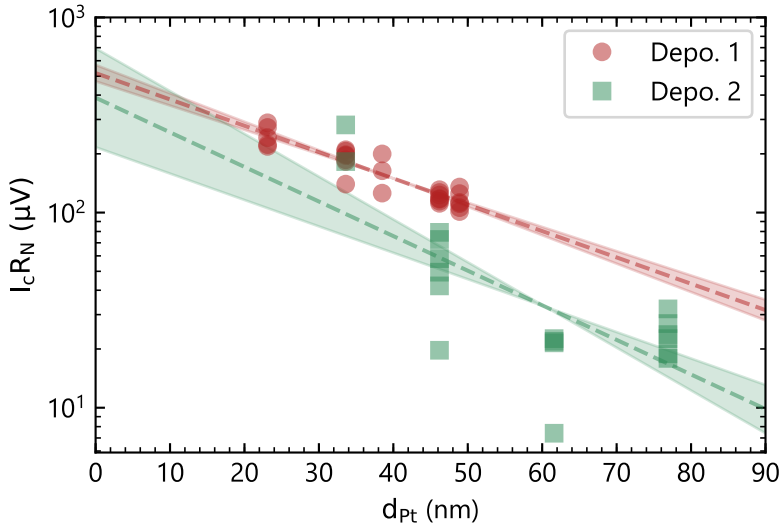


FIGURE 7.2: Decay of I_cR_N with Pt thickness in Pt S/N/S junctions at 4.2 K. The shaded regions indicate the one standard deviation range of the gradient and intercept from the least-squares fit. Errors in individual measurements are smaller than the markers.

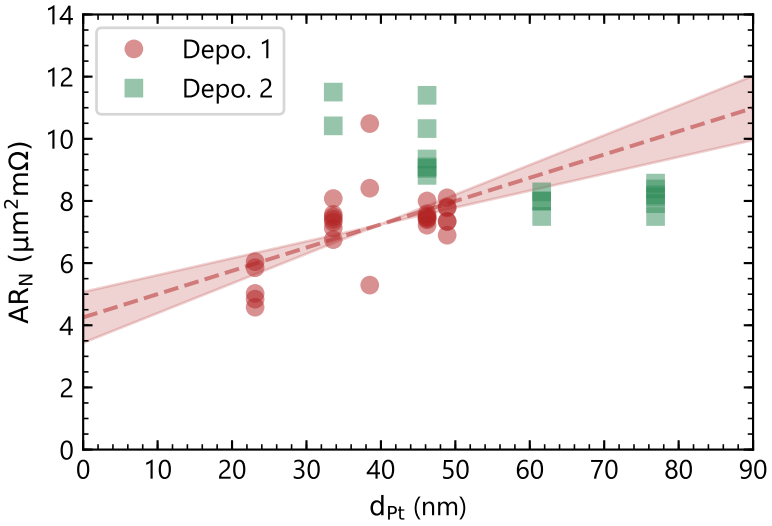


FIGURE 7.3: AR_N variation in Pt S/N/S junctions at 4.2 K. Errors in individual measurements are smaller than the markers.

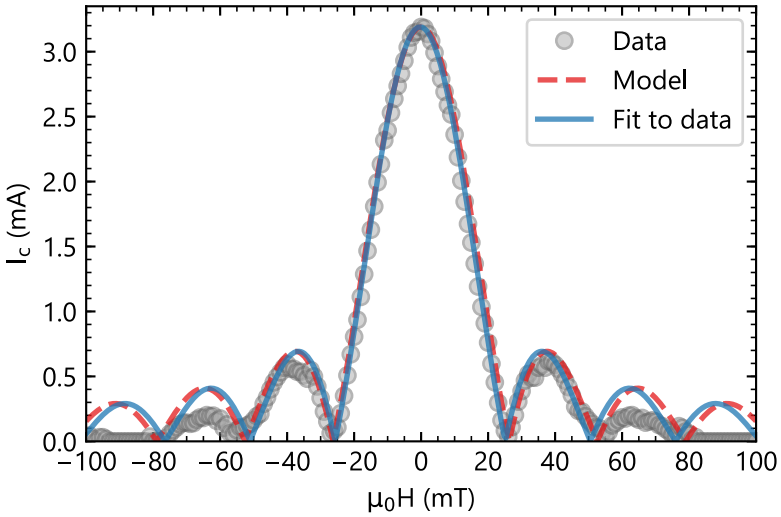


FIGURE 7.4: $I_c(H)$ for a Nb/Pt(34)/Nb junction at 4.2 K. The red dashed line is the Fraunhofer model based on the SEM-measured junction length L of 368 nm. The blue solid line is a fit to the data with L unconstrained and λ = 90 nm, returning L = 381 nm, close to the measured value.

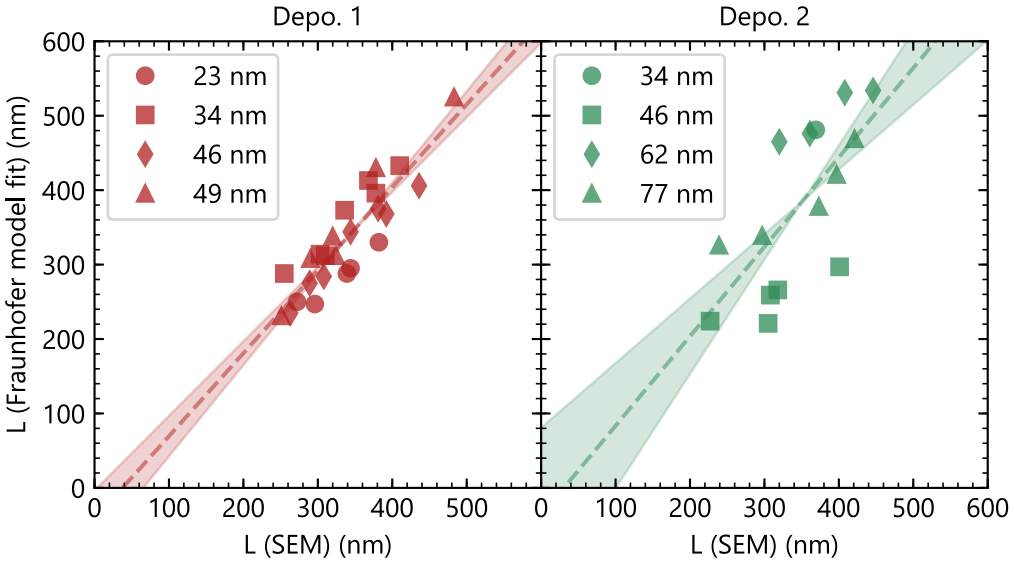


FIGURE 7.5: L extracted by fitting a Fraunhofer model to the $I_c(H)$ of Nb/Pt/Nb Josephson junctions at 4.2 K plotted against L measured by SEM.

7.2 Nb/Pt/Nb/Pt/Nb junctions

I now turn to the case of S/N/S/N/S junctions where N is Pt. This is important as a control experiment, as this thesis will later explore the behaviour of devices with superconducting interlayers in combination with ferromagnets and strong spin-orbit coupling. By comparison, the behaviour of Nb/Pt/Nb/Pt/Nb devices is more readily interpretable and we expect only a singlet component to the supercurrent. It will then be possible to explore any differences that might arise in the experiments combining ferromagnetism and strong spin-orbit coupling.

The multilayer structure was Nb/Pt(25)/Nb($d_{Nb'}$)/Pt(25)/Nb, with $d_{Nb'}$ taking values of 0 nm, 22 nm, 45 nm, and 89 nm; a range from control devices with no interlayer up to more than twice the coherence length of Nb. Choosing a total Pt thickness of 50 nm allows for appreciable suppression of the critical current I_c of the junction, such that I_c can be measured without driving the nanopillar itself into the normal state.

Measurements of the critical current density J_c and the characteristic voltage I_cR_N as a function of interlayer thickness $d_{Nb'}$ are presented in Fig. 7.6. It is observed that both J_c and I_cR_N rise as $d_{Nb'}$ is increased, indicating that the interlayer is already superconducting by 22 nm. While the data are too sparse to infer a clear form of the dependence, they are consistent with a plateau being reached beyond a coherence length of the superconducting interlayer.

This behaviour is consistent, at least qualitatively, with the expected behaviour of two Josephson junctions in series in an S/N/S/N/S device. For $d_{\mathrm{Nb}'} \gg \xi$, we expect the behaviour to approach that of a single Nb/Pt(25)/Nb junction, since the coherence of the Cooper pairs is lost between the two Pt layers. As $d_{\mathrm{Nb}'}$ is decreased, we expect $I_{\mathrm{c}}R_{\mathrm{N}}$ to be suppressed as the two Josephson junctions begin to interact. Finally, we should see a Nb/Pt(50)/Nb junction where there is no interlayer. The values of $I_{\mathrm{c}}R_{\mathrm{N}}$ in the extreme cases $d_{\mathrm{Nb}'} \gg \xi$ and $d_{\mathrm{Nb}'} = 0\,\mathrm{nm}$ are similar to those seen for simple S/N/S junctions with Pt above, at 25 nm and 50 nm Pt respectively (differences being attributed to run-to-run variation in deposition).

Zapata and Sols [41] calculate the theoretical dependence of J_{c} on the distance between the normal-state regions, and find a solution which starts out with J_{c} suppressed at zero distance and a plateau in the long-distance limit, corresponding to the J_{c} of a single non-interacting junction as observed in our data (see Subsection 2.2.6). They predict an initial decrease in J_{c} for distances less than the coherence length, the depth of which depends on the strength of the barriers. The data here are not complete enough to observe this initial decrease.

A further prediction of Zapata and Sols is that the $I_{\mathrm{c}}(T)$ dependence of the junctions should decay as $\sqrt{T_{\mathrm{c}}' - T_{\mathrm{c}}}$ for S/N/S/N/S and $(T_{\mathrm{c}} - T)^2$ for S/N/S junctions, where $T_{\mathrm{c}}' < T_{\mathrm{c}}$, i.e. the temperature at which I_{c} becomes zero is lower in the S/N/S/N/S case.

$I_{\mathrm{c}}(T)$ plots for the devices are shown in Fig. 7.7. All of the curves are concave, and so are closer to $(T_{\mathrm{c}} - T)^2$ dependence than $\sqrt{T_{\mathrm{c}}' - T_{\mathrm{c}}}$. This would suggest S/N/S behaviour in all cases, and the predicted behaviour for S/N/S/N/S junctions is not observed. Furthermore, the theoretical prediction that S/N/S/N/S behaviour causes a suppression of T_{c} is not seen. Instead, the thinnest interlayer has a similar T_{c} to the control S/N/S junction, with subsequent monotonic increases in the T_{c} of the devices for thicker interlayers. It should be noted that Zapata and Sols assume delta-function-like barriers for their theoretical treatment; the 25 nm Pt layers here will cause significant deviation from the theory.

$R(T)$ curves (Fig. 7.8) for the devices tell a similar story, where the device with the thickest interlayer is the first to fully proximitize as the temperature is reduced. In this plot, there is a clearer separation between the device without an interlayer and the device with a 22 nm interlayer, showing that the T_{c} of the latter is suppressed relative to that of the former. Then, as the interlayer thickness is increased further, the device T_{c} monotonically rises again. This may be interpreted as the thin interlayer having a suppressed T_{c}, and therefore presenting an additional barrier to full proximitization. Then, thicker interlayers have higher T_{c}, and for the thickest interlayer, the barrier to proximitization is simply a 25 nm Pt layer as the central Nb T_{c} approaches that of the bulk.

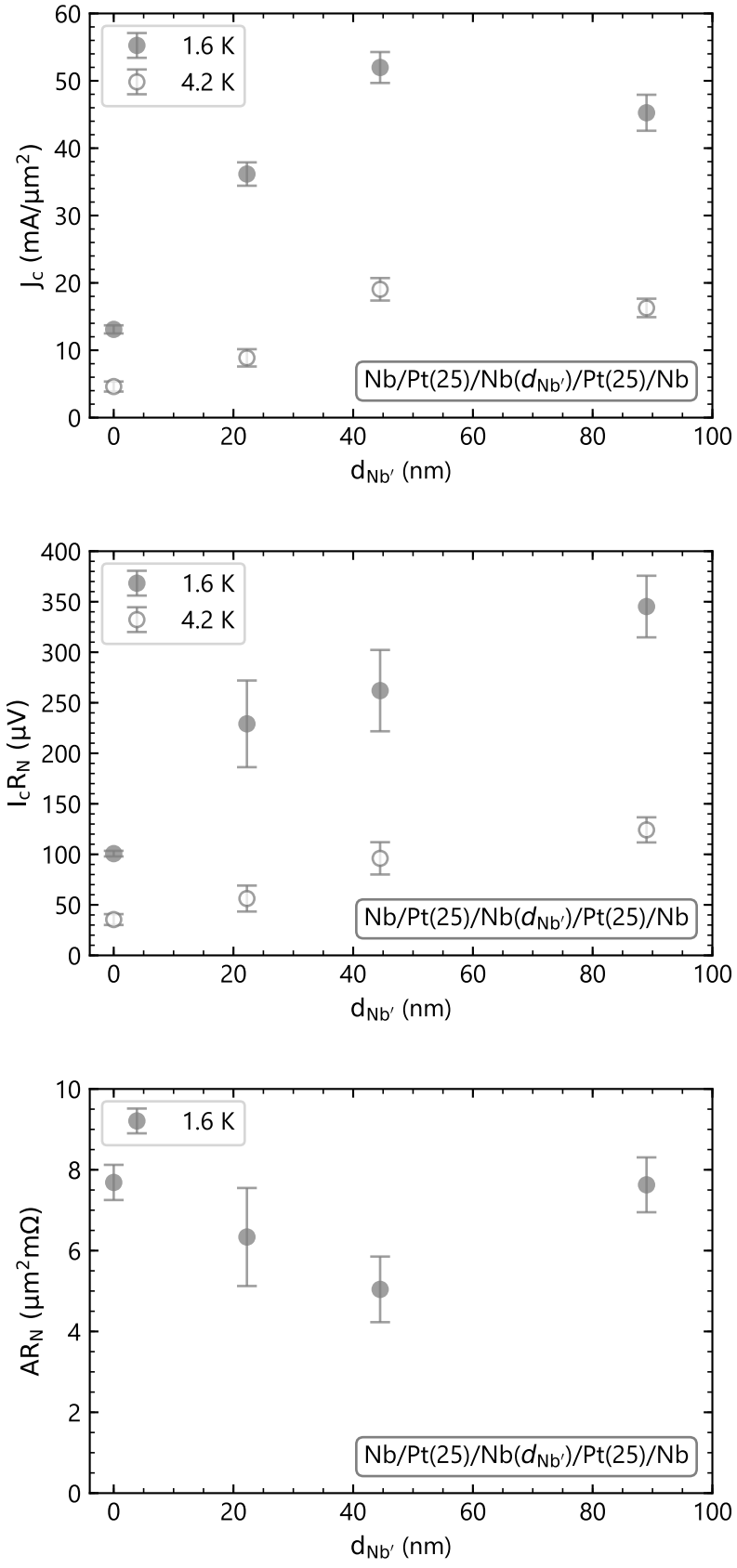


FIGURE 7.6: Variation of J_c, I_cR_N and AR_N with interlayer thickness from 0-89 nm for a series of Nb/Pt(25)/Nb($d_{Nb'}$)/Pt(25)/Nb junctions.

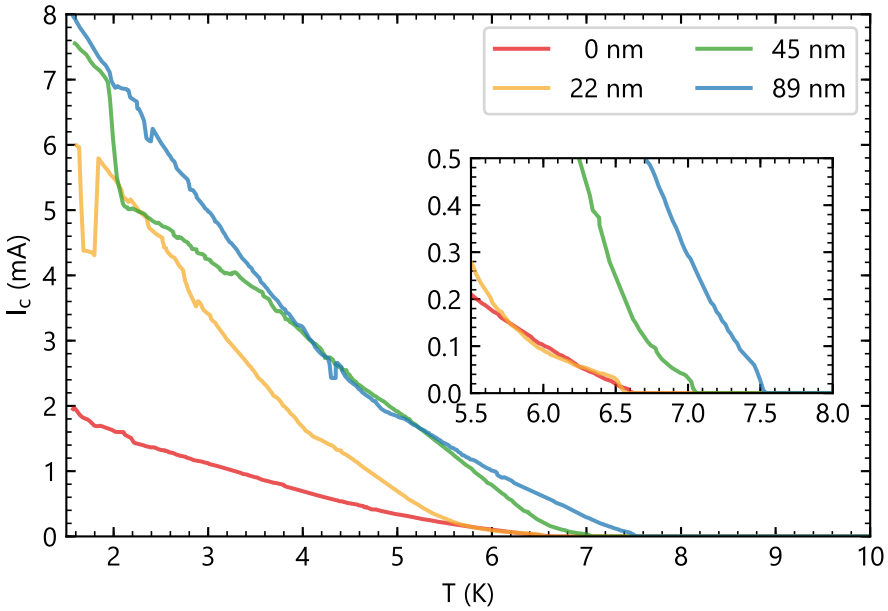


FIGURE 7.7: $I_c(T)$ for patterned Nb/Pt(25)/Nb($d_{Nb'}$)/Pt(25)/Nb devices, with the interlayer thickness varying from 0-89 nm. Inset: Detail near zero critical current.

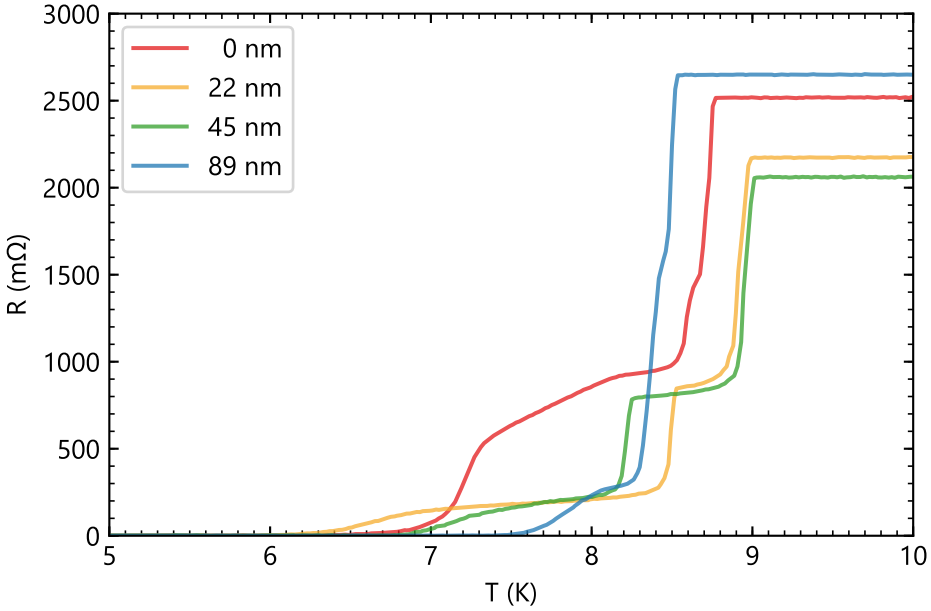


FIGURE 7.8: $R(T)$ curves of patterned Nb/Pt(25)/Nb($d_{Nb'}$)/Pt(25)/Nb devices, with the interlayer thickness varying from 0-89 nm. The 89 nm device is from a different deposition from the other three. The reason for the depression in the bulk critical temperature for the 0 nm and 89 nm curves is unclear, but the focus of the discussion here is on the temperature at which full proximitization is achieved.

7.3 Nb/Pt/Co/Pt/Nb junctions

It has recently been proposed that spin-orbit coupling (SOC) may substitute the role of the magnetic inhomogeneity in interconverting the triplet states (see Subsection 2.3.5); to investigate this I fabricate devices with Pt/Co interfaces. The SOC arises from the high atomic number of Pt and broken inversion symmetry at its interfaces, and is of pure Rashba type. The generation of the LRT only occurs when the Rashba and exchange field vectors are neither parallel nor perpendicular.

Co/Pt bilayer and multilayer structures are known to exhibit an out-of-plane magnetic anisotropy [74]. This appears promising as a means to achieve an exchange field at some angle between 0° and 90° to the interface and therefore satisfy the condition for LRT generation.

7.3.1 Magnetic characterisation

Two series of Nb/Pt(d_{Pt})/Co(1.5)/Pt(d_{Pt})/Nb films were deposited. Devices were fabricated from Series 1 only, as the Series 2 films were deposited at the end of this research. The magnetic behaviour of both series of unpatterned Nb/Pt(d_{Pt})/Co(1.5)/Pt(d_{Pt})/Nb films was examined by room temperature VSM (with some limited SQUID measurements at 10 K). The nanopillars fabricated later will likely be magnetic monodomains, hence the behaviour of the unpatterned films will only serve as a rough guide to the possible magnetic behaviour of the nanopillar.

Fig. 7.9 shows $M(H)$ loops for both series of unpatterned films, both in-plane (IP) and out-of-plane (OOP). Fig. 7.10 shows the 10 K SQUID $M(H)$ data taken for Series 1. After the measurement, these loops were found not to have reached saturation, and so subtraction of the background diamagnetic signal from the substrates had to be estimated. This was done by choosing the smallest correction factor that would ensure that all of the curves attained non-negative gradients at the high-field limit, and the same correction factor was applied to all the curves. While this means the picture is somewhat incomplete, some inferences can nonetheless be made. The IP coercivity of the sample with Pt is higher than the IP coercivity without Pt, showing that the easy axis is rotated out of plane by Pt. This is further evidenced by the OOP curves; with Pt the IP and OOP curves are close to converging at the high-field limit; without Pt the IP and OOP curves are still distant.

For total Pt thicknesses $2d_{\mathrm{Pt}} < 3$ nm, the magnetic easy axis is largely in-plane. For $2d_{\mathrm{Pt}} > 3$ nm, the magnetic easy axis is largely out-of-plane. This is easier to see in Fig. 7.11, where the remanent magnetization per unit area m_{r}/A is plotted as a function of $2d_{\mathrm{Pt}}$. The plot shows effectively zero OOP remanence at $2d_{\mathrm{Pt}} < 3$ nm and then a large OOP remanence for $2d_{\mathrm{Pt}} > 3$ nm. The IP remanence first rises with increasing Pt thickness for $2d_{\mathrm{Pt}} < 3$ nm due to proximity-induced magnetism (see Subsection 1.1.4) and then becomes close to zero for total Pt thicknesses $2d_{\mathrm{Pt}} \geq 4$ nm.

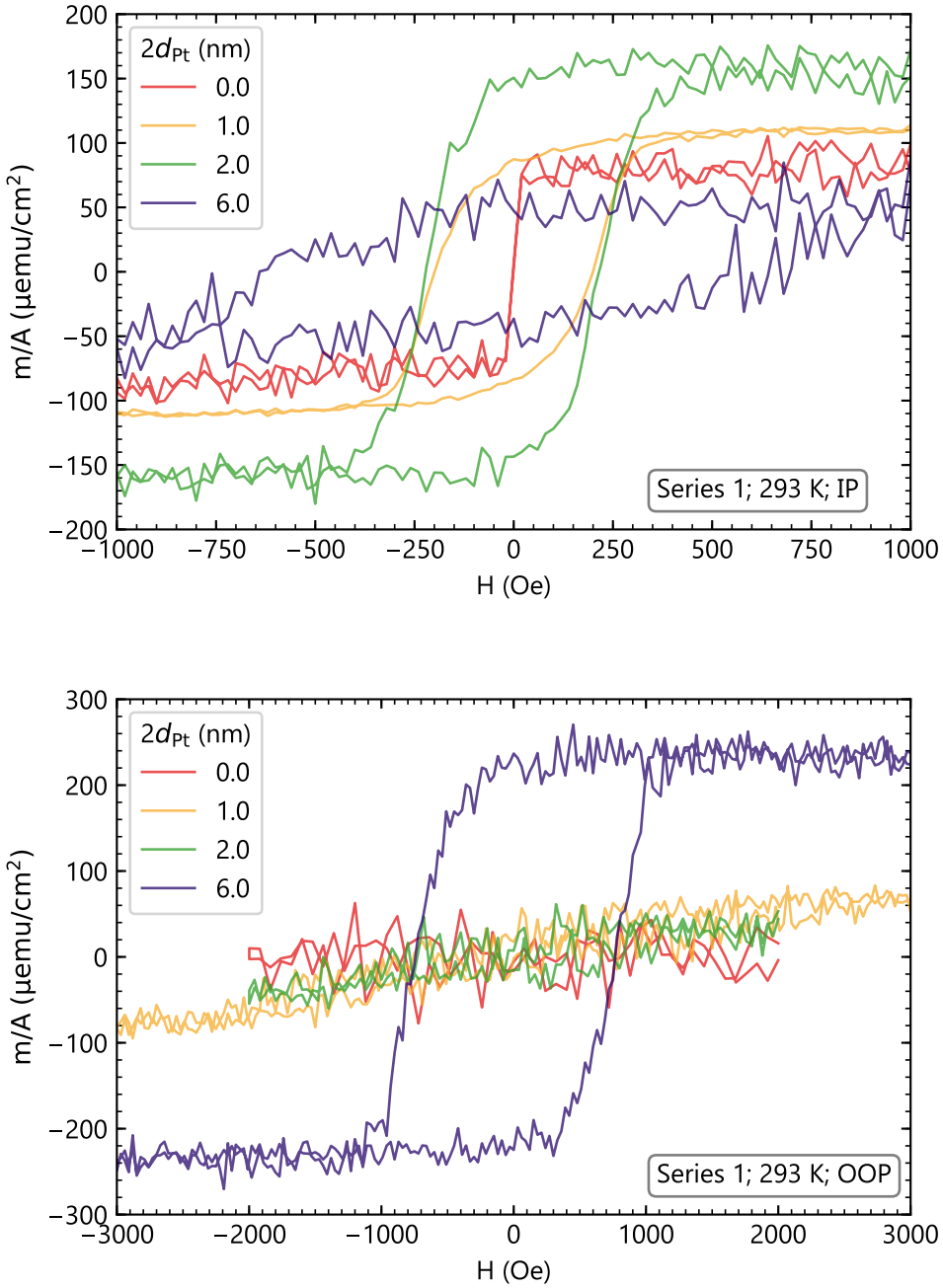


FIGURE 7.9: $M(H)$ loops measured by room temperature VSM for a series of unpatterned Nb/Pt(d_{Pt})/Co(1.5)/Pt(d_{Pt})/Nb (Series 1) films.

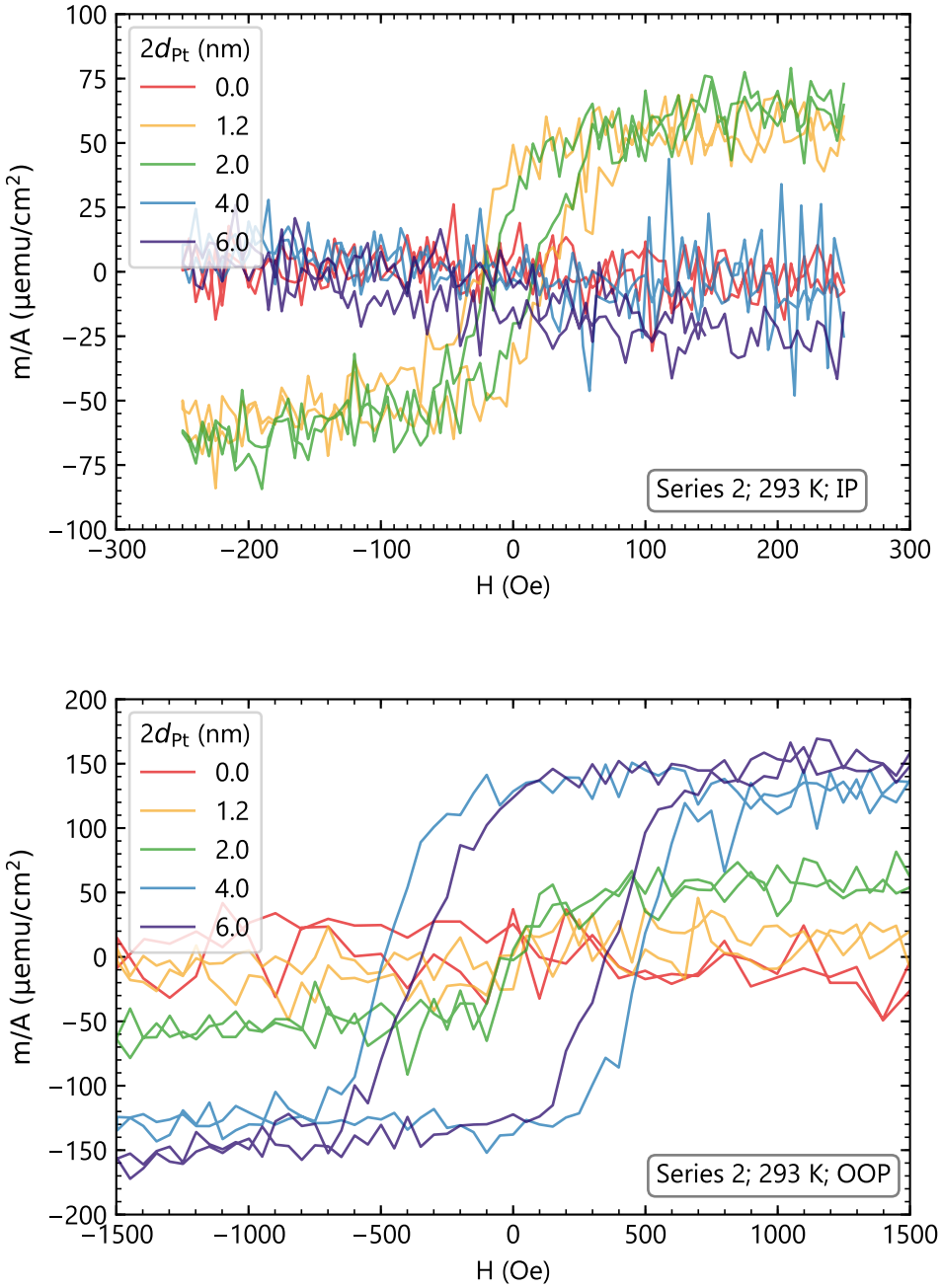


FIGURE 7.9: (Continued) $M(H)$ loops measured by room temperature VSM for a series of unpatterned Nb/Pt(d_{Pt})/Co(1.5)/Pt(d_{Pt})/Nb (Series 2) films.

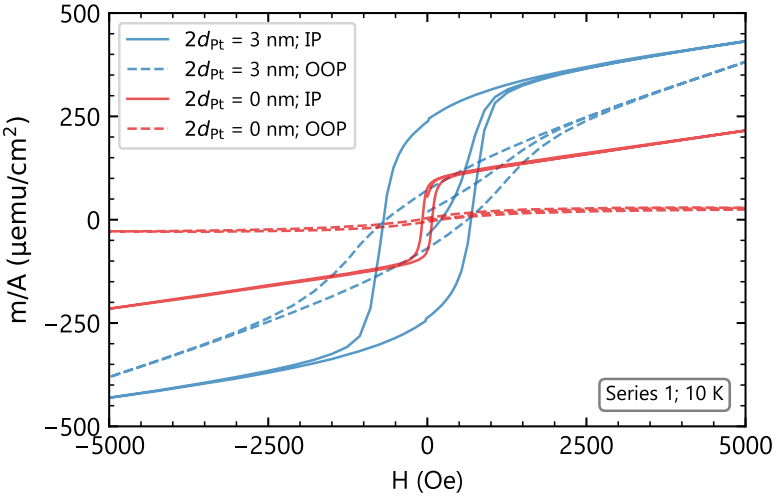


FIGURE 7.10: Nb/Pt(d_{Pt})/Co(1.5)/Pt(d_{Pt})/Nb (Series 1) film SQUID $M(H)$ loops at 10 K. An approximate lower-limit diamagnetic background subtraction has been applied, calculated from the high-field gradient of the OOP curve of the no-Pt sample. This is the smallest diamagnetic background correction factor that will ensure that all the curves have non-negative gradients at high field. Small discontinuous jumps at zero field are a known artifact of the measurement system.

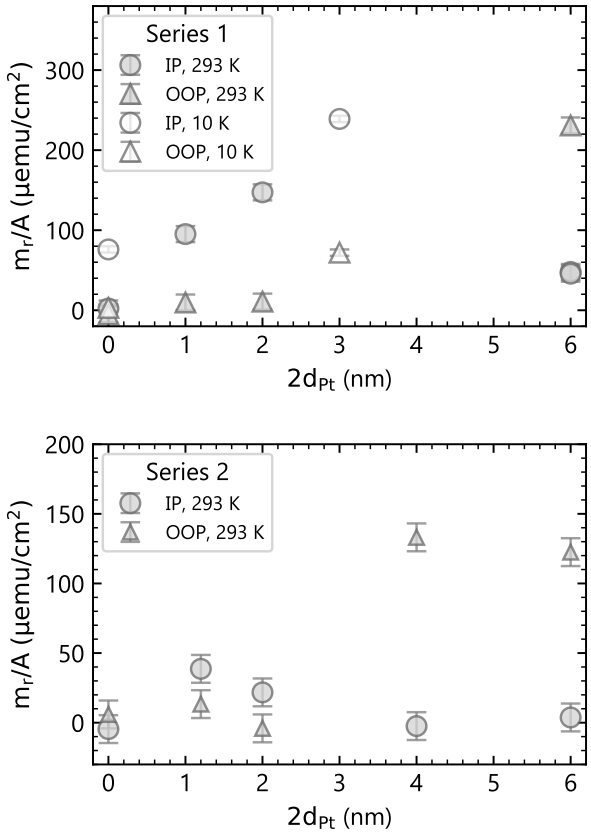


FIGURE 7.11: Remanent magnetization per unit area m_{r}/A from room temperature VSM measurements for a series of unpatterned Nb/Pt(d_{Pt})/Co(1.5)/Pt(d_{Pt})/Nb films. Top: Series 1 films. Bottom: Series 2 films.

In another series of films, the Co thickness d_{Co} was varied at constant Pt thickness, with the structure Nb/Pt(2)/Co(d_{Co})/Pt(2)/Nb. Room-temperature $M(H)$ loops are shown in Fig. 7.12, and the saturation magnetization m_s is plotted against d_{Co} in Fig. 7.13. The Co dead layer thickness is extracted as 0.6 nm from the intercept at zero magnetization, and the gradient of the straight line fit corresponds to (1009 ± 6) emu/cm^3 compared with 1422 emu/cm^3 [75]. The discrepancy can be attributed to film quality and interfacial effects, and the value measured here is very close to that reported by Robinson et al. [68].

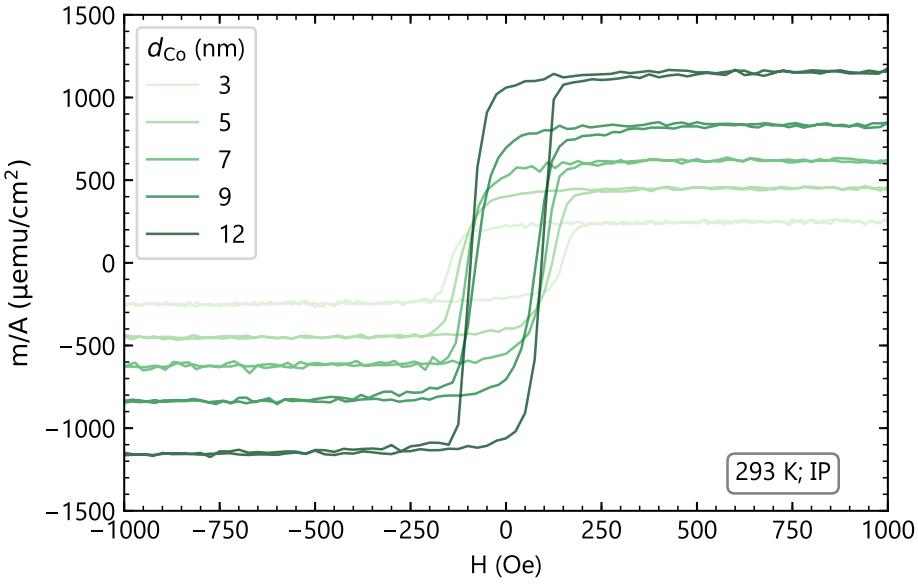


FIGURE 7.12: $M(H)$ loops for Nb/Pt(2)/Co(d_{Co})/Pt(2)/Nb unpatterned films at room temperature.

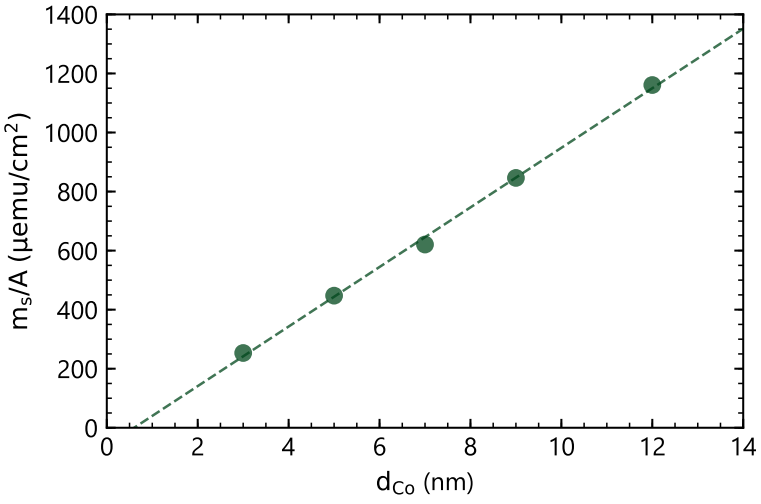


FIGURE 7.13: Saturation moment per unit area at 293 K plotted against Co thickness. The errors in the measured moment per unit area are smaller than the size of the data points.

7.3.2 Transport measurements

Measurements of the patterned nanopillar devices follow, commencing with the Series 1 Nb/Pt(d_{Pt})/Co(1.5)/Pt(d_{Pt})/Nb devices. The aim is to understand the dependence of supercurrent on the Pt thickness at a Co thickness where the singlet supercurrent is still measurable. The behaviour observed may not be trivial for two reasons. Firstly, the easy axis will vary from IP to OOP as Pt is added. Secondly, the total magnetic moment will increase as Pt is added due to proximity-induced magnetism. According to Rowan-Robinson et al. [12], proximity-induced magnetism in Pt decays after around 1 nm. So after $2d_{\mathrm{Pt}} = 2\,\mathrm{nm}$, we might expect this effect to saturate. The saturation magnetization data above show variations occurring up to around $2d_{\mathrm{Pt}} = 3\,\mathrm{nm}$, although due to the limited data and the changing magnetic anisotropy it is difficult to be precise about this. This means we might expect something resembling 0-π transitions for very thin Pt, although the short range would make this difficult to observe. Once this short range effect is saturated, we would expect the singlet component to decay exponentially with a constant given by the coherence length ξ_{Pt}.

Fig. 7.14 shows the I_cR_N dependence on Pt thickness. Adding thin Pt layers ($2d_{\mathrm{Pt}} = 1\,\mathrm{nm}$) leads to a steep drop in $I_{\mathrm{c}}R_{\mathrm{N}}$ and J_{c}. Increasing the thickness to $2d_{\mathrm{Pt}} = 2\,\mathrm{nm}$, rises in $I_{\mathrm{c}}R_{\mathrm{N}}$ and J_{c} are observed, although with so few data points it is difficult to have confidence in the reproducibility of this rise. This then decays gradually to close to zero at $2d_{\mathrm{Pt}} = 10\,\mathrm{nm}$. The data here are insufficient to claim that 0-π oscillations are being observed; more data at low Pt thicknesses would be desirable to investigate this.

AR_{N} is also plotted (Fig. 7.14) to confirm consistent device fabrication, and appears roughly constant with $2d_{\mathrm{Pt}}$ over this relatively small Pt thickness range.

Having explored the dependence on the Pt thickness, further series of films were deposited with varying Co thickness for $2d_{\mathrm{Pt}} = 2\,\mathrm{nm}$ and $2d_{\mathrm{Pt}} = 4\,\mathrm{nm}$. Fig. 7.15 shows the dependence of $I_{\mathrm{c}}R_{\mathrm{N}}$ on d_{Co} in Nb/Pt(d_{Pt})/Co(d_{Co})/Pt(d_{Pt})/Nb nanopillar junctions at 1.6 K. A supercurrent can be detected at a maximum thickness $d_{\mathrm{Co}} = 7\,\mathrm{nm}$. Also shown on the figure are data points from Robinson et al. [68] for Nb/Co/Nb devices without Pt, along with the fitted 0-π oscillation model given by:

$$I_{\mathrm{c}}R_{\mathrm{N}}(d_{\mathrm{F}}) \propto I_{\mathrm{c}}R_{\mathrm{N}}(d_0)\left|\frac{\sin\left(\frac{d_{\mathrm{F}}-d_1}{\xi_2}\right)}{\sin\left(\frac{d_1-d_0}{\xi_2}\right)}\right|\exp\left(\frac{d_0-d_{\mathrm{F}}}{\xi_1}\right), \tag{7.1}$$

where d_{F} is the the ferromagnetic thickness being varied, $I_{\mathrm{c}}R_{\mathrm{N}}(d_0)$ is an experimentally measured point at thickness d_0, d_1 is the thickness of the first zero, $\xi_1 = 3\,\mathrm{nm}$ is the decay length and $\xi_2 = 0.3\,\mathrm{nm}$ is the oscillation length, following the values reported by Robinson et al. [68].

We see that the present devices with Pt layers do not differ significantly in I_cR_N from the Nb/Co/Nb devices; while there are too few points to extract the decay behaviour accurately in the present data it appears to be similar. There is no evidence of the LRT generation that was the initial aim of investigating this device structure.

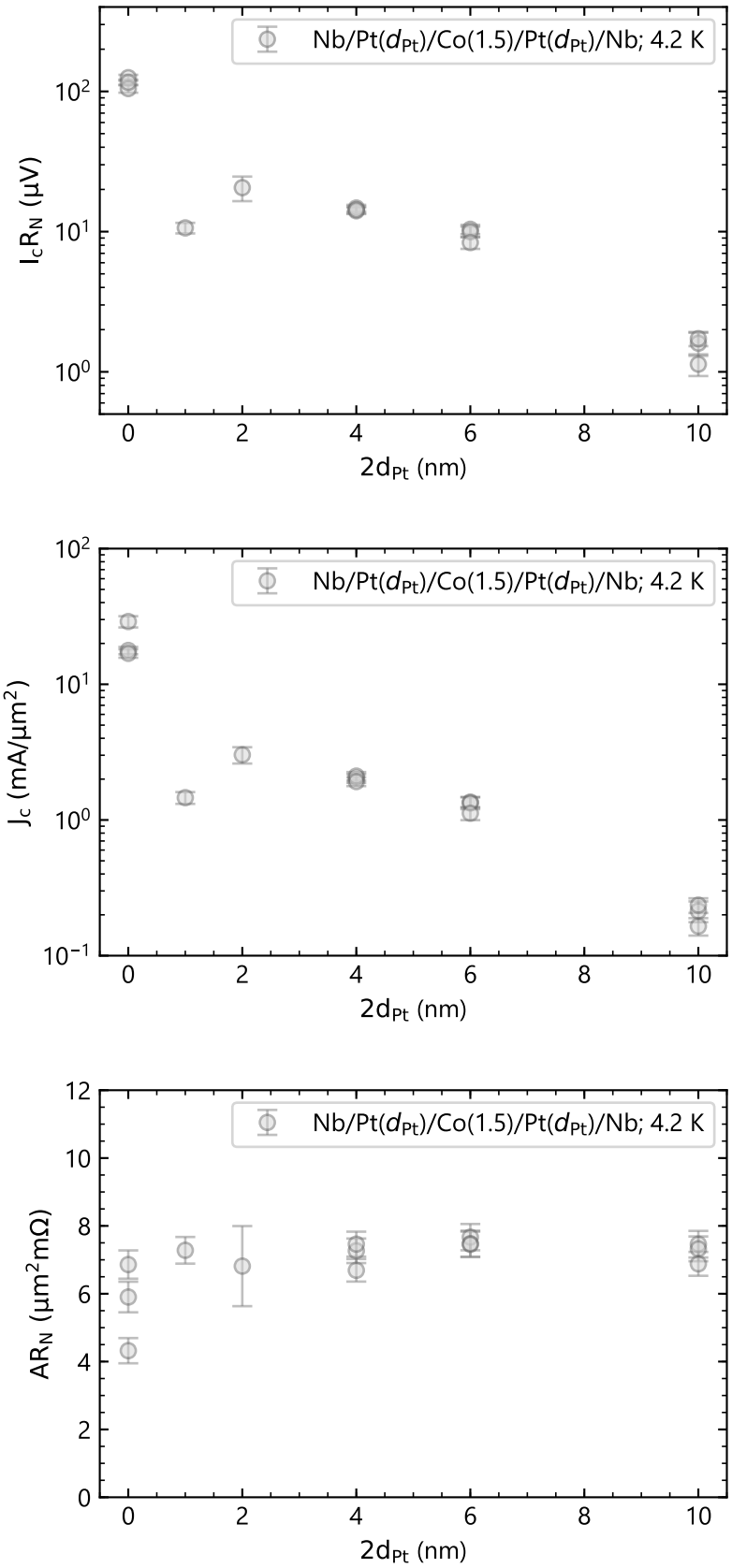


FIGURE 7.14: I_cR_N, J_c and AR_N measured for varying Pt thickness in Nb/Pt(d_{Pt})/Co(1.5)/Pt(d_{Pt})/Nb devices at 4.2 K.

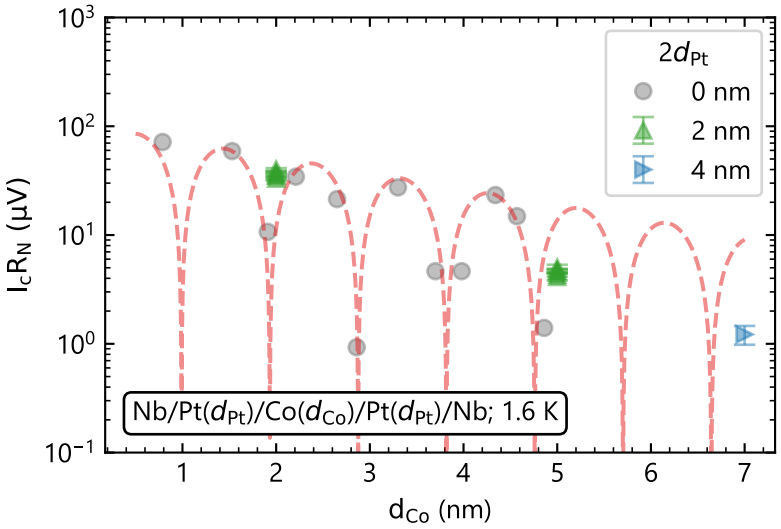


FIGURE 7.15: I_cR_N measured for a series of Nb/Pt(d_{Pt})/Co(d_{Co})/Pt(d_{Pt})/Nb devices (coloured triangles) at 1.6 K, compared with Nb/Co/Nb devices from Robinson et al. [68] (grey circles). The red dashed line is the 0-π model given by Equation 7.1.

The $I_c(H)$ dependence of the devices is fairly typical, with a more rapid periodicity than expected from the device dimensions, as seen elsewhere in the ferromagnetic junctions in this thesis. Fraunhofer patterns for the devices of differing $2d_{Pt}$ are shown in Fig. 7.16, while those with differing d_{Co} are shown in Fig. 7.17. We may define $\Delta H = \frac{1}{2}(H^+_{peak} - H^-_{peak})$, where H^+_{peak} (H^-_{peak}) is the applied field for which peak I_c is measured on the positive (negative) field sweep from initial saturation at 200 mT in the opposite direction, i.e. the applied field at which the internal flux is cancelled. ΔH is plotted against both varying Co thickness and varying Pt thickness in Fig. 7.18. We observe a linear dependence of ΔH on Co thickness. In the case of varying Pt thickness, we observe an initial increase as Pt is added, consistent with Pt increasing the magnetic moment. This remains relatively flat, except for the fall at $2d_{Pt} = 6$ nm. Again, more data are needed to understand this behaviour fully.

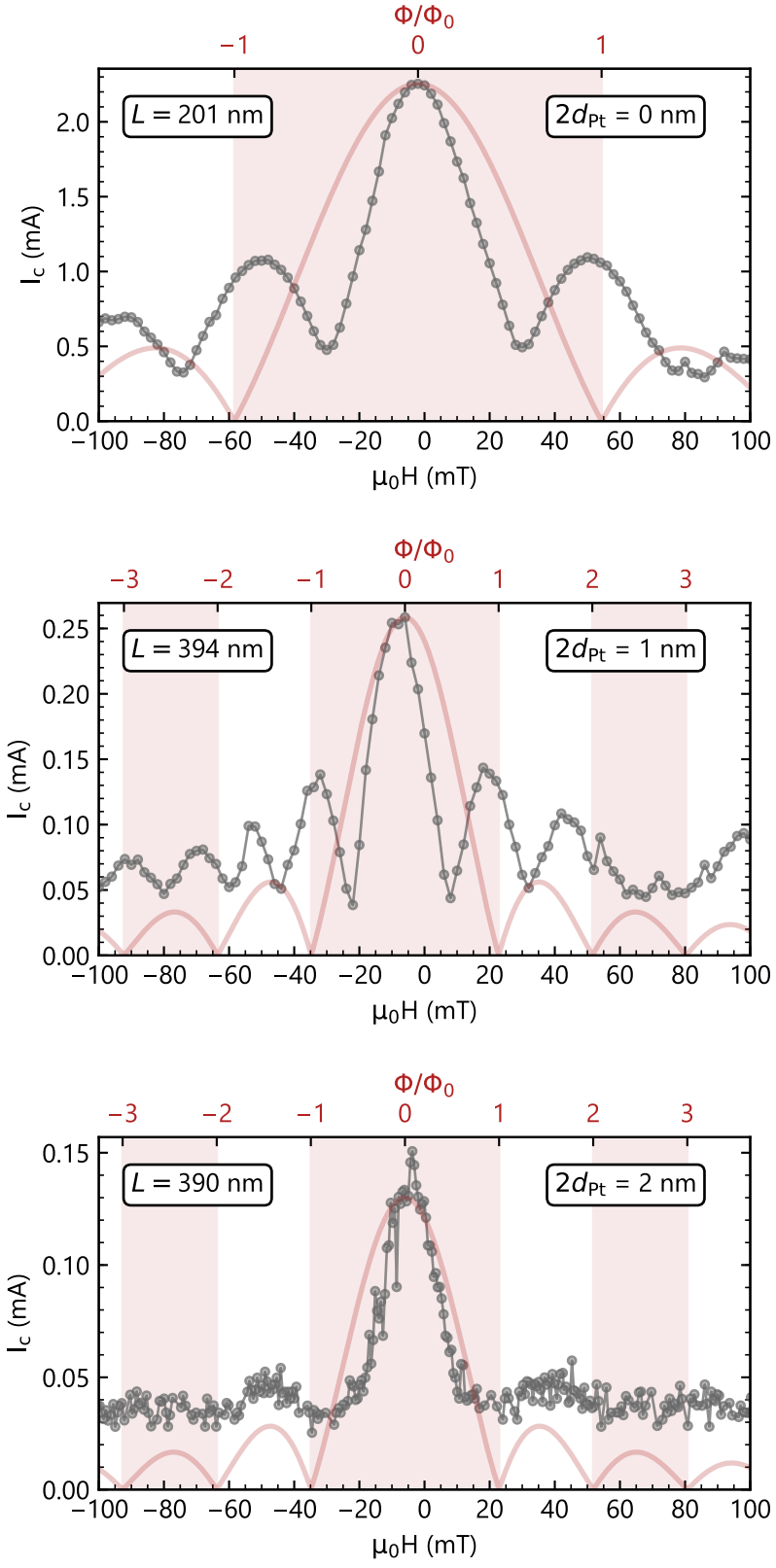


FIGURE 7.16: $I_c(H)$ dependence of Nb/Pt(d_{Pt})/Co(1.5)/Pt(d_{Pt})/Nb junctions at 4.2 K. Red shaded regions and curve represent the periodicity expected from the junction length L, and have been centred on the central maximum from the data. (Continues)

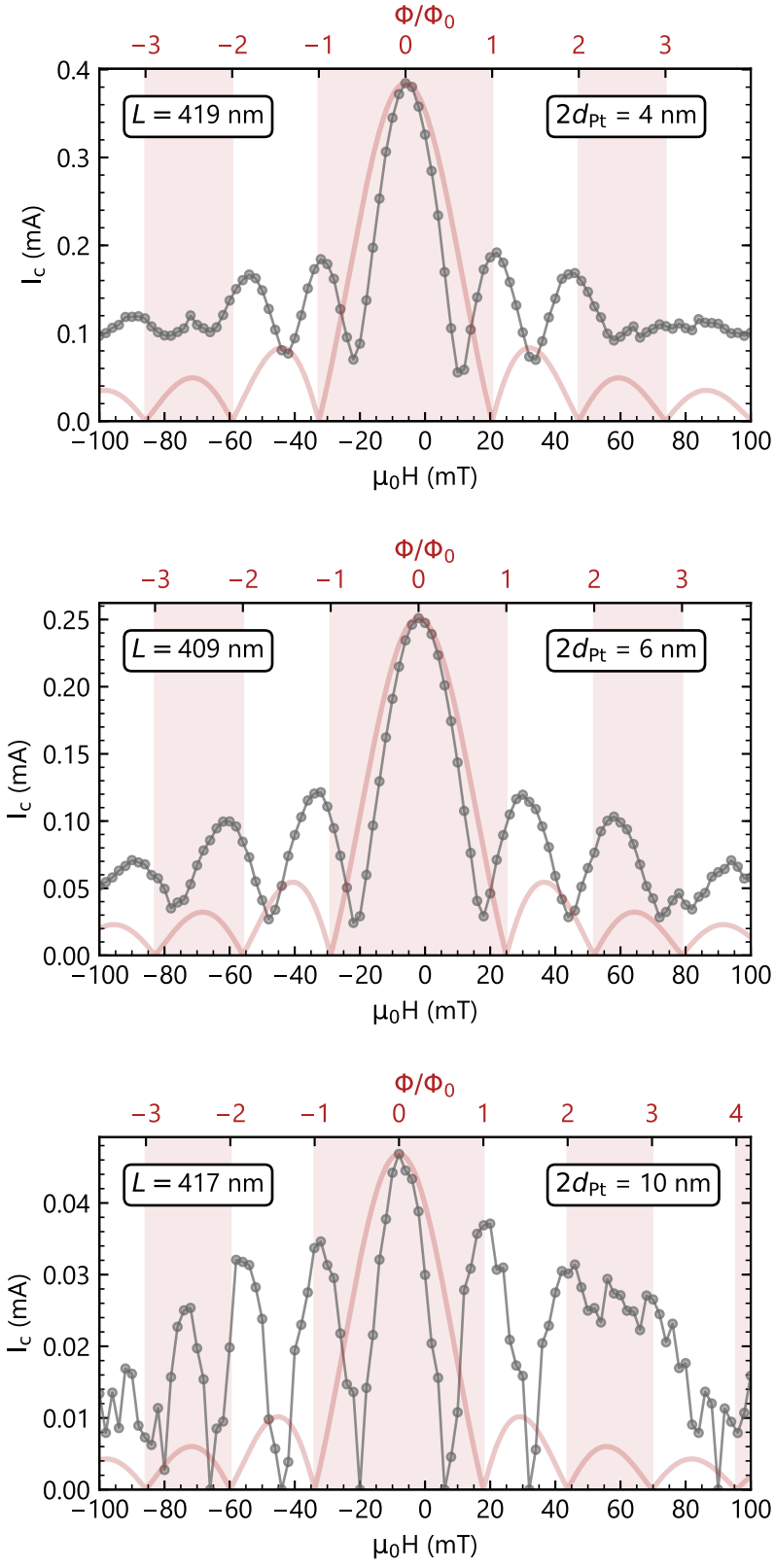


FIGURE 7.16: (Continued) $I_c(H)$ dependence of Nb/Pt(d_{Pt})/Co(1.5)/Pt(d_{Pt})/Nb junctions at 4.2 K. Red shaded regions and curve represent the periodicity expected from the junction length L, and have been centred on the central maximum from the data.

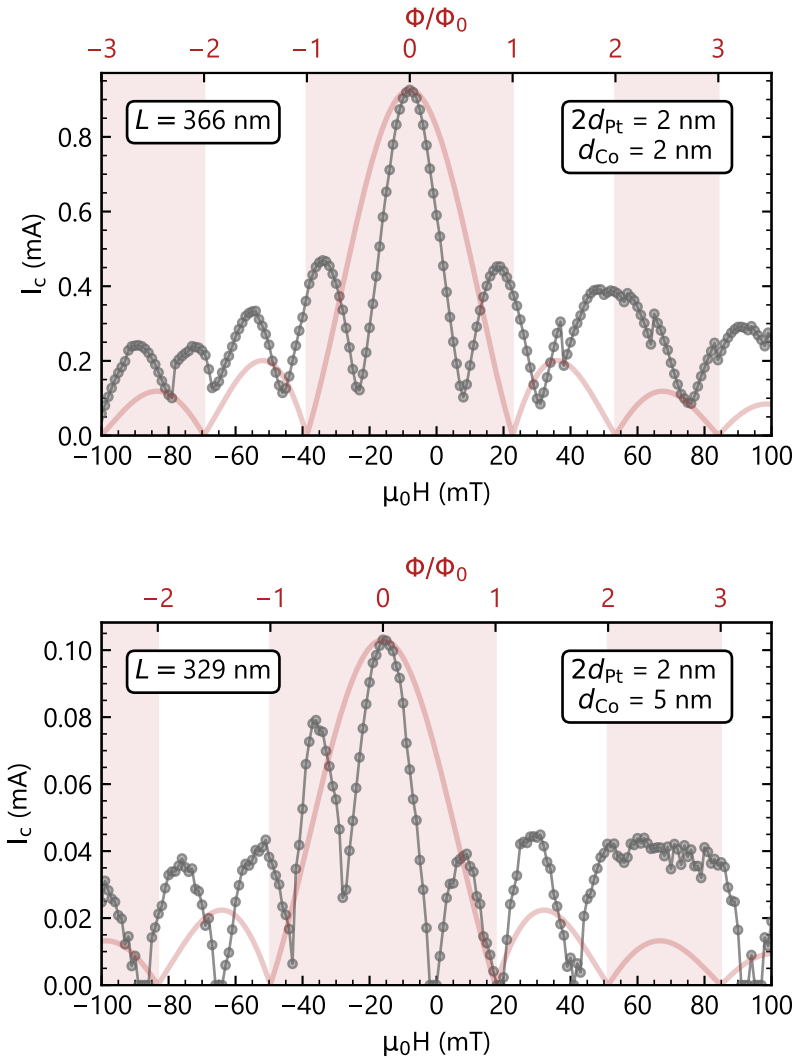


FIGURE 7.17: $I_c(H)$ dependence of Nb/Pt(2)/Co(d_{Co})/Pt(2)/Nb junctions at 1.6 K. Red shaded regions and curve represent the periodicity expected from the junction length L, and have been centred on the central maximum from the data.

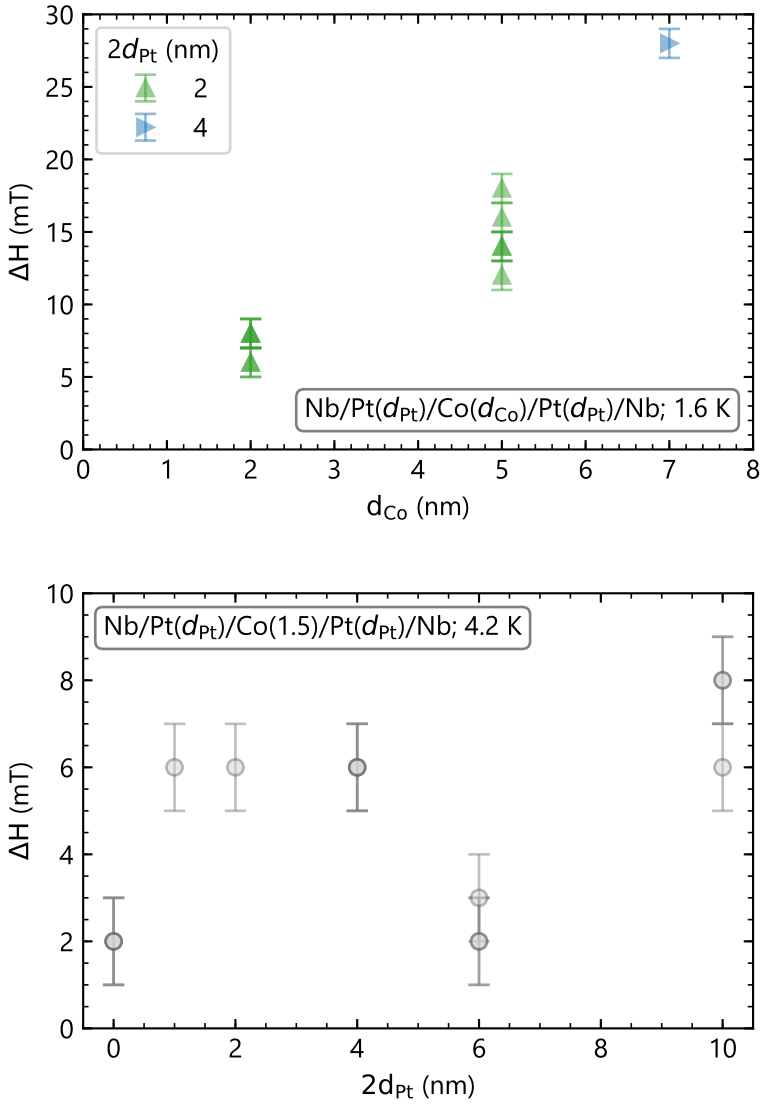


FIGURE 7.18: Top: ΔH dependence of Nb/Pt/Co(d_{Co})/Pt/Nb junctions on Co thickness at 1.6 K. Bottom: ΔH dependence of Nb/Pt(d_{Pt})/Co(1.5)/Pt(d_{Pt})/Nb junctions on Pt thickness at 4.2 K.

7.4 Conclusions

Simple Nb/Pt/Nb junctions were fabricated to confirm expected device behaviour and estimate the normal-metal coherence length of Pt as $\xi_{\mathrm{Pt}} = (24 \pm 2)\,\mathrm{nm}$. Then Nb/Pt/Nb/Pt/Nb structures were investigated to study singlet supercurrent propagation in S/N/S/N/S structures, serving as a useful control for many of the experiments in this thesis.

No long-ranged triplet supercurrent was observed in the Nb/Pt/Co/Pt/Nb junctions. During the course of this work, similar experiments were performed by Birge and Satchell [76] on Nb/Pt(0.5)/Co/Ru(0.6)/Co/Pt(0.5)/Nb Josephson junctions. They found that although the incorporation of Pt increased the $I_{\mathrm{c}}R_{\mathrm{N}}$ product (attributed to Pt altering the film growth), the decay length was unchanged. They concluded that this was due to a lack of out-of-plane anisotropy in their devices. The devices are much larger than those in this thesis; they fabricate circular junctions of diameter between 12 µm and 48 µm, so the magnetostatic behaviour is expected to be rather different. Guided by the theoretical requirement of generating a significant out-of-plane magnetic anisotropy, they then attempted to observe LRTs in Nb/[Co(0.4)/Ni(0.4)]×8 /Co(0.4)/Nb junctions [77], where such anisotropy arises in the Co/Ni superlattice. Again, there was no evidence of LRT generation.

The reasons for the elusiveness of LRTs generated via SOC are unclear. It may be that the conversion efficiency achieved in these experiments is too small. Jacobsen et al. [59] note that interface roughness needs to be minimized. It might be that the lateral geometry remains the better approach due to the looser set of conditions required for LRT generation.

Chapter 8

Josephson junctions with strong spin-orbit coupling and superconducting interlayers

The previous chapters have explored Cr/Fe and Pt/Co interfaces as potential spin-mixers, and structures with superconducting interlayers. A major aim of this thesis is to study the propagation of long-ranged triplet correlations within intermediate superconductors, with a view to eventual logic circuits carrying spin in the superconducting state.

This chapter presents equilibrium Josephson junction experiments analogous to the non-equilibrium experiments of Jeon et al. 2.3.6. In their FMR experiments, the spectrum linewidth is a measure of the Gilbert damping. The flow of spin angular momentum from a ferromagnet into an adjacent material increases the Gilbert damping, and therefore the measured linewidth. Above T_c, Nb/Py/Nb trilayers show an increased linewidth compared with Py alone due to spin absorption in the Nb. For a given trilayer, the linewidth decreases as the temperature is lowered below T_c, as the opening of the superconducting gap blocks spin transport. When Pt layers (5 nm thick) are added symmetrically about the trilayer, the behaviour is dramatically different, showing an increase of linewidth below T_c compared to that above T_c. This effect is only observed for Nb thicknesses shorter than the coherence length, and is at its strongest around 30 nm. Hence spin transport is now enhanced, rather than inhibited in the superconducting state.

The mechanism proposed by Jeon et al. [7] is an induced triplet pairing state, arising due to the strong SOC of Pt, and the likely spin splitting of Pt due to its high spin susceptibility. Explanations involving a static magnetic inhomogeneity at the interface and the precession of interface magnetization were rejected, on the basis that the magnetic layer was expected to be homogeneous.

The work of this chapter aims to elucidate more about the origin of the triplet component in the FMR work and attempts to recreate this in equilibrium Josephson junctions for use in spintronic devices. I explore the device structures Nb/Cr/Fe/Nb/Pt/Nb and Nb/Pt/Nb/Py/Nb/Pt/Nb. The first of these combines a Cr/Fe spin-glass interface as discussed in Chapter 5 with a thin Pt layer, separated

by a Nb interlayer. The presence of a magnetic exchange field from Fe, in combination with the Rashba spin-orbit field arising due to Pt, should generate a triplet component. The second structure is a direct analogue of that used in the experiment of Jeon et al. We now consider the proposed mechanism from the FMR experiment to predict what might be seen in these equilibrium Josephson junction devices. In both of these structures, we hypothesise that LRT generation would be observed when the Pt is sufficiently close to the spin-mixer interface, with the effect decaying on the length scale of the Nb coherence length. However, as the interlayer is made thinner, the suppression of the superconducting order parameter may diminish the critical current, as seen in the Nb/Pt/Nb/Pt/Nb devices of Chapter 7. If the ferromagnet is made sufficiently thick, the singlet component should be suppressed entirely, and so only the triplet component would be measured, decaying on the length scale of the Nb coherence length. If the ferromagnet is thin and some singlet contribution remains, we may see a non-monotonic dependence of the critical current with interlayer thickness; an initial rise due to the increasing singlet contribution, followed by a decrease as the triplet component diminishes.

The device fabrication and measurements in this chapter are the sole work of the author.

8.1 Nb/Cr/Fe/Nb/Pt/Nb junctions

In this device structure, it is hypothesized that the central superconducting Nb interlayer may be able to support a triplet supercurrent generated at a Cr/Fe interface, due to the Pt layer 'opening' a triplet channel. Nb interlayer thicknesses from 0-67 nm were studied. Fig. 8.1 shows the variation of I_cR_N, J_c and AR_N with interlayer thickness. I_cR_N and J_c show an initial increase (from zero when the Pt directly abuts the ferromagnet), with increasing $d_{Nb'}$, before plateauing roughly around the coherence length of Nb (39 nm). This behaviour is consistent with two singlet Josephson junctions in series, as in Chapter 7 with Nb/Pt/Nb/Pt/Nb devices. For $d_{Nb'} \gg \xi$, we simply have a single asymmetric Cr/Fe barrier, with the 4.4 nm thick Pt having little effect on the device behaviour (the critical current of a 4.4 nm thick Pt Josephson barrier is much greater than that for 3.7 nm Fe). With no interlayer and Pt adjacent to Fe, the critical current is zero. This may be rationalized by the proximity-induced magnetization of Pt discussed in Subsection 1.1.4, which offers a greater effective ferromagnetic thickness to the singlet supercurrent. In the intermediate range of $d_{Nb'}$, the increasing Nb thickness supports an increasing singlet supercurrent.

At 3.7 nm Fe, the singlet is moderately suppressed but still measurable. The non-monotonic dependence due to the interplay of singlet and triplet contributions hypothesized in the introduction is not seen, and the behaviour here can be explained purely in terms of a singlet supercurrent.

Also plotted are control data with Cu replacing the Pt layer. This shows a similar dependence, providing further confirmation that the hypothesized influence of the

SOC of Pt does not play a role in determining the device behaviour. One contrasting feature is that with Cu, devices with no interlayer have a measurable critical current. This is consistent with the assumption that proximity induced magnetization occurs in Pt but not in Cu, with the additional magnetization in the former case suppressing the singlet supercurrent below measurable levels.

AR_N stays roughly constant with increasing $d_{Nb'}$ (although there is considerable scatter), as may be expected, since the superconducting Nb does not contribute to R_N. Further, it can be inferred from this that the currents applied here are not large enough to drive the interlayers themselves into the normal state.

Devices with varying ferromagnetic thickness d_{Fe} were fabricated, to estimate the decay length. The results are shown in Fig. 8.2, and show a rapid decay with length $\xi_{Fe} = 0.6\,\text{nm}$, consistent with a singlet supercurrent.

Fraunhofer patterns for the devices are plotted in Fig. 8.3. The behaviour is similar to other singlet ferromagnetic junctions in this thesis, with a reduced primary lobe width and higher than expected current in the subsidiary lobes.

The temperature dependence of the devices are shown in Fig. 8.4. The temperature at which I_c reaches zero increases with increasing $d_{Nb'}$, as might be expected. The decay of $I_c(T)$ is much steeper for the thinnest interlayer. $R(T)$ curves are similar for all devices, with the no-interlayer $R(T)$ showing a small resistance at base temperature, indicating that full proximitization is not attained.

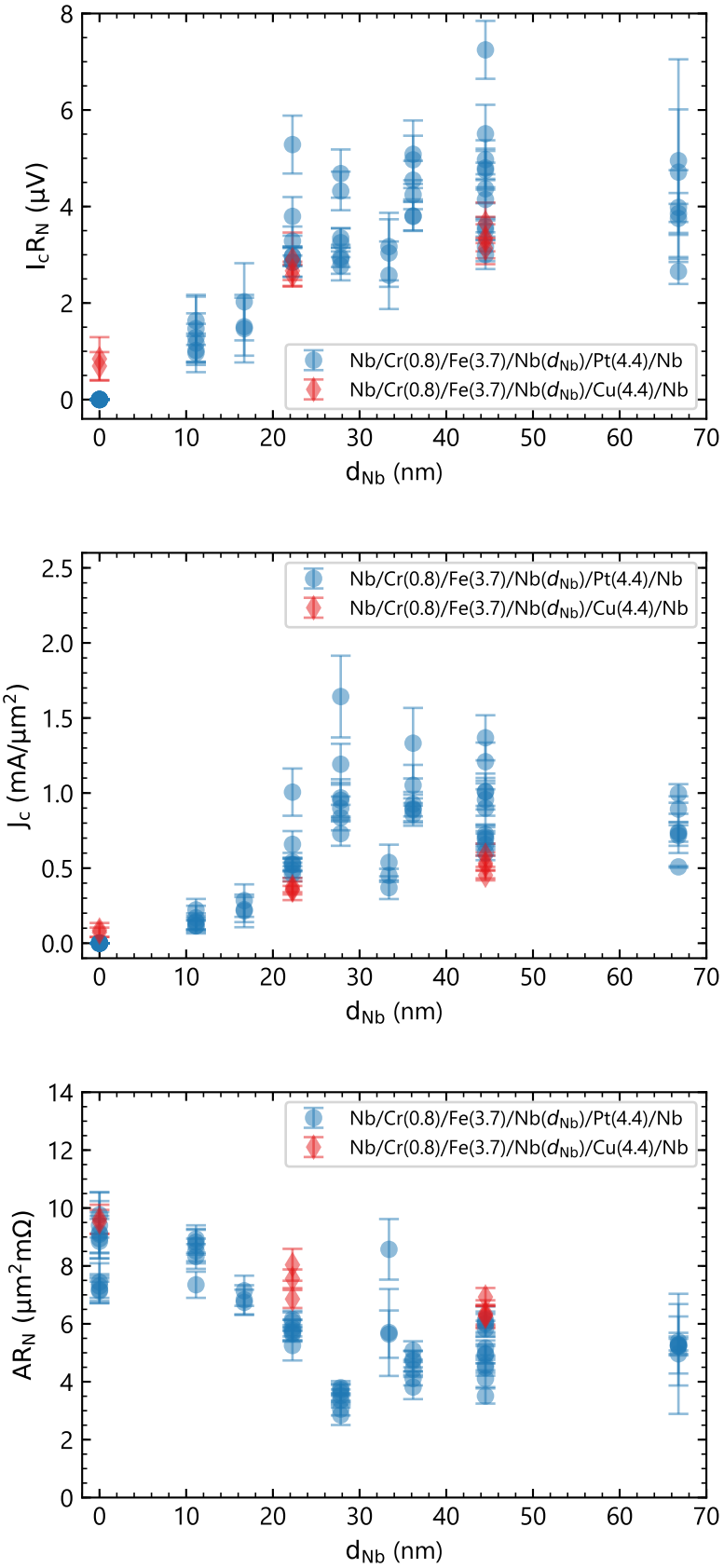


FIGURE 8.1: I_cR_N, J_c and AR_N measured for varying Nb thickness in Nb/Cr(0.8)/Fe(3.7)/Nb($d_{Nb'}$)/Pt(4.4)/Nb devices at 1.6 K.

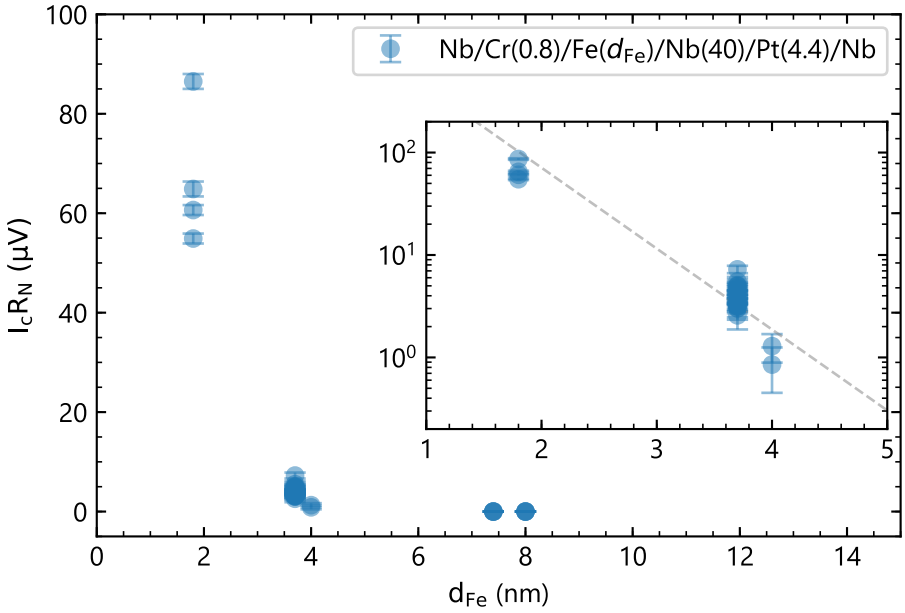


FIGURE 8.2: I_cR_N measured for varying Fe thickness in Nb/Cr(0.8)/Fe(d_{Fe})/Nb(40)/Pt(4.4)/Nb devices at 1.6 K. The inset shows the non-zero values of I_cR_N on a log-scale, with a fitted decay corresponding to ξ_{Fe} around 0.6 nm.

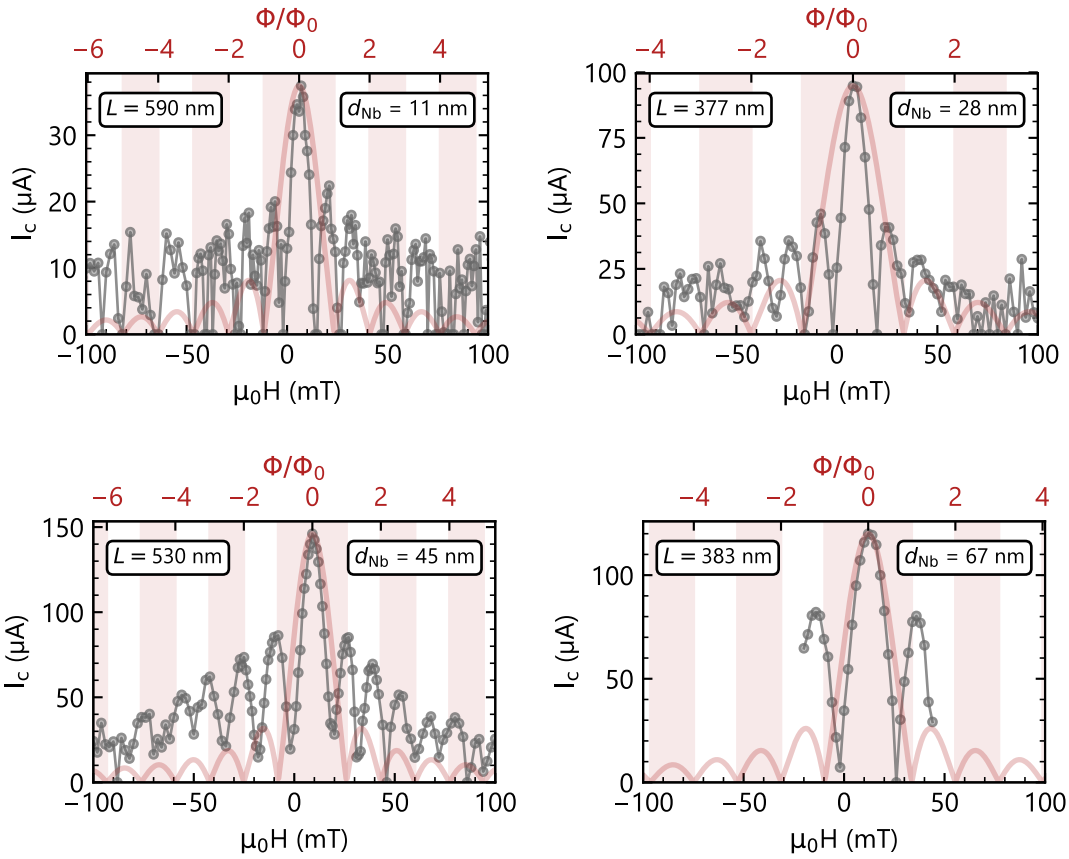


FIGURE 8.3: $I_c(H)$ dependence of Nb/Cr(0.8)/Fe(3.7)/Nb($d_{Nb'}$)/Pt(4.4)/Nb junctions at 1.6 K. Red shaded regions and curve represent the periodicity expected from the junction length L, and have been centred on the central maximum from the data.

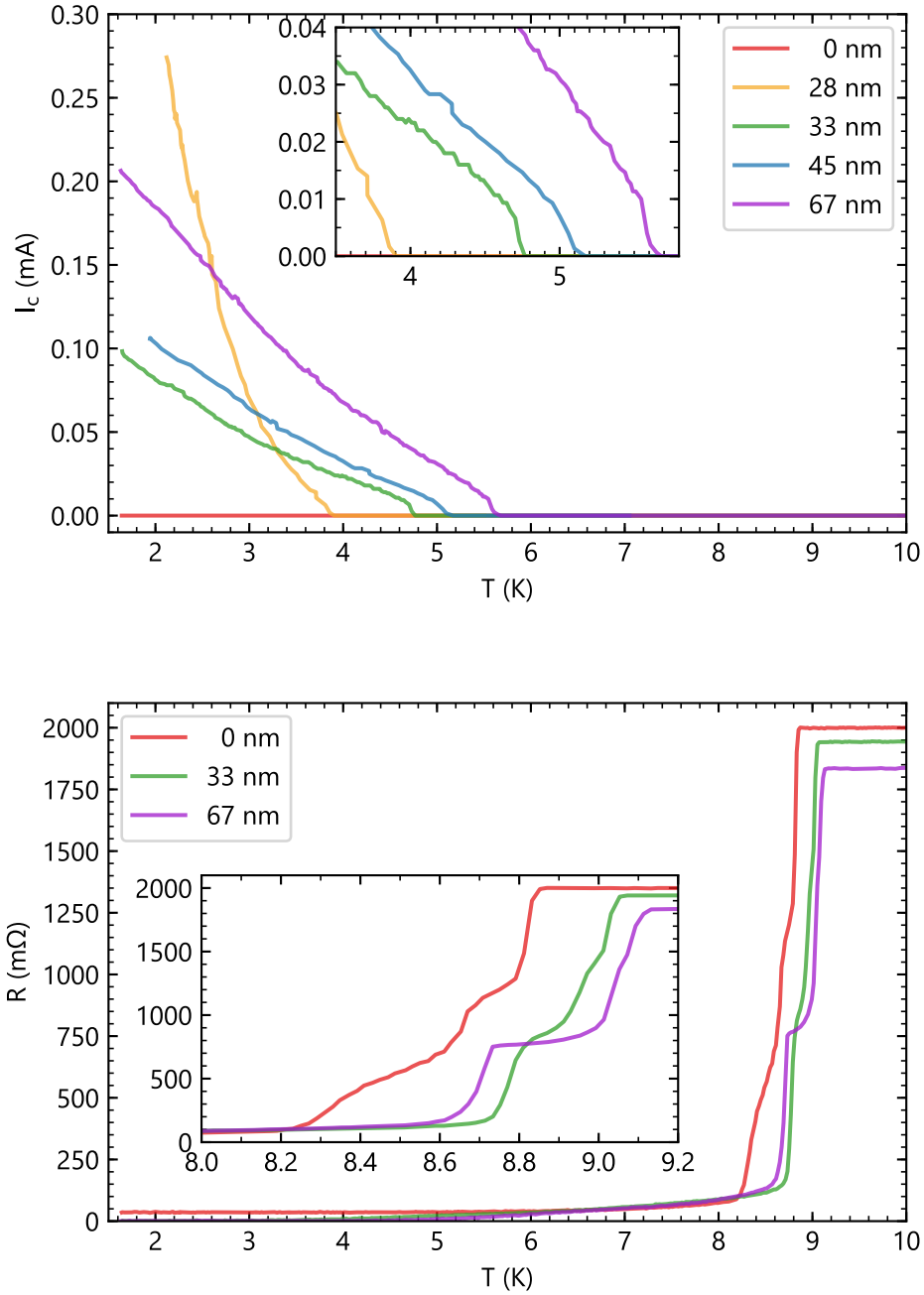


FIGURE 8.4: Top: $I_c(T)$ for Nb/Cr(0.8)/Fe(3.7)/Nb($d_{Nb'}$)/Pt(4.4)/Nb devices. Bottom: $R(T)$ curves for a subset of these devices.

8.2 Nb/Pt/Nb/Py/Nb/Pt/Nb junctions

The Nb/Pt(4.4)/Nb($d_{Nb'}$)/Py(4)/Nb($d_{Nb'}$)/Pt(4.4)/Nb structure is a direct copy of that used in the FMR experiments of Jeon et al. [7]. A thickness of 4 nm Py is chosen to suppress the singlet component moderately, such that a superposition of singlet and triplet supercurrents would be observed. As discussed in the introduction to this chapter, we are looking for a peak in critical current around the coherence length of Nb as a signature of the Pt layers inducing triplet transport.

In these devices, the junction size was varied significantly, from 0.05 µm^2 to 0.40 µm^2. As discussed in Chapter 4, size is known to affect I_cR_N. Fig. 8.5 shows the size dependence for these devices. As for the Nb/Py/Nb devices in Chapter 4, I_cR_N decreases with increasing area in a non-linear fashion, most clearly exhibited by the data for $d_{Nb'} = 80$ nm.

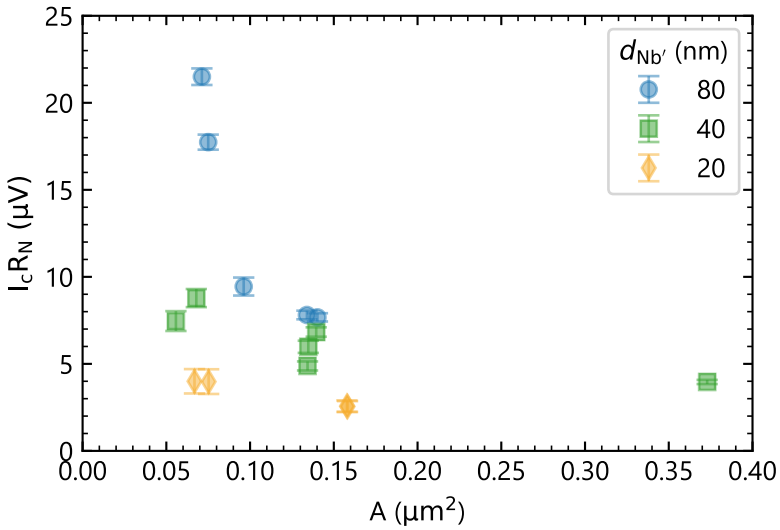


FIGURE 8.5: Area dependence of I_cR_N for Nb/Pt(4.4)/Nb($d_{Nb'}$)/Py(4)/Nb($d_{Nb'}$)/Pt(4.4)/Nb devices at 1.6 K, for $d_{Nb'}$ = 20 nm, 40 nm and 80 nm.

Informed by this size dependence, the devices are divided into two groups for the purposes of plotting the data: those of area < 0.08 µm^2 (small junctions) and those with area > 0.08 µm^2 (large junctions). I_cR_N, J_c and AR_N are plotted for a symmetric variation of the two Nb interlayers in Fig. 8.6, for interlayers from 0 nm to 80 nm (much greater than the coherence length). I_cR_N and J_c increase monotonically, consistent with the behaviour expected from a singlet supercurrent. Once again, we conclude that the hypothesized triplet generation via the SOC of Pt does not operate in these devices. As observed with the Nb/Cr/Fe/Nb/Pt/Nb devices, the critical current falls to zero when the interlayer thickness is reduced to zero. This is due to both the increased thickness of contiguous non-superconducting layers, and the proximity-induced magnetism of Pt at the interface with a ferromagnet.

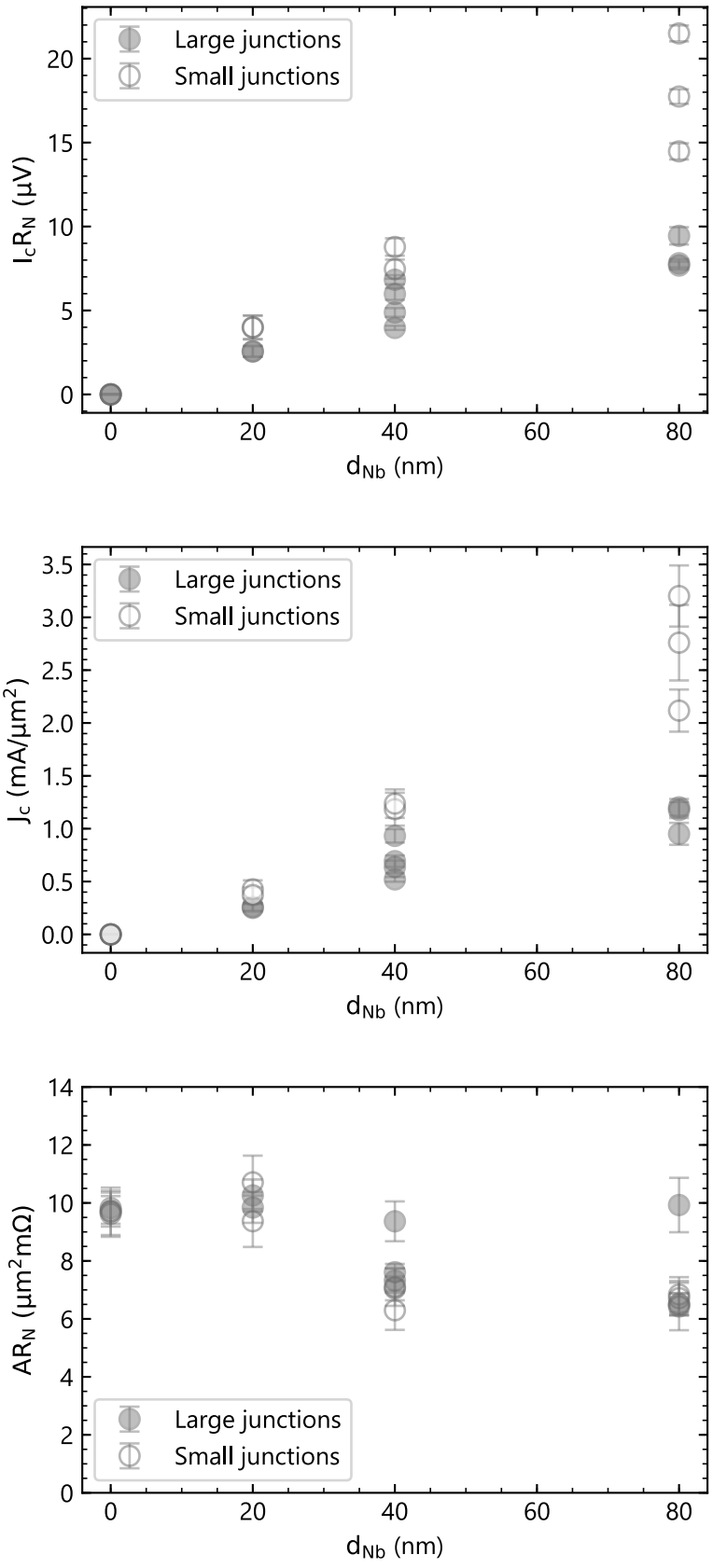


FIGURE 8.6: I_cR_N, J_c and AR_N measured for varying Nb thickness in Nb/Pt(4.4)/Nb($d_{Nb'}$)/Py(4)/Nb($d_{Nb'}$)/Pt(4.4)/Nb devices at 1.6 K.

The temperature dependence of the devices are shown in Fig. 8.7. The temperature at which I_c reaches zero increases with increasing $d_{Nb'}$, as with the devices with Cr/Fe/Nb/Pt barriers. $R(T)$ curves show that the devices with no interlayer do not fully proximitize, while the devices with $d_{Nb'}$ = 20 nm proximitize at lower temperature than the thicker interlayers, exhibited by the lower shoulder at around 8.7 K, and zero resistance not being attained until less than 2 K.

The $I_c(H)$ dependence of one of the devices is shown in Fig. 8.8. It is very difficult to model the flux penetration within the barrier with superconducting interlayers. Here, the effective thickness was chosen to be 184 nm in all cases (the thickness of the central ferromagnet plus twice the London penetration depth for thin-film Nb). The periodicity match to the measured patterns is fairly close nonetheless, at least in the context of other ferromagnetic Josephson junctions in this thesis. The size dependence is also clear; the two plots in Fig. 8.8 are from the same nanopillar with a high aspect ratio, measured with the field in two perpendicular orientations. These junctions commonly had sudden jumps in $I_c(H)$, perhaps associated with sudden changes in magnetization or phase slips. This can be observed in the left panel of Fig. 8.8 around +20 mT.

The hysteresis shift ΔH was noted to be higher for lower aspect ratios; i.e. applying magnetic flux through the short side of the junction. This can be seen in Table 8.1 and Fig. 8.9. This is likely to be the result of shape anisotropy, and follows what was observed for simple Nb/Py/Nb junctions in Chapter 4, where this effect is discussed in more detail.

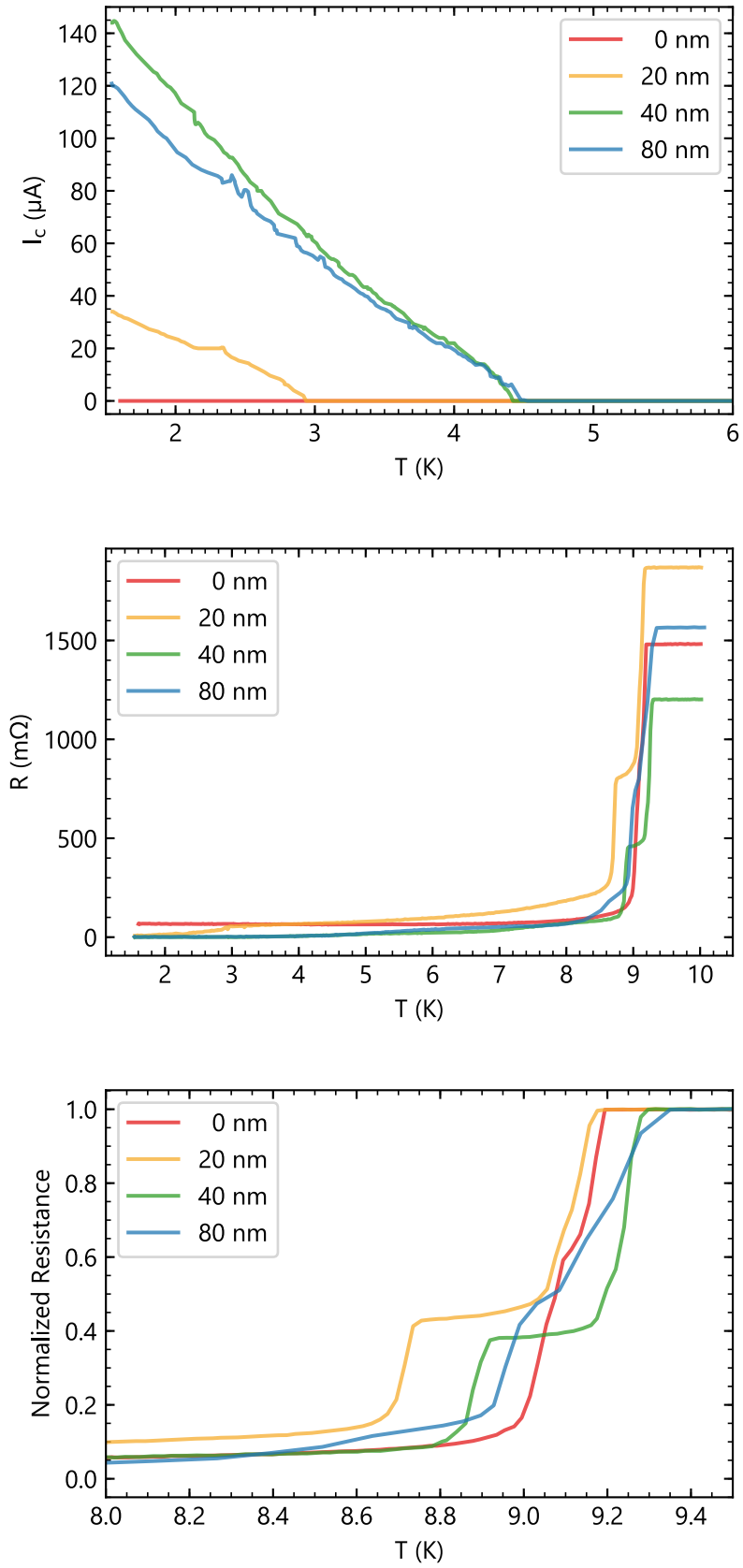


FIGURE 8.7: $I_c(T)$ and $R(T)$ for Nb/Pt(4.4)/Nb($d_{Nb'}$)/Py(4)/Nb($d_{Nb'}$)/Pt(4.4)/Nb devices. The lower plot shows the $R(T)$ data normalized by the value of each curve at 10 K.

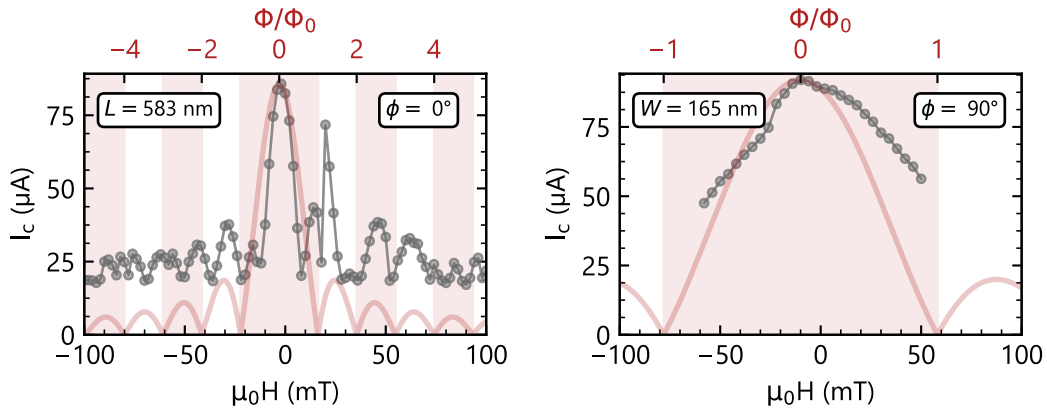


FIGURE 8.8: Fraunhofer patterns for one of the Nb/Pt(4.4)/Nb(80)/Py(4)/Nb(80)/Pt(4.4)/Nb devices, measured at $\phi = 0°$ (left) and $\phi = 90°$ (right). The red shaded regions, top axis and red model pattern are calculated from the device dimensions and show the expected periodicity. The grey points are the measured data, with the grey line joining subsequent measurements as a guide to the eye.

TABLE 8.1: Hysteresis shift ΔH in Fraunhofer patterns for three representative Nb/Pt(4.4)/Nb($d_{Nb'}$)/Py(4)/Nb($d_{Nb'}$)/Pt(4.4)/Nb devices measured at $\phi = 0°$ and $\phi = 90°$.

$d_{Nb'}$	L (nm)	W (nm)	$\Delta H_{\phi=0°}$ (mT)	$\Delta H_{\phi=90°}$ (mT)
80	120	625	10	8
80	583	165	3	10
40	621	217	0	12

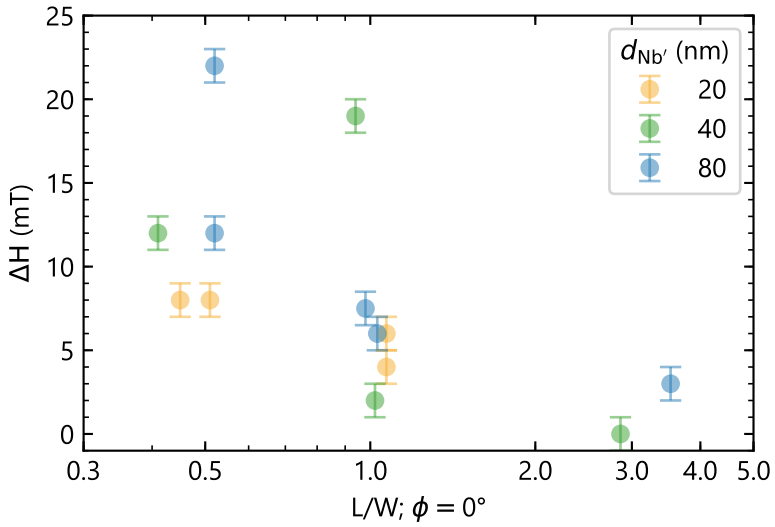


FIGURE 8.9: ΔH variation with aspect ratio L/W for measurements with applied field at $\phi = 0°$ at each interlayer thickness $d_{Nb'}$.

8.3 Conclusions

The experiments in this chapter aimed to generate a triplet channel in an intermediary superconducting layer through the combination of a spin-orbit coupling and an exchange field, after the FMR experiments of Jeon et al. Two device structures were investigated: Nb/Cr/Fe/Nb/Pt/Nb, combining the Cr/Fe spin-mixer with the Pt SOC, and Nb/Pt/Nb/Py/Nb/Pt/Nb, with no spin-mixer interface but providing a replication of the structure in the FMR experiments. At the outset, the thicknesses of ferromagnetic layers were chosen to suppress the singlet current moderately but not completely. In this case, it was hypothesized that a non-monotonic dependence of the critical current on interlayer thickness would be seen, with a maximum around the coherence length of Nb. In both of the device structures in this chapter, a simple monotonic increase was observed as the interlayer thickness was increased, consistent double-junction behaviour for purely singlet supercurrents. Increasing the ferromagnet thickness in the Nb/Cr/Fe/Nb/Pt/Nb beyond 4 nm suppressed the supercurrent below the limit of detection, providing a further indication that there was no significant triplet generation.

Putting this back into the context of the results of Jeon et al., it seems that the dynamic generation of a triplet channel in a non-equilibrium FMR experiment cannot be replicated in an equilibrium Josephson junction experiment.

Jeon et al. assumed that no triplet channel was present without Pt present. However, their results only provide evidence of the absorption of spin, rather than the initial generation of spin polarisation. An alternative explanation of their results is that there may be a triplet channel below T_c already present due to a mechanism not involving SOC. Adding Pt then merely allows for the absorption of this spin. The alternative mechanism for generating the spin triplet channel may rely on the FMR process itself. While interface inhomogeneity was rejected as an explanation by Jeon et al., it may well be present. The multilayers were sputtered, and so interface roughness will play a role. FMR excitation may precess these misaligned interfacial moments, rather than a spatially uniform magnetization precessing throughout the entire ferromagnet. If this is the case, then the lack of triplet generation in the equilibrium experiments here is unsurprising. Further work needs to be carried out to establish the precise mechanism by which the equal-spin triplet correlations are generated.

Chapter 9

Summary and future works

9.1 Overview

In this thesis I have presented experimental results from attempts to generate long-ranged triplet correlations via magnetically inhomogeneous interfaces and spin-orbit coupling. In addition, the research explored the propagation of singlet and triplet Cooper pairs through intermediary superconducting layers. Spin-aligned triplet generation and propagation through ferromagnets was first seen a decade ago, providing impetus to work towards superconducting circuits utilizing such pairing correlations as a basis for logic and memory. Spin propagation through intermediate superconductors is a crucial process to understand for the design of spintronic devices.

Attempts to reliably generate spin-aligned triplet supercurrents provided mixed results. The Cr/Fe spin-mixer interface initially thought to be the most convenient gave only hints of a long-ranged triplet having been generated, with poor reproducibility. Given the inherent randomness of the spin glass, the interface is very difficult to engineer through the deposition parameters, and the conversion efficiency is limited. The attempts to generate long-ranged triplets through the combination of spin-orbit coupling and an exchange field showed no signs of success at all. Similar recent results from other groups show that this remains elusive. The most reliable method of generating long-ranged triplets to date seems to be the use of multiple ferromagnetic layers with misaligned magnetizations, as in the work of Birge et al., although such structures still pose numerous experimental challenges.

The second major aim of this thesis was the study of spin-aligned triplet correlations in intermediate superconductors; i.e. the propagation of spin polarization in an ordinary spin singlet, s-wave superconductor. The most interesting results on this subject came from Nb/Cr/Fe/Nb/Fe/Cr/Nb double Josephson junction devices. While doubts remain about the triplet generation with Cr/Fe interfaces, we observed markedly different behaviour in devices with relatively thick Fe compared with those with thinner Fe; behaviour that could not be trivially explained in terms of spin-singlet supercurrents. If we assume that the behaviour is due to spin-aligned triplets, we would conclude that spin-aligned triplets decay quickly in thin non-superconducting Nb, and cannot be recovered by making the Nb interlayer thick enough to support a superconducting order parameter once more. This result is perhaps disappointing

if one hopes for devices in which spin polarization can be propagated over long distances in superconductors, however it may alternatively provide a mechanism for superconducting filtering of triplet states. The last experimental chapter of this thesis sought to study spin propagation through intermediate superconductors supported by strong spin-orbit coupling from Pt, after the FMR experiment of Jeon et al. showing enhancement of spin transport in similar structures. My results here showed no signature of triplet generation. Future work should aim to understand the mechanism underlying the results of the FMR experiment to establish whether the non-equilibrium dynamics are a requirement to observe the enhanced spin transport.

Before turning to the outcomes and recommended future work arising from each chapter, I will discuss some general points which affect the interpretation of all of the results in the thesis.

Depositing thin layers on top of relatively rough, 300 nm thick Nb electrodes leads to a 'snow-capped mountain range' morphology rather than the idealized flat interfaces drawn in schematics. Along with the sensitivity to deposition parameters, this leads to various complications in the micromagnetic state and makes interfaces difficult to control and reproduce. While interfacial roughness is known to weaken perpendicular magnetic anisotropy, an out-of-plane easy axis was observed nonetheless here in Pt/Co/Pt trilayers. However, roughness has been indicated as a potential issue for the generation of an LRT through SOC. While methods such as interrupting the growth of Nb with Cu have been known to decrease the roughness, this can cause additional complications in the device behaviour and so were not used here. Detailed structural characterizations of the interfaces in this type of device with thick Nb electrodes would benefit future research.

All magnetometry measurements were limited to the bulk unpatterned films, since magnetic characterisation of the fabricated nanopillars would not be possible. Micromagnetic modelling may provide a way to obtain semi-quantitative predictions about the magnetic behaviour in the nanopillars. Further characterization of the unpatterned films may be performed, for example neutron diffraction and X-ray magnetic circular dichroism. This would aid in understanding the complex magnetic behaviour arising in multilayer films.

Modelling the Fraunhofer patterns accurately has not been possible in this work. The sensitivity of the patterns to the ferromagnetic layers makes this challenging, as does the complex flux penetration arising when there are double or triple barrier junctions of small lateral extent with intermediary superconductors. Furthermore, there may be self-field effects and flux penetration. Again, more complex models could be developed to deal with these devices.

9.2 Summary of experimental chapters

Chapter 4: Varying the aspect ratio does not have an appreciable effect on the critical current density or $I_c R_N$ product, however increasing the junction area causes a

monotonic decrease in both of these. The reasons were not entirely clear, although a spatially non-uniform current distribution seemed likely. A more in-depth study of this area dependence, with sufficient data to derive a likely functional relationship on the dimensions, would provide a useful reference for experiments based on ferromagnetic nanopillar Josephson junctions.

Chapter 5: The generation of LRTs by Cr/Fe spin glass interfaces was attempted, with mixed results. We were able to detect a supercurrent at up to 12 nm Fe at 1.6 K in the case that Cr/Fe interfaces were present compared to less than 6 nm Fe without, although the number of successful devices was too small to claim that a longer decay length had been achieved with confidence. While these interfaces have advantages in that only a small number of layers is required to generate magnetic inhomogeneity, the disadvantage of this system is the poor degree of control of the magnetic structure. Assuming randomized spins at the two Cr/Fe interfaces, the pair-conversion efficiency is around 40% of the ideal case of the Houzet-Buzdin model. Better characterisation of the magnetism at the interface is necessary, for example through a neutron reflectometry study, or an a.c. susceptibility investigation of the spin glass. It can then be seen how the degree of spin glass formation depends on deposition parameters such as rate and power, as well as the roughness of the electrode layer.

Chapter 6: Supercurrents in Nb/Cr/Fe/Nb/Fe/Cr/Nb devices were examined. The dependence on the thickness of the Nb interlayer was markedly different between a set of samples with a total Fe thickness of 4 nm and two sets with thicker Fe where the total Fe thicknesses were 7.2 nm and 9.5 nm. In the two sets with thicker Fe, it was found that the decay of the supercurrent inside normal state Nb was much more rapid than in the devices with thin Fe. We speculate that the supercurrent may be triplet-dominated in the thicker-Fe devices. In such triplet-dominated devices, no supercurrent could be recovered at the appearance of singlet superconductivity in the interlayer. A shortcoming of this experiment was that the triplet supercurrent falls to zero for Nb thicknesses less than that at which the Nb interlayer becomes superconducting. For this reason, we are unable to probe the decay of the triplet in superconducting Nb directly, and can only conclude that the singlet superconductivity does not re-establish the triplet channel across the device.

Chapter 7: Nb/Pt/Nb and Nb/Pt/Nb/Pt/Nb Josephson junctions were studied, to establish the coherence length in Pt and the behaviour of S/N/S/N/S junctions. I attempted to generate LRTs in Nb/Pt/Co/Pt/Nb devices through a combination of Rashba spin-orbit coupling and an exchange field with an out-of-plane component, but observed the usual singlet decay length. Contemporaneous results from Satchell and Birge [76] corroborate this finding. An interesting possibility is that 0-π transitions might be achieved by varying the Pt thickness, since proximity-induced magnetism of Pt adjacent to Co provides a variation in the effective magnetic thickness. Further work is needed to observe such an oscillation, with many measurements required at Pt thicknesses below 1.5 nm on each side of the ferromagnet. Lateral Josephson junctions may hold greater promise for observing LRTs generated by SOC, predicted

by several theoretical papers, but there is scant experimental work on this at present. Lateral devices present some fabrication challenges, such as forming good interfaces after breaking vacuum between layers; I was involved in initial experimental attempts to achieve this, and continuing on this avenue may prove worthwhile.

Chapter 8: Attempts were made to open a triplet supercurrent channel through a superconducting interlayer in two devices: Nb/Cr/Fe/Nb/Pt/Nb, and Nb/Pt/Nb/Py/Nb/Pt/Nb, after the FMR experiments of Jeon et al. Neither of these were successful in doing so, with the behaviour in both cases being consistent with simple double-barrier singlet junctions. The exact mechanisms for opening the triplet channel in the FMR experiment were not determined. It might be that the dynamic precession plays a vital role in the pair-conversion, as well as the possibility of magnetic inhomogeneity at the interfaces, which was ruled out in that work. The next step may be returning to the FMR experiments and making careful studies of the effect of magnetic inhomogeneity by using for example Cr/Fe interfaces, or studying magnetic interfaces directly through neutron reflectometry.

Appendix A

Josephson junctions with a ferromagnetic exchange-spring

During the course of this PhD, I worked with Ekta Bhatia, visiting from the National Institute of Science Education and Research, Bhubaneswar, for six months. Her project focused on the control of Co/Py magnetic exchange spring structures and spin-triplet generation. The work resulted in a publication [78] where we demonstrate exchange-spring behaviour, reversible within a certain field range, and use this to modulate the critical temperature of Nb/Co/Py/Nb films. My contribution to this work was limited and falls outside the scope of this thesis, but subsequently, I continued this work to attempt to use these structures for triplet-generation.

The device fabrication and measurements in this chapter are the sole work of the author.

A.1 Nb/Py/Co/Py/Nb junctions

Fig. A.1 shows the saturation magnetization of the unpatterned Nb/Py(d_{Py})/Co(2)/Py(d_{Py})/Nb multilayer films plotted against the total Py thickness. From the bulk magnetizations of Co and Py, we can calculate the expected saturation moment as a base value of 284.4 emu for 2 nm Co, plus 70.46 emu per nm Py. This is plotted as the red dash-dot line in the figure. The grey dashed line is a fit to the data, corresponding to (30.9 + 84.3 d_{Py}) emu, where d_{Py} is in nm. The magnetic dead layer of Co reduces the magnetization from the expected value without Py, and the increased slope indicates that the Py thickness may actually be around 20% greater than assumed from the deposition.

$I_{\mathrm{c}}R_{\mathrm{N}}$, J_{c} and AR_{N} for the Nb/Py/Co/Py/Nb devices are plotted against the total Py thickness $2d_{\mathrm{Py}}$ in Fig. A.2. $I_{\mathrm{c}}R_{\mathrm{N}}$ and J_{c} decay rapidly, with decay constants 1.4 nm and 1.2 nm respectively, consistent with singlet superconductivity. AR_{N} shows a linear increase with $2d_{\mathrm{Py}}$, allowing us to estimate the resistivity of Py as (46 ± 4) μΩ cm. This is in agreement with the literature for Py in this thickness range [79].

$I_{\mathrm{c}}(H)$ behaviour of the junctions is shown in Fig. A.3. The hysteresis of the pattern ΔH is shown in Fig. A.4. The hysteresis increases with increasing ferromagnetic thickness, consistent with the picture of internal flux contributing to the device behaviour.

Fig. A.5 shows magnetic moment per unit area against in-plane applied field (hysteresis loops) measured at room temperature for unpatterned Nb/Py(d_{Py})/Co(2)/Py(d_{Py})/Nb multilayer films. Two sets of films were prepared, one where 1.6 nm < $2d_{Py}$ < 11 nm, and in the other, 3.2 nm < $2d_{Py}$ < 30 nm. For the latter set, measurements were performed along two perpendicular directions in the plane of the film, yielding significantly different loop shapes. There appears to be a hard axis (low remanence) and an easy axis (high remanence) in the plane of the films. The most likely reason for this is that although they are polycrystalline, the films have some degree of crystallographic texture, leading to a net magnetocrystalline anisotropy. This may be due to the strong magnetic field of the magnetron influencing grain development (and therefore magnetocrystalline anisotropy) at the substrate during deposition.

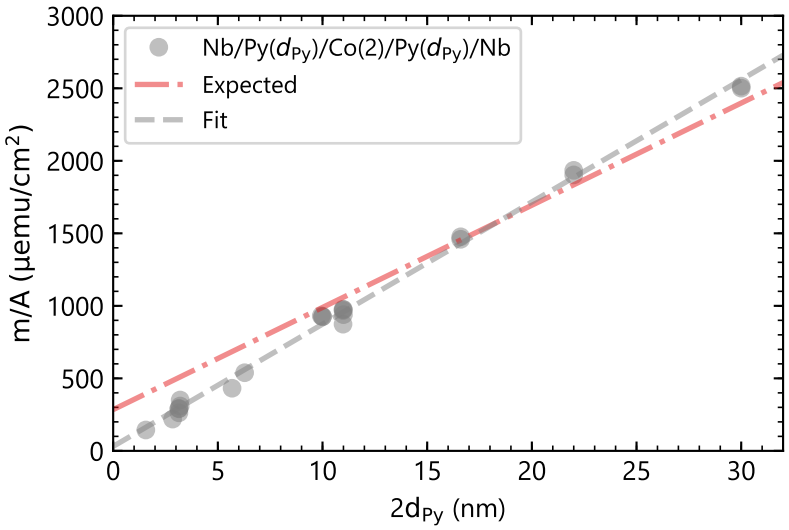


FIGURE A.1: Saturation magnetization per unit area against Py thickness. The expected saturation moment obtained by summation of bulk volume magnetizations of Co and Py is shown as the red dash-dot line. The grey dashed line is a least-squares fit to the data.

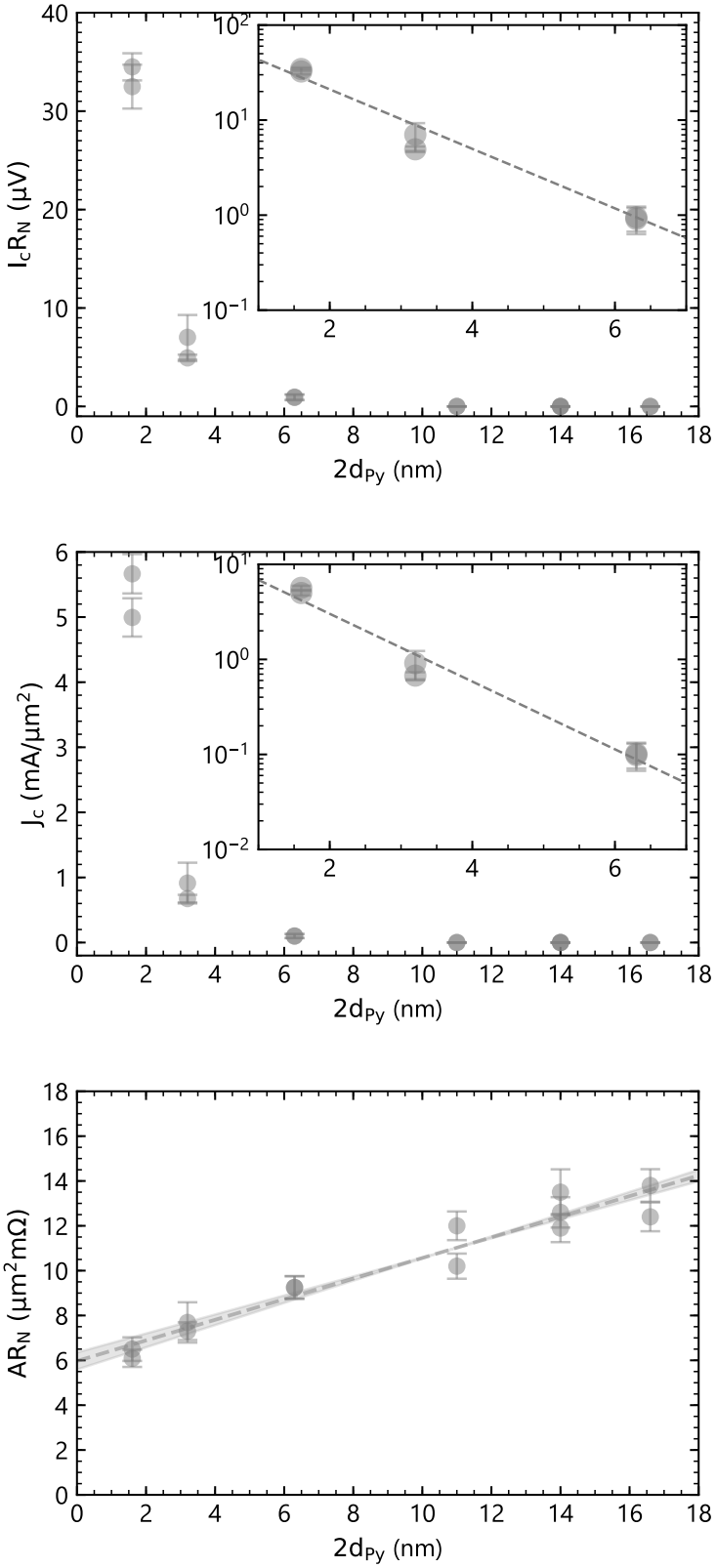


FIGURE A.2: I_cR_N, J_c and AR_N measured for varying Py thickness in Nb/Py(d_{Py})/Co(2)/Py(d_{Py})/Nb devices at 1.6 K. The insets in the top two panels show the same data on logarithmic scales with a linear decay fitted, with the decay constants 1.4 nm (I_cR_N) and 1.2 nm (J_c). The dashed line in the AR_N plot is a linear fit, with the shaded region corresponding to the standard error of the fit.

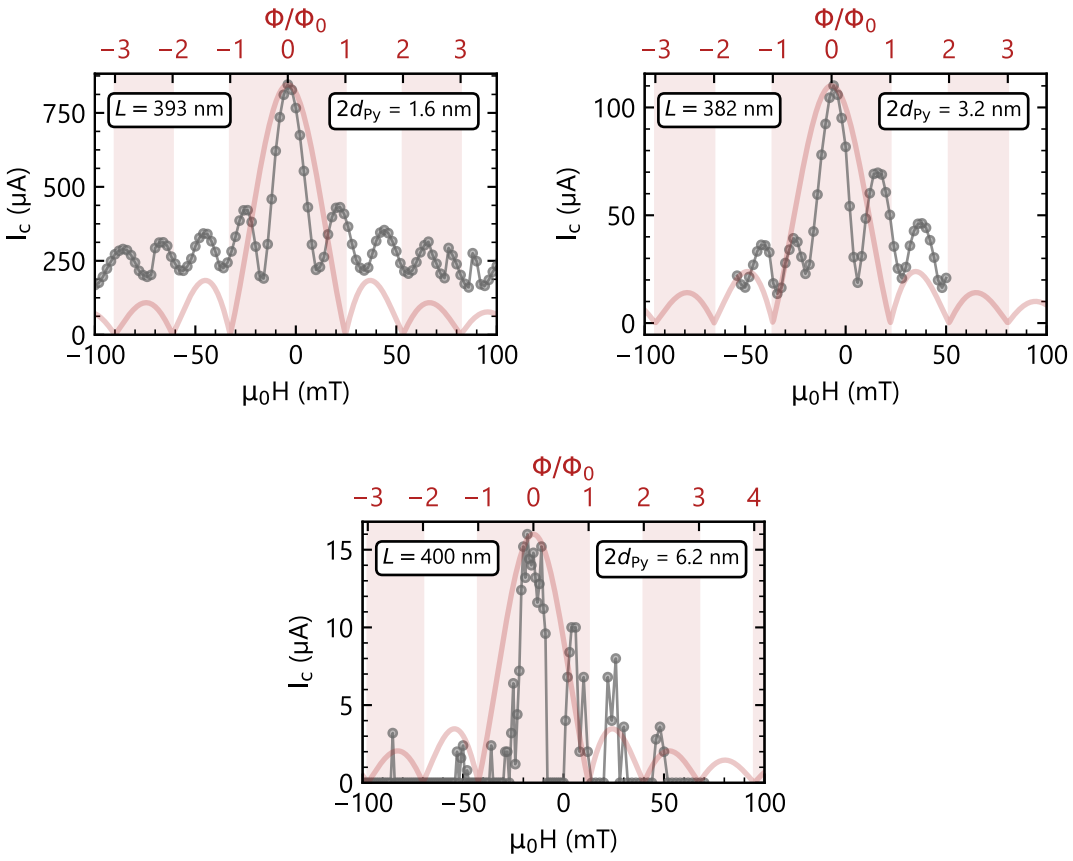


FIGURE A.3: Fraunhofer patterns for Nb/Py(d_{Py})/Co(2)/Py(d_{Py})/Nb devices at 1.6 K. The red shaded regions, top axis and red model pattern are calculated from the device dimensions and show the expected periodicity. The grey points are the measured data, with the grey line joining subsequent measurements as a guide to the eye.

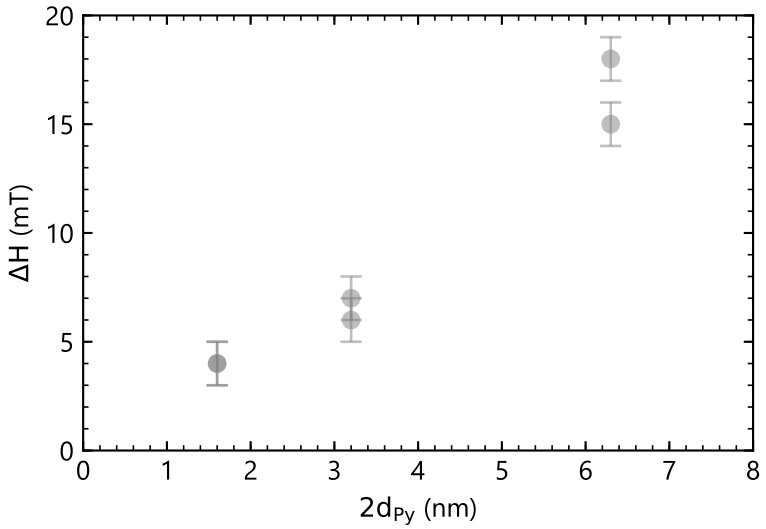


FIGURE A.4: Hysteresis of the Fraunhofer pattern ΔH against total Py thickness for Nb/Py(d_{Py})/Co(2)/Py(d_{Py})/Nb devices at 1.6 K.

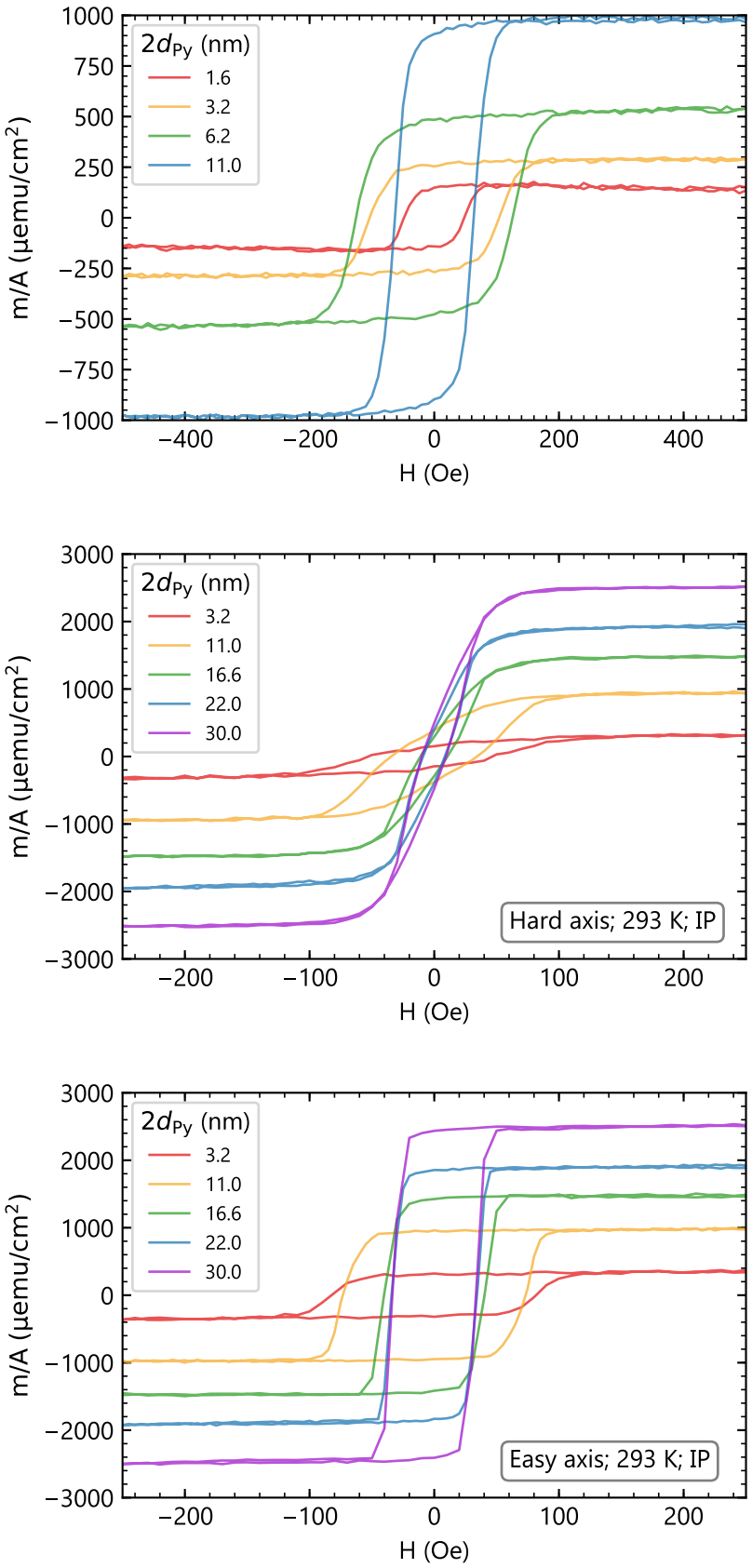


FIGURE A.5: $M(H)$ loops for unpatterned Nb/Py(d_{Py})/Co(2)/Py(d_{Py})/Nb films from two deposition runs (top: run 1; middle and bottom: run 2).

A.2 Conclusions

There was no evidence of having generated a long-ranged triplet in these devices. More careful characterization and control of the exchange-spring structure may be required.

Bibliography

[1] A. Bérut et al. *Nature* **483**.7388, 187–189 (2012).

[2] M. Johnson and R. H. Silsbee. *Phys. Rev. B* **37**, 5312–5325 (1988).

[3] M. N. Baibich et al. *Phys. Rev. Lett.* **61**, 2472–2475 (1988).

[4] J. Barnaś et al. *Phys. Rev. B* **42**, 8110–8120 (1990).

[5] P. M. Tedrow and R. Meservey. *Phys. Rev. Lett.* **26**, 192–195 (1971).

[6] J. Linder and J. W. A. Robinson. *Nat. Phys.* **11**.4, 307–315 (2015).

[7] K.-R. Jeon et al. *Nat. Mater.* **17**.6, 499–503 (2018).

[8] J. Cornwell, D. Hum, and K. Wong. *Phys. Lett. A* **26**.8, 365 –366 (1968).

[9] J. Stöhr and H. C. Siegmann. *Magnetism: From Fundamentals to Nanoscale Dynamics*. Springer, 2006.

[10] M. M. Sigalas and D. A. Papaconstantopoulos. *Phys. Rev. B* **50**, 7255–7261 (1994).

[11] J. Geissler et al. *Phys. Rev. B* **65**, 020405 (2001).

[12] R. M. Rowan-Robinson et al. *Sci. Rep.* **7**.1, 16835 (2017).

[13] E. Fawcett. *Rev. Mod. Phys.* **60**, 209–283 (1988).

[14] H. Zabel. *J. Phys.: Condens. Matter* **11**.48, 9303–9346 (1999).

[15] S. Blundell. *Magnetism in Condensed Matter*. OUP Oxford, 2001.

[16] D. Pierce et al. *J. Magn. Magn. Mater.* **200**, 290–321 (1999).

[17] K. H. Fischer and J. A. Hertz. *Spin Glasses*. Cambridge Studies in Magnetism. Cambridge University Press, 1991.

[18] C. R. Fincher et al. *Phys. Rev. Lett.* **45**, 474–477 (1980).

[19] J. O. Strom-Olsen et al. *J. Phys. F: Met. Phys.* **9**, L95 (1979).

[20] S. K. Burke et al. *J. Phys. F: Met. Phys.* **13**.2, 451–470 (1983).

[21] J. W. A. Robinson, N. Banerjee, and M. G. Blamire. *Phys. Rev. B* **89**, 104505 (2014).

[22] I. Mihai Miron et al. *Nat. Mater.* **9**.3, 230–234 (2010).

[23] L. Néel. *J. Phys. Radium* **15**, 225–239 (1954).

[24] P. F. Carcia, A. D. Meinhaldt, and A. Suna. *Appl. Phys. Lett.* **47**.2, 178–180 (1985).

[25] B. Tudu and A. Tiwari. *Vacuum* **146**, 329 –341 (2017).

[26] D. Weller et al. *Phys. Rev. Lett.* **75**, 3752–3755 (1995).

[27] K. Kyuno et al. *J. Appl. Phys* **79**.9, 7084–7089 (1996).

[28] S. Bandiera et al. *IEEE Magn. Lett.* **2**, 3000504–3000504 (2011).

[29] P Bruno. *J. Phys. F: Met. Phys.* **18**.6, 1291–1298 (1988).

[30] C. Kittel. *Introduction to Solid State Physics*. 8th ed. Wiley, 2004.

[31] M. Tinkham. *Introduction to Superconductivity*. 2nd ed. Dover Publications, 2004.

[32] A. I. Gubin et al. *Phys. Rev. B* **72**, 064503 (2005).

[33] H. Fröhlich. *Phys. Rev.* **79**, 845–856 (1950).

[34] C. A. Reynolds et al. *Phys. Rev.* **78**, 487–487 (1950).

[35] E. Maxwell. *Phys. Rev.* **78**, 477–477 (1950).

[36] L. N. Cooper. *Phys. Rev.* **104**, 1189–1190 (1956).

[37] J. Bardeen, L. N. Cooper, and J. R. Schrieffer. *Phys. Rev.* **106**, 162–164 (1957).

[38] A. Zagoskin. *Quantum Theory of Many-Body Systems: Techniques and Applications*. 2nd ed. Springer, 2014.

[39] B. Josephson. *Phys. Lett.* **1**.7, 251 –253 (1962).

[40] A. Barone and G. Paternò. *Physics and Applications of the Josephson Effect*. John Wiley & Sons, 1982.

[41] I. Zapata and F. Sols. *Phys. Rev. B* **53**, 6693–6704 (1996).

[42] V. C. Chang and C. Chu. *Solid State Commun.* **107**.8, 433 –438 (1998).

[43] M. Eschrig. *Phys. Today* **64**.1, 43–49 (2011).

[44] F. S. Bergeret, A. F. Volkov, and K. B. Efetov. *Phys. Rev. Lett.* **86**, 4096–4099 (2001).

[45] F. S. Bergeret, A. F. Volkov, and K. B. Efetov. *Rev. Mod. Phys.* **77**, 1321–1373 (2005).

[46] M. Giroud et al. *Phys. Rev. B* **58**, R11872–R11875 (1998).

[47] V. T. Petrashov et al. *Phys. Rev. Lett.* **83**, 3281–3284 (1999).

[48] M. Eschrig et al. *Phys. Rev. Lett.* **90**, 137003 (2003).

[49] R. S. Keizer et al. *Nature* **439**.7078, 825–827 (2006).

[50] I. Sosnin et al. *Phys. Rev. Lett.* **96**.15, 1–4 (2006).

[51] M. Houzet and A. I. Buzdin. *Phys. Rev. B* **76**, 060504 (2007).

[52] J. Robinson, J. Witt, and M. Blamire. *Science* **329**.5987, 59–61 (2010).

[53] G. B. Halász et al. *Phys. Rev. B* **79**.22, 1–9 (2009).

[54] G. B. Halász, M. G. Blamire, and J. W. A. Robinson. *Phys. Rev. B* **84**.2, 1–5 (2011).

[55] J. W. A. Robinson et al. *Sci. Rep.* **2**.1, 699 (2012).

[56] T. S. Khaire et al. *Phys. Rev. Lett.* **104**.13, 2–5 (2010).

[57] C. Klose et al. *Phys. Rev. Lett.* **108**, 127002 (2012).

[58] F. S. Bergeret and I. V. Tokatly. *Phys. Rev. B* **89**.13, 1–13 (2014).

[59] S. H. Jacobsen, I. Kulagina, and J. Linder. *Sci. Rep.* **6**.1, 23926 (2016).

[60] M. G. Blamire, A. Aziz, and J. W. A. Robinson. *Phil. Trans. R. Soc. A* **369**, 3198–3213 (2011).

[61] J. F. Ziegler and J. P. Biersack. *The Stopping and Range of Ions in Matter*. New York: Pergamon, 1985.

[62] A. Daire. *White paper: An Improved Method for Differential Conductance Measurements*. 2610. Cleveland, Ohio: Keithley, 2005.

[63] *White paper: Achieving Accurate and Reliable Resistance Measurements in Low Power and Low Voltage Applications*. 2544. Cleveland, Ohio: Keithley, 2004.

[64] S. Piano et al. *Eur. Phys. J. B* **58**.2, 123–126 (2007).

[65] J. W. A. Robinson et al. *Phys. Rev. Lett.* **104**, 207001 (2010).

[66] F. Kajzar, G. Parette, and B. Babic. *J. Phys. Chem. Solids* **42**.6, 501 –512 (1981).

[67] Weiss, Pierre and Forrer, R. *Ann. Phys.* **10**.12, 279–372 (1929).

[68] J. W. A. Robinson et al. *Phys. Rev. B* **76**, 094522 (2007).

[69] J. A. Glick et al. *J. Appl. Phys.* **122**.13, 133906 (2017).

[70] M. Morota et al. *Phys. Rev. B* **83**, 174405 (2011).

[71] X. Montiel and M. Eschrig. *Phys. Rev. B* **98**, 104513 (2018).

[72] D. Papaconstantopoulos. *Handbook of the Band Structure of Elemental Solids*. New York: Plenum Press, 1986.

[73] N. W. Ashcroft and N. D. Mermin. *Solid State Physics*. Holt-Saunders, 1976.

[74] S. Emori and G. S. D. Beach. *J. Appl. Phys.* **110**.3, 033919 (2011).

[75] B. D. Cullity and C. D. Graham. "Appendix 2: Data on Ferromagnetic Elements". *Introduction to Magnetic Materials*. John Wiley Sons, Ltd, 2008.

[76] N. Satchell and N. O. Birge. *Phys. Rev. B* **97**, 214509 (2018).

[77] N. Satchell, R. Loloee, and N. O. Birge. *Phys. Rev. B* **99**, 174519 (2019).

[78] E. Bhatia et al. *App. Phys. Lett.* **116**.11, 112601 (2020).

[79] T. G. S. M. Rijks et al. *Phys. Rev. B* **56**, 362–366 (1997).